AN EXPERIMENTAL STUDY OF THE KINETICALLY ARRESTED STATES OF COLLOIDAL SUSPENSIONS

By

Sanjay Kumar Behera

A thesis submitted to the Jawaharlal Nehru University

for the degree of Doctor of Philosophy

Department of Soft Condensed Matter

Raman Research Institute

Bengaluru 560 080

February 2020

Typeset in LaTeX 2_{ε}.

Certificate:

This is to certify that the thesis entitled **"An experimental study of the kinetically arrested states of colloidal suspensions"** submitted by Sanjay Kumar Behera for the award of the degree of Doctor of Philosophy of Jawaharlal Nehru University is his original work. This has not been published or submitted to any other University for any other Degree or Diploma.

Prof. Ravi Subrahmanyan
(Director)
Raman Research Institute
Bengaluru 560 080
India

Prof. Ranjini Bandyopadhyay
(Thesis Supervisor)

Declaration:

I hereby declare that the work reported in this thesis is entirely original. This thesis is composed independently by me at Raman Research Institute under the supervision of Prof. Ranjini Bandyopadhyay. I further declare that the subject matter presented in this thesis has not previously formed the basis for the award of any degree, diploma, membership, associateship, fellowship or any other similar title of any university or institution. I also declare that I have run it through **Turnitin** plagiarism detection software.

Prof. Ranjini Bandyopadhyay
(Thesis Supervisor)
Soft Condensed Matter Group
Raman Research Institute
Bengaluru 560 080
India

Sanjay Kumar Behera

Acknowledgements

I express my sincere gratitude to my thesis supervisor Prof. Ranjini Bandyopadhyay for her superb guidance, constant support and encouragement throughout the duration of thesis work and beyond. I am grateful to her for encouraging me in independent thinking, believing in my ability and giving me a friendly lead whenever needed. I thank her for modifying me in improving my presentation, writing and data analysis skills. Finally, I thank her for arranging the DST SERB project fellowship during my final year.

A very sincere note of thanks is to Prof. Sandeep Kumar for allowing me to use the facilities of chemistry laboratory. I thank to my student advisory committee members Dr. Gautam Soni, Prof. Sadiq Rangwala, Prof. V. A. Raghunathan and Prof. Sanjib Sabhapandit for their useful discussions, suggestions and help with many academic issues. I would like to thank Dr. Sayantan Mujumdar, Prof. Pramod Pullarkat, Prof. R. Pratibha, Prof. Y. Hatwalne and other faculty members of Soft Condensed Matter Group for their helpful discussions and encouragement.

I express my sincere gratitude to my senior lab mates, Dr. Debasish Saha, Dr. Paramesh Gadige, Dr. Samim Ali and Dr. Rajib Basak for helping me in familiarizing with the experimental set up and useful discussions. I thank to my junior lab mates Mr. Chandeshwar Misra, Mr. Rajkumar Biswas, Miss Palak, Miss Riddhika Mahalanabis and Mr. Tonmoy Gogoi for their help with the experiments. I thank them for their

company and help throughout my PhD period. I also thank my past lab mates, Mr. Sai Ganesh, Mr. Venkatesh, Mr. Vipin, Mrs. Harsha, Miss Rashmi and Mrs. Janeet for their help with the experiments and pleasant company. My sincerest thanks and regards to my seniors, Dr. Debasish Saha, Dr. Paramesh Gadige and Dr. Samim Ali for helping me in countless occasions and giving me company and support when I needed it most. A special note of thanks to Miss Palak for motivating me.

I am thankful to Mr. Swamynathan, Mr. Marichandran, Mr. Irla Siva Kumar, Dr. Avinash, Mr. Ashwath and Dr. H. T. Srinivasa for their useful discussions and help in synthesis of colloidal particles. I express my gratitude to Mr. K. M. Yatheendran and Mr. A. Dhason for their help with SEM and cryo-SEM imaging. I extend my thanks to Mrs. K. N. Vasudha for her help with the UV-visible and infrared spectrophotometer experiments. I am also thankful to Mr. K. M. Yatheendran for his help with confocal microscopy imaging. I am thankful to Mr. A. Dhason for his help in fabricating glasswares for my experiments. I am also thankful to Mr. Mani for his help in glass etching. I am thankful to Mrs. Serena R. D. for her help in using centrifuge machine. I am thankful to all members of RRI workshop for their help and support.

I would like to express my gratitude to SCM group secretary Mr. K. Radhakrishna for his assistance with purchasing chemicals and laboratory components, arranging transport, travel claim and many more official things. My sincere thanks to Raja and Murali for their help in daily basis. I would like to thank all the staff members of the library for their help and support. I am thankful to all staff members in the purchase and account departments for their help with purchasing laboratory equipments, travel claim and foreign exchange. I would like to thank all the staff members of the computer section for their assistance to sort out countless issues regarding software installation and internet connectivity.

I express my gratitude to the director, Prof. Ravi Subrahmanyan for his help regarding various academic issues. I would like to thank the administrative officer, Mr. CSR Murthy for his assistance with countless administrative issues. I express my sincere gratitude to all staff members of administration, especially Mr. Naresh, Mrs. K.

Radha, Mrs. Marisa and Mrs. Vidya for their help and support. I acknowledge all the canteen staff members, hostel staff members, and everyone at RRI for their cooperation and encouragement.

I am thankful to every student at RRI for their company, entertainment, support and encouraging discussions in various academic and nonacademic topics. I would like to thank my friends Sreeja, Amit, Santanu, Ashwath, Shikha, Prutha, Karishma, Tripti, Ashutosh, Siman, Alkesh, Rajarshi, Deepshikha, Janakee, Varun and Neha for their company and giving me many pleasurable moments. I would like to thank my seniors Sushil, Jagadish, Madhukar, Jayakumar, Meera, Renu, Radhakrishna, Surya, Raj Hossen, Niranjan, Anirudh, Karamveer, Priyanka, Karthik, Mahaveer, Santosh, Arnab, Chaitra and Yogesh for their valuable suggestions and discussions. I would particularly like to thank Tukun, Anya, Rajkumar, Chandeshwar, Jagadeesh, Swamynathan, Marichandran, Deepak, Subodh, Sagar, Sharath, Nooman, Sreyas, Madhavan, Prasad, Shafi, Tridib, Rangaraj, Arnab, Anjan, Rahul, Chandan and Venu for helping me relax through many sports activities such as cricket, football, badminton, volleyball and chess. I am thankful to Anindya, Vishnu, Saichand, Dipak, Arsalan, Ashish, Sukh veer, Sumanth, Alaka, Vani, Madhu, Mahesh, Abhishek, Sachidananda, Sebanti, Nishant, Saurabh, Pradosh and Raj Prince for giving me many more pleasurable moments. I am thankful to boarders at Vyalikaval and RMV hostel for being amazing friends during my stay and doing many fun activities like cooking food, watching movies and celebrating holi, diwali etc. Especially, I would like to thank Jagdish, Sushil, Amit, Debasish, Samim, Rajkumar, Palak, Chandeshwar, Anand, Shivam and Meera for their help with cooking on weekend and holidays.

At Last, I express my deepest gratitude, love and respect for my parents Mr. Ramachandra Behera and Mrs. Sabita Behera, my brother Mr. Rajesh Behera, my ladylove Miss Satyanistha Sankhua, my teacher Mr. Birakishore Satapathy and other family members for their constant support, motivation and help in every ups and downs in my life.

Synopsis

The kinetically arrested states of soft materials such as colloidal and hydrogel suspensions are interesting because of their variable microstructures and heterogeneous and ultra slow dynamics. In this thesis, colloidal particles with tunable size polydispersities, stiffnesses and activity have been synthesized and the approach to kinetic arrest of dense suspensions of these particles have been studied experimentally. Polydispersity, stiffness and activity are seen to greatly affect the microstructures and dynamics of the arrested states of these dense suspensions. As the suspensions approach the kinetically arrested state, the growth of viscosity or relaxation times with volume fraction, the suspension fragility and the sizes of dynamical heterogeneities are strongly affected by size polydispersity, stiffness and activity of the constituent colloidal particles. In this thesis, we have studied the structure, dynamics and flow behaviour of kinetically arrested states formed by thermoresponsive poly(*N*-isopropylacrylamide) (PNIPAM) particles and in suspensions of active and passive colloidal particles.

Thermoresponsive PNIPAM particles deswell by expelling water with increase in temperature. Moreover, at a fixed temperature and in dense suspensions, these particles deform when the particle volume fraction increases beyond the random close packing volume fraction (ϕ_{rcp}) of monodisperse hard spheres. This swelling behaviour allows us to control the packing properties of these soft particles in dense suspensions. The packing properties, in turn, influence the dynamical behaviours of the colloidal phases

formed in these suspensions. For example, for a fixed solvent temperature and volume fraction, the microscopic structure, dynamics and flow behaviour of dense PNIPAM suspensions are expected to be affected by the stiffness and polydispersity of the dispersed colloidal particles. In order to study the effects of polydispersity and stiffness on the kinetically arrested state of thermoresponsive soft particles, we have prepared PNIPAM particles of different polydispersities by controlling the flow rates of the reaction ingredients into the reaction vessel. We have also synthesized PNIPAM particles of different stiffnesses by varying the concentration of the crosslinkers used in the reaction. Furthermore, to investigate the effects of activity on the dynamics of dense suspensions of passive colloidal particles, we have synthesized chemically active Janus particles by coating platinum on one hemisphere of the polystyrene microspheres. The propulsion of a Janus particle is facilitated by the platinum induced catalytic decomposition of hydrogen peroxide into water and oxygen. The presence of a small amount of active particles in a crowded environment of passive particles is expected to strongly influence the suspension dynamics. Theoretical studies have reported that the incorporation of activity or self propulsion induces a cage breaking phenomenon in dense bidisperse suspensions of passive particles.

Chapter 1 of this thesis presents the background information required to understand the research presented in this thesis. This chapter gives a brief introduction to colloidal suspensions and contains a detailed discussion on suspensions of thermoresponsive hydrogel particles and chemically active particles. This is followed by an overview of the dynamics of colloidal jammed states, the unique features of colloidal systems approaching kinetically arrested states and the various interparticle interactions such as van der Waals interaction and screened electrostatic repulsion between colloidal particles. Features of a variety of phases in kinetically arrested states are next described in detail. This is followed by a discussion of the dynamics of noninteracting active particles in a homogeneous environment and in mixtures of active and passive particle suspensions.

Chapter 2 describes the methods used to prepare the suspensions studied in this

thesis and the experimental techniques employed in this thesis work. This chapter contains detailed descriptions of the synthesis methods used by us to control the size polydispersity, stiffness and activity of the colloidal particles used here. The experimental techniques employed in this thesis include dynamic light scattering, rheological measurements, confocal microscopy, scanning electron microscopy (SEM), cryogenic SEM, ultrasound attenuation spectroscopy and ultraviolet-visible spectroscopy and have been discussed in this chapter. Finally, an experimental setup used for measuring the oxygen evolution rate due to the platinum induced catalytic decomposition of hydrogen peroxide is described.

Chapter 3 presents the effects of polydispersity on the dynamics of suspensions of soft PNIPAM colloidal particles. Two different synthesis methods are followed to synthesize PNIPAM colloidal particles with polydispersity indices (PDIs) varying over a wide range (7.4%-48.9%). PDIs of these colloidal particles are controlled by varying the flow rates of the reaction ingredients added externally into the reaction vessel in a semi-batch method. In the one-pot method, on the other hand, the PDI is controlled by varying the concentration of the added surfactant. We use a modified parameter called the effective volume fraction (ϕ_{eff}) for estimating the volume fractions (ϕ) of suspensions of these soft and deformable particles. The zero shear viscosity (η_0) values of these colloidal suspensions, estimated from rheometric experiments as a function of the effective volume fraction (ϕ_{eff}), show a dramatic increase at a volume fraction near the jamming point. The data for η_0 as a function of ϕ_{eff} are seen to fit well to the Vogel-Fulcher-Tammann (VFT) equation. The fragility, which signifies the deviation from Arrhenius behaviour and is obtained from VFT fits, is seen to increase with PDI. Moreover, the jammed state formed by these colloidal particles are observed to fluidize with the increase in PDIs. Jammed suspensions of PNIPAM particles are seen to form highly fragile glasses at volume fractions well above the random close packing volume fraction ϕ_{rcp} of monodisperse hard sphere colloidal suspensions. The observed increase in fragility is attributed to the prevalence of dynamical heterogeneities (DHs) in these polydisperse suspensions, while the fluidization of the jammed state of these

suspensions is ascribed to the decoupling of the dynamics of the smallest and largest particles. The fluidization of jammed states and the increase in fragility of these concentrated suspensions with an increase in particle PDI is supported by our nonlinear rheology results. The nonlinear stress response at the third harmonic to applied oscillatory strains is measured to quantify the intrinsic nonlinearity of these samples. The changes in the intrinsic nonlinearity of these suspensions are monitored by changing ϕ_{eff} at a fixed PDI and by changing particle PDIs at a fixed ϕ_{eff}. The nonlinearity of the dynamics of these suspensions is observed to increase when ϕ_{eff} and PDI are increased.

Chapter 4 explores the role of particle size polydispersity on the spatio-temporal heterogeneity and the caging dynamics of polydisperse aqueous PNIPAM colloidal suspensions approaching the dynamically arrested state. We have studied the evolution of the dynamics of the particles in their dense suspensions by computing the mean square displacements and the non-Gaussian parameter as a function of lag time from two dimensional confocal images. The plateau in the MSD curves versus lag time observed at the initial times slowly disappears with the increase in PDI at a fixed area fraction and confirms that the caging behaviour becomes weak with increasing PDI in dense aqueous suspensions of PNIPAM particles. This conclusion supports the results obtained in chapter 3. To extract information about the evolution of spatial heterogeneities, the probability distribution of the displacements of the particles is plotted for several different time intervals. It is seen that the probability distribution becomes broader and deviates from Gaussian behaviour with the progress of time. To quantify the spatial heterogeneity present in these polydisperse systems, we have estimated the non-Gaussian parameter as a function of lag time. For a PNIPAM suspension of fixed polydispersity and area fraction, the non-Gaussian parameter is seen to exhibit a peak with increase in time. The peak height of the non-Gaussian parameter shows a non-monotonic increase with PDIs. This observation shows that spatio-temporal heterogeneity of these polydisperse systems increases with PDI and the dynamics becomes maximally heterogeneous for a certain value of PDI. When PDI is increased further,

the spatio-temporal heterogeneity reduces and finally vanishes.

Chapter 5 describes the temperature and stiffness induced phase changes in dense suspensions of PNIPAM colloidal particles and their macroscopic mechanical responses in oscillatory strain sweep experiments. The stiffness of PNIPAM colloidal particles is controlled by varying the concentration of the crosslinkers in the one-pot synthesis method. Dense suspensions of these particles show a non-monotonic increase of viscoelastic moduli with increase in temperature. We observe that when the temperature is increased above the lowest critical solution temperature (LCST), the rigidity moduli of the suspensions increase with increasing temperature. This observation, while contrary to intuition, can be successfully explained by considering that the hydrophobicity of the particles increase with temperature. The increase in temperature above the LCST also affects the underlying microscopic structures of these suspensions. Above the LCST, a rheological investigation of suspensions of stiff particles shows a two-step yielding behaviour similar to that observed in attractive glasses. From the data analysis of oscillatory strain sweep experiments, it is concluded that PNIPAM suspensions of stiff particles are less elastic and shear melt at smaller strain amplitudes when compared to suspensions of soft particles. Next, we directly visualize the microscopic structures of dense suspensions of colloidal particles of different stiffnesses at different temperatures using cryogenic scanning electron microscopy. We observe a transition from a gel network to a structure constituted by attractive clusters in suspensions of stiff particles with increasing temperature. Suspensions of soft particles, however, are always seen to remain in the gel phase for the entire range of temperatures explored in these experiments.

Chapter 6 describes the effects of active forces or activity on the kinetically arrested state of binary mixtures of passive particles. Chemically active Janus particles are synthesized by coating platinum on one hemisphere of polystyrene microspheres. These particles self-propel in a hydrogen peroxide solution due to the platinum induced catalytic decomposition of hydrogen peroxide into water and oxygen. The rate of self propulsion of these particles is observed to increase with the increase in concentration

of fuel (hydrogen peroxide). When a small concentration of these active particles is added in densely packed bi-dispersed polystyrene microspheres, the cages formed by the passive polystyrene particles are seen to break due to the activity of the Janus particles. When the concentration of fuel is increased while keeping the concentration of active particles fixed, the jammed states formed by suspensions of these microparticles are fluidized.

Chapter 7 summarizes the main results reported in this thesis and briefly discusses the scope for future work.

Prof. Ranjini Bandyopadhyay
(Thesis Supervisor)
Soft Condensed Matter Group
Raman Research Institute
Bengaluru 560 080
India

Sanjay Kumar Behera

Publication List

Publications from this thesis:

1. Effects of polydispersity on the glass transition dynamics of aqueous suspensions of soft spherical colloidal particles, **Sanjay Kumar Behera**, Debasish Saha, Paramesh Gadige and Ranjini Bandyopadhyay, *Physical Review Materials*, 2017, 1, 055603, DOI: 10.1103/PhysRevMaterials.1.055603

2. Study of dynamical heterogeneities in colloidal nanoclay suspensions approaching dynamical arrest, Paramesh Gadige, Debasish Saha, **Sanjay Kumar Behera** and Ranjini Bandyopadhyay, *Scientific Reports*, 2017, 7, 8017, DOI: 10.1038/s41598-017-08495-9

3. Influence of particle size on the thermoresponsive and rheological properties of aqueous poly(*N*-isopropylacrylamide) colloidal suspensions, Chandeshwar Misra, **Sanjay Kumar Behera** and Ranjini Bandyopadhyay, manuscript is accepted for publication in *Bulletin of Materials Science*.

Contents

Acknowledgements vii

Synopsis xi

Publication List xvii

1 Introduction 5

1.1 Colloidal suspensions 5

1.2 Thermoresponsive Poly(*N*-isopropylacrylamide) (PNIPAM) hydrogel particles 8

1.3 Janus particles 10

1.4 Interparticle interactions in colloidal systems 13

1.4.1 Electrostatic repulsion 14

1.4.2 van der Waals attraction 16

1.4.3 Hydrophobic attraction 16

1.5 Colloidal jamming 17

1.6 Phases in colloidal suspensions 19

1.7 Features of colloidal system approaching jammed or kinetically arrested states 21
1.7.1 Growth of viscosity and relaxation times 21
1.7.2 Fragility 23
1.7.3 Dynamical heterogeneity 25
1.8 Soft particle suspension rheology 26

References **29**

2 Materials and Methods **39**
2.1 Introduction 39
2.2 Synthesis methods 40
2.2.1 Synthesis of PNIPAM colloidal particles 40
2.2.2 Synthesis of chemically active Janus particles 44
2.3 Experimental techniques 46
2.3.1 Dynamic Light Scattering 46
2.3.2 Rheological measurements 52
2.3.3 SEM 63
2.3.4 Zeta potential measurements: 66
2.3.5 Confocal microscopy 67

References **70**

3 Effects of polydispersity on the glass transition dynamics of aqueous suspensions of soft spherical colloidal particles **73**
3.1 Introduction 73
3.2 Sample preparation 77
3.3 Results and discussion 78
3.4 Conclusions 97

References **99**

4 Study of microscopic dynamics of a polydisperse colloidal suspension approaching kinetic arrest. **103**

4.1 Introduction 103

4.2 Sample preparation 105

4.2.1 Preparation of aqueous suspensions of fluorescent PNIPAM particles and measurement of their zeta potential: 107

4.3 Confocal microscopy imaging and Particle tracking: 108

4.4 Estimation of Area fraction and PDI: 109

4.5 Results and discussion 110

4.6 Conclusions 113

References **115**

5 Temperature and stiffness induced phase changes in dense aqueous suspensions of thermoresponsive poly(*N*-isopropylacrylamide) colloidal particles **117**

5.1 Introduction 118

5.2 Sample preparation 120

5.2.1 Estimation of the effective volume fraction ϕ_{eff} 120

5.3 Results and discussion 122

5.4 Conclusions 131

References **133**

6 The effect of activity on the kinetically arrested state of passive particles **137**

6.1 Introduction 137

6.2 Sample preparation 139
6.2.1 Preparation of passive binary mixture 139
6.2.2 Preparation of active-passive hybrid mixture 140
6.2.3 Estimation of particle volume fraction 140
6.3 Designing microchannel as a sample cell 140
6.4 Measurement of hydrogen peroxide decomposition rate 142
6.5 Confocal microscopy imaging and particle tracking 145
6.6 Results and Discussion 146
6.7 Conclusions 149

References **151**

7 Future directions **153**

References **156**

1

Introduction

1.1 Colloidal suspensions

A colloidal suspension is a heterogeneous system in which particles of solid, liquid or gas are dispersed in a continuous liquid, gas or solid medium [1]. Familiar examples of colloidal suspensions are biological fluids such as blood and milk, shaving cream, smoke, mayonnaise, cranberry glass etc [2]. In a colloidal suspension, the sizes of the dispersed particles are significantly larger than the sizes of the particles of the suspension medium. The sizes of colloidal particles lie in the range 10 nm-10 μm [3]. The lower size limit is set by the size of the suspension medium. The upper size limit is set to avoid gravitational settling or convection of these particles. Essentially, the Brownian motion of a colloidal particle should not be affected by the gravitational force exerted on it [4]. Colloidal particles have a high surface area to volume ratio. A colloidal dispersion therefore has a high area of interface. For instance, 1 litre of an aqueous colloidal suspension containing monodisperse colloidal particles of 100 nm radius at a volume fraction 0.5 has a total area of interface between water and colloidal

particle of around 15000 m^2. The high area of interface of a colloidal particle not only allows the adsorption of chemicals and other moieties onto the particle surface but also affects the interaction between particles and hence the suspension properties [5]. The size of the colloidal particle is more than 1000 times larger than the size of the atom. The number density of an atomic material ($n_A \approx 10^{23}$ cm^{-3}) is approximately 10 billion times the number density of a typical colloidal suspension ($n_c \approx 10^{13}$ cm^{-3}). The colloidal crystals and glasses are therefore at least 100 times less elastic than the atomic materials [4]. The sizes of the colloidal particles are sufficiently small such that thermal fluctuations drive their movement. At a certain temperature, colloidal particles in a suspension perform Brownian motion due to random collisions with the particles of the suspending medium [6]. The relaxation time of a colloidal particle that is freely diffusing in a suspension medium is defined as: $\tau_R = R^2/D$, where D is the self diffusion coefficient of the particle, R is the radius of the particle and τ_R is the time taken by the particle to diffuse a distance equal to its radius [4]. For a colloidal particle, τ_R is of the order of ms-μs, while for a typical atomic material it is of the order of picoseconds. This large relaxation time of colloidal particles allows experimenters to study their dynamics in the laboratory [7, 8].

Colloidal particles available in nature are inevitably polydisperse [9]. Polydispersity of the spherical colloidal particles is defined as the ratio of the standard deviation of the particle size distribution to the mean size [9, 10] and can be controlled while synthesizing them in the laboratory. However, it is very difficult to synthesize highly monodisperse colloidal particles. At best, particles with a minimum of $2-5\%$ polydispersity can be prepared in the laboratory. The concentration of the colloidal particles is expressed by a general parameter called the volume fraction ϕ. For a colloidal suspension of monodisperse particles, $\phi = \frac{4}{3}\pi R^3 n_c$, where R is the radius of the monodisperse particle. For a polydisperse suspension $\phi = \frac{4}{3}\pi < R >^3 n_c$, where $< R >$ is the mean radius and n_c is the number density of the colloidal particle [11]. When the volume fraction ϕ of the colloidal particles in a suspension increases, the suspension becomes more viscous. The viscosity η of a very dilute colloidal suspension ($\phi < 0.05$) can be

related with the particle volume fraction ϕ by the Einstein's relation: $\eta = \eta_0(1 + 2.5\phi)$ [12]. Here, η_0 is the viscosity of the suspending medium. At higher volume fractions, the relationship between η and ϕ deviates from linear behaviour. A colloidal particle in a suspension can be stabilized by introducing some charges on their surface during the synthesis process [13]. The resultant electrostatic repulsion between the particles prevents the formation of aggregates. In some experiments, we need to stabilise the suspension constituted by large particles against gravitational settling. This is achieved by matching the density of the dispersing medium with the dispersed particles [14]. If the dispersed particles are less dense than the dispersing medium, they will form a creamy layer over the dispersing medium. A denser dispersed particle, on the other hand, will tend to sediment.

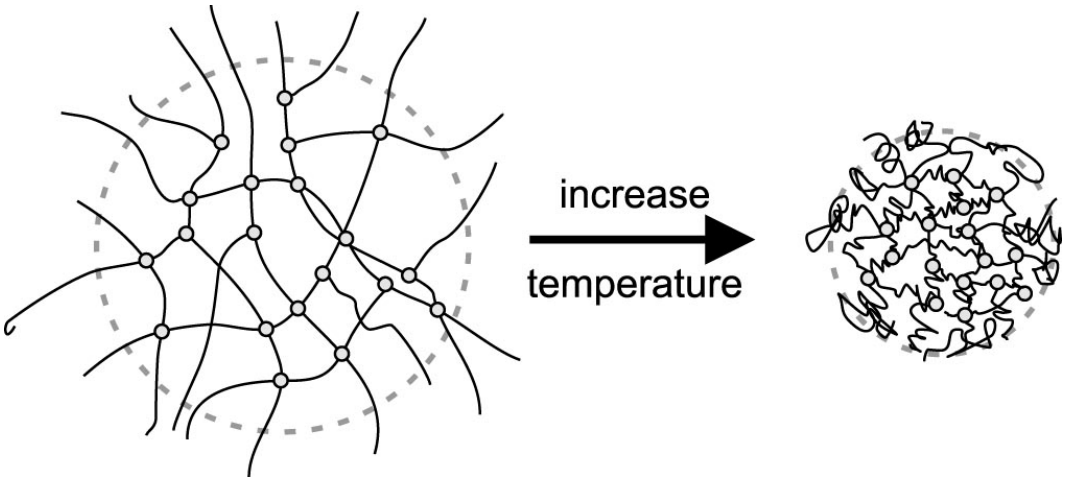

Figure 1.1: Cartoon of a thermoresponsive PNIPAM hydrogel particle. This figure is adapted from [16]. PNIPAM chains are crosslinked at certain points to form a spherical particle. At low temperatures, the particle size is larger due to the stretching of the polymer chains. When the temperature is increased, the particle shrinks to a smaller size due to the coiling up of the polymer chains.

1.2 Thermoresponsive Poly(*N*-isopropylacrylamide) (PNIPAM) hydrogel particles

Thermoresponsive poly(*N*-isopropylacrylamide) (PNIPAM) hydrogel particles are spherical in shape and consist of crosslinked PNIPAM polymer chains and water (figure 1.1) [15, 16]. Water inside the particle exists in two different physical states. Water molecules associated with the polymer chains are immobilized due to the hydrogen bonding between the water molecules and the amide groups of PNIPAM, while the water molecules away from the polymer chains are free [17]. PNIPAM hydrogel particles in water undergo a reversible volume phase transition above the lowest critical solution temperature (LCST) due to the switching between hydrophilic and hydrophobic states [18, 19]. The LCST of a PNIPAM particle is decided by the enthalpy of hydrogen bond formation between the water molecule and the amide groups of PNIPAM polymer chains. At low temperatures, the reorientation of water molecules around the amide group of PNIPAM results in a decrease in entropy of the system. As a consequence, the enthalpy of hydrogen bonding between the water molecule and the amide group of PNIPAM particle dominates the Gibb's free energy, causing the PNIPAM particle to absorb water and swell. At temperatures above the LCST, the increase in entropy of the system forces the PNIPAM particle to release water. As a result, PNIPAM particles shrink to smaller sizes (figure 1.1). In general, PNIPAM hydrogel particles are synthesized by the emulsion polymerization reaction [20–22]. Polymerization of a monomer is initiated in the presence of a free radical generated during the heating of a persulfate salt. PNIPAM hydogel particles of different sizes varying from nanometers to micrometers can be synthesized by varying the concentration of the surfactant [11, 23]. The particle size is also influenced by the initiator concentration, reaction temperature, monomer-to-crosslinker ratio and monomer concentration [24].

PNIPAM hydrogel particles in their dried states can be viewed under an electron microscope (figure 1.2(a)) [11, 25]. The particles in their swollen state can also be imaged by bright-field microscopy (figure 1.2(b)) or, if they are dyed, by confocal

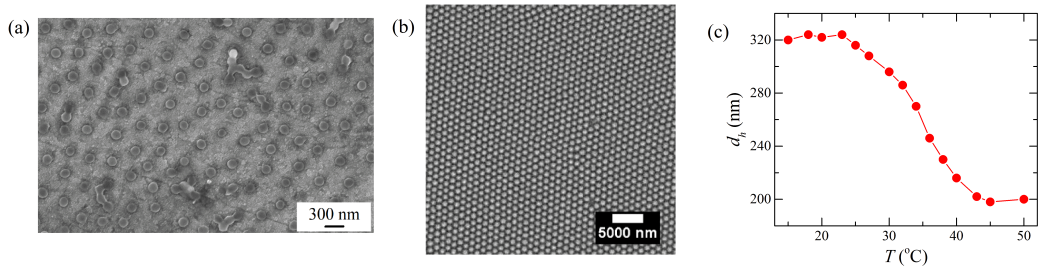

FIGURE 1.2: (a) Scanning electron micrograph of PNIPAM particles of size 0.14 μm in dry state. (b) Bright-field micrograph of a colloidal crystal of PNIPAM particles of size 1.1 μm. This figure is adapted from [16]. (c) Hydrodynamic diameter d_h of PNIPAM particles in an aqueous media measured by dynamic light scattering as a function of temperature T. The sizes of these particles in the fully swollen ($T \leq 23°$C) and fully shrunken states ($T \geq 45°$C) are respectively, 320 and 200 nm.

microscopy [26, 27]. Thermoresponsive behavior of these particles can be studied by measuring their hydrodynamic diameters, d_h, as a function of temperature, $d_h(T)$, using dynamic light scattering. The $d_h(T)$ curve of PNIPAM hydrogel particles in a dilute aqueous suspension is plotted in figure 1.2(c). In this curve, the plateaus at lower and higher temperatures respectively indicate the fully swollen and shrunken states of the particles. At the LCST ($\approx 34°$C), particles collapse and the diameter of the particles decreases rapidly to a new and lower high temperature plateau value. The swelling ratio, which is defined as the ratio of the particle diameters measured at the lowest and highest temperatures, is used to characterize the stiffness of the PNIPAM hydrogel particles [15, 28]. The stiffness of these particles can be controlled by varying the concentrations of surfactant and crosslinker during the polymerization reaction [29].

The volume fraction of PNIPAM hydrogel particles in an aqueous medium can be varied by changing the temperature of the medium without changing the particle number density [15, 30]. This property presents a unique advantage over temperature-insensitive polystyrene, silica and PMMA particles for studying the dynamics of aqueous suspensions of colloidal particles approaching kinetic arrest [16]. Since a tagged PNIPAM particle in an aqueous suspension can be observed and tracked at different volume fractions by varying the suspension temperature, the exploration of several

different samples synthesized at different volume fraction can be avoided. The structural and dynamical behaviours of suspensions of PNIPAM particles can be tuned by changing the suspension temperature [31–33].

As discussed in the previous section, the particle concentration in a hard sphere suspension is quantified by the volume fraction $\phi = n_c V$, where n_c is the number density and V is the volume of each particle. Above the random close packing volume fraction of undeformed monodisperse spheres ($\phi_{rcp} = 0.64$), soft PNIPAM particles start deforming in the presence of the neighboring particles [28, 34]. Since the volume fraction ϕ does not account for the particle deformations of these soft particles, a modified parameter called the effective volume fraction ϕ_{eff} is used to quantify the particle concentration. ϕ_{eff} is related to the number density of the particles by the relation $\phi_{eff} = n_c V_d$ [28]. Here, $V_d = \pi <d_h>^3/6$ is the volume of an undeformed PNIPAM particle of mean hydrodynamic diameter $<d_h>$ in a very dilute suspension at a temperature below LCST. In dilute suspensions, PNIPAM hydrogel particles can be treated as hard spheres as their volume is independent of concentration [28].

1.3 Janus particles

Janus particles are named after the ancient Roman God Janus Bifrons, who has two faces gazing into the past and the future (figure 1.3(a)). The concept of a Janus particle was first presented by Pierre-Gilles de Gennes in his Nobel Lecture in 1991 [35]. Janus particles form a special class of colloidal particles with two different surfaces or functionalities on their two opposite faces. Figure 1.3(b) shows the cartoon of a spherical Janus particle. The faces A and B of the particle have different physical and chemical properties. For example, if face A is hydrophilic, then face B will be hydrophobic [36]. The particles can also have two faces characterized by different charges, fluorescence or magnetic properties [37, 38]. Janus particles of various sizes, shapes and properties have important applications in biomedical research, textiles, sensors, stabilization of emulsions etc [39–41]. Two main aspects to consider while synthesizing Janus par-

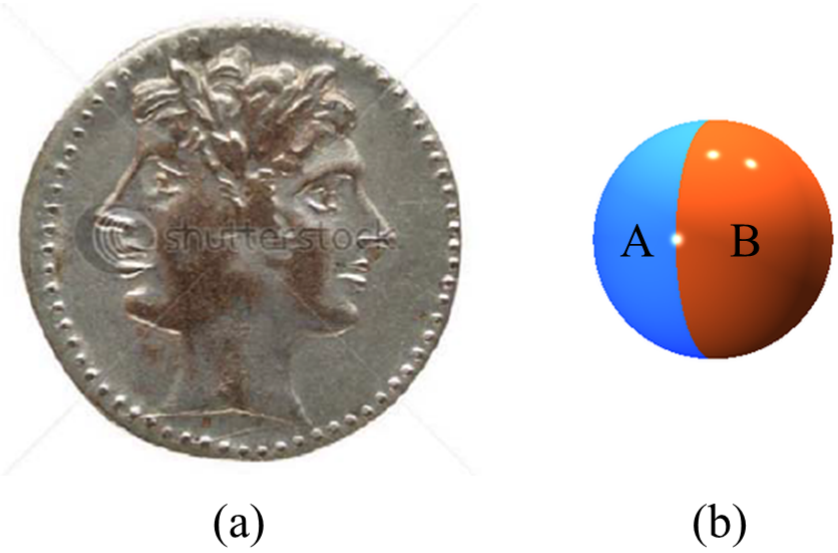

FIGURE 1.3: (a) An image of Janus Bifrons engraved on an ancient Roman coin. This figure is adapted from www.storyblocks.com. (b) Cartoon of a spherical Janus particle with two distinct faces A and B that possess two surfaces with different physical or chemical properties.

ticles are to control the relative areas of the two faces of the particle having different physical or chemical properties and to increase the yield of the particles [42]. Recently, three major methods (masking, self-assembly and phase separation) have been used for the synthesis of Janus particles. Of these methods, masking is one of the easiest and most convenient techniques accessible to us. A schematic of the synthesis of spherical Janus particles by masking is shown in figure 1.4. In this method, one side of the particle is protected by a masking agent while the unprotected side is modified. The modified particles are then removed from the masking agent and the resultant Janus particles are collected. Evaporative deposition and the phase interface method are the two common masking techniques used for the synthesis of Janus particles. Evaporative deposition involves the deposition of an evaporated material on a target object in vacuum. An example of an evaporative deposition technique is described by Howse et al. for the synthesis of platinum coated Janus particles [43]. They deposited a thin layer

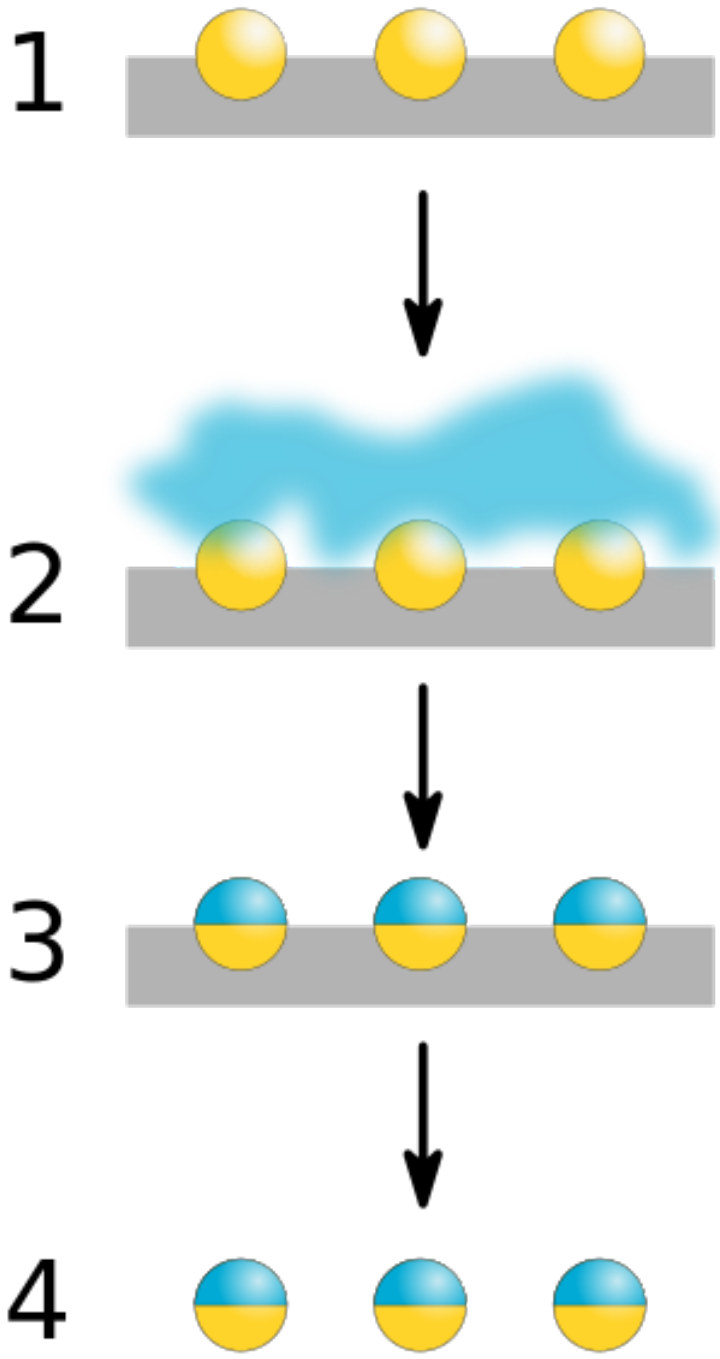

Figure 1.4: Schematic diagram for the synthesis of Janus particles by the masking method. (1) A monolayer of spherical particles is placed over a substrate in such a way that only one hemisphere is exposed. (2) A chemical is deposited on the exposed surface. (3) The chemical is coated over the particle which changes its property. (4) Janus particles are produced by removing the modified particles from the masking agent. This figure is adapted from www.en.wikipedia.org/wiki/Janus_particles.

(5.5 nm thickness) of platinum on one side of polystyrene microspheres by evaporating platinum onto the microspheres that were coated on a glass substrate. The phase interface method involves trapping of homogeneous particles at the interface of two immiscible phases (liquid-liquid, liquid-solid or gas-liquid interfaces). An example of a liquid-liquid interface method is the addition of magnetite nanoparticles in an oil-water emulsion. Further addition of silver nitrate into the above mixture results in the deposition of silver on the surface of the magnetite nanoparticles [44].

The property of a Janus particle is decided by its chemistry. In this thesis, we use platinum coated Janus particles, with the platinum acting as a catalyst for the decomposition of hydrogen peroxide that is present in the medium. Spherical colloidal particles coated with platinum on one hemisphere act as nanomotors in hydrogen peroxide solution due to the catalytic decomposition of hydrogen peroxide into water and oxygen [45]. The self-propulsion mechanism of these nanomotors is decided by the particle architecture, size and nature. One of the self-propulsion mechanisms is self-diffusiophoresis. In this mechanism, a spherical colloidal particle with an asymmetric distribution of catalyst (platinum) on its surface self propels in the reactant medium (hydrogen peroxide) due to the asymmetric distribution of the reaction products around the particle [43, 46]. The propulsion velocity of Janus particles increases with the reactant concentration [43].

1.4 Interparticle interactions in colloidal systems

The interaction forces acting between colloidal particles in a suspension play a significant role in determining the properties of the suspension at high particle volume fractions. For hard sphere colloidal suspensions, the interaction potential between two particles has the simplest form: $V(r) = \infty$ for $r \leq \sigma$ and $V(r) = 0$ for $r > \sigma$ [3]. Here, r is the distance between the centers of two interacting spherical particles and σ is the sum of their radii. A dilute colloidal suspension has no potential energy between the

particles and the dynamics is solely governed by the particle volume fraction. However, the dynamics of concentrated colloidal suspensions composed of charged particles is regulated by the various interactions present between them such as electrostatic repulsion, van der Waals, hydrophobic attractions etc [47–49].

1.4.1 Electrostatic repulsion

When a colloidal particle with a surface charge is dispersed in an electrolyte solution, the counterions in the solution are attracted towards the opposite electric charges of the particle and screen the charged surface of the colloid (figure 1.5). However, the counterions always remain in a diffused state around the particle because of thermal fluctuations. This diffuse layer of counterions, together with the particle's surface charges, form the electric double layer (EDL) (figure 1.5) [1]. When charged particles in a suspension approach each other, their electric double layers overlap at a particle separation of less than twice the EDL's length. Due to the interaction between the electric double layers surrounding the particles, a screened electrostatic repulsion between the colloidal particles arises. This is known as electric double layer repulsion. The length scale over which the influence of the EDL repulsion is experienced is called the Debye screening length ($1/\kappa$). The Debye screening length decreases with the increase in electrolyte concentration n in a suspension and is related with n by the following relation [50]:

$$\frac{1}{\kappa} = \left[\frac{\epsilon_0 \epsilon_r k_B T}{\sum_i (z_i e)^2 n_i} \right]^{1/2} \tag{1.1}$$

Here, ϵ_0 is the permittivity of vacuum, ϵ_r is the relative permittivity of the medium, k_B is the Boltzmann constant, T is the suspension temperature, e is the charge of an electron and z_i is the valency of the ith ion species of concentration n_i.

The Stern layer is situated near the particle's surface and contains counterions that are attracted to the electric charges on the particle [51, 52] (figure 1.5). When a colloidal particle moves in the dispersion medium, a layer of the surrounding solvent remains attached to the particle. The boundary of this layer is called the slipping plane

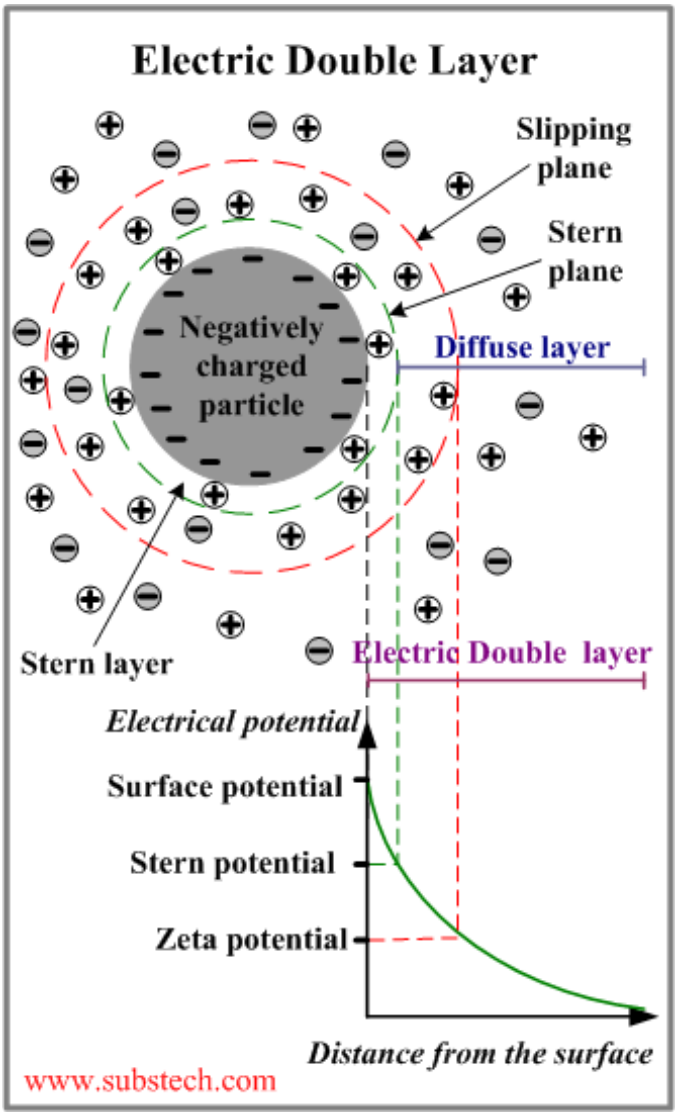

Figure 1.5: Schematic diagram of the electric double layer (EDL) of a negatively charged colloidal particle in a suspension. The layer close to the surface of the particle is the Stern layer. A layer of counterions next to the Stern layer and containing the slipping plane is called the diffuse layer. The electric potential at the slipping plane is called the zeta potential. The electric potential decreases as a function of distance from the surface of the particle. This figure is adapted from www.substech.com website.

(figure 1.5). The value of the electric potential at the slipping plane is called the zeta potential [1, 51, 53]. As it is very difficult to measure the exact potential at the surface of the colloidal particle, an approximate estimate of the surface charge on the particles can be obtained by measuring the zeta potential at the slipping plane. As a good approximation, the zeta potential can be considered as the potential at the Stern layer.

1.4.2 van der Waals attraction

The van der Waals interaction is attractive in nature and acts between atoms, molecules and surfaces [54]. Two atoms or molecules having permanent dipole moments attract each other through dipole-dipole interactions [55]. However, in neutral atoms and molecules, an induced dipole moment is generated due to the rapid motion of the electrons around the nucleus. The London dispersion interaction between the induced dipoles arises as they couple with each other to minimize the interaction energy [56]. The van der Waals attraction between two colloidal particles is the sum of all the pairwise London interactions that arise for all pairs of atoms in the two particles [57]. The effective range of the van der Waals interaction can vary from 0.1 nm to 10 nm [58]. The strength of this interaction depends on the dielectric properties of the colloidal particles and the dispersion medium. The van der Waals interaction energy between two spherical particles of radii R_1 and R_2 separated by a distance r is as follows [50]:

$$W_{vdW} = -A_H\left[\frac{R_1R_2}{(R_1+R_2)6r}\right] \tag{1.2}$$

Here, A_H is the Hamaker constant which depends on the material properties. It can be positive or negative in sign depending on the intervening medium.

1.4.3 Hydrophobic attraction

A hydrophobic surface has no polar or ionic groups or hydrogen-bonding sites. As a result, there is no affinity for bonding between water molecules and the hydrophobic surface. As the orientation of water molecules around a hydrophobic surface is entropically unfavorable, two hydrophobic molecules tend to come together by pairwise attraction in order to minimize the free energy of the system. Water molecules confined in a gap between the hydrophobic surfaces are unable to form clusters larger than a certain size. For an extremely narrow gap, the free energy of water molecules

inside the gap increases when compared with those in bulk [59]. This give rise to an attractive force between hydrophobic surfaces due to which the water molecules migrate from the gap to the bulk water. Attraction between the hydrophobic surfaces has been measured directly [60] and can extend upto a range of 80 nm [61]. The hydrophobic attraction is much stronger than the van der Waals force and occurs at a larger separation [62].

1.5 Colloidal jamming

Hard sphere colloidal suspensions are the simplest model systems used for studying the physics of the jamming transition. The increase in the number of colloidal particles in a suspension increases the suspension packing fraction, with the system entering into the jammed state above a specific particle volume fraction. As a result, colloidal suspensions undergo a transition from a liquid to a solid state with increase in volume fraction of the particles. Liquid-solid structural arrest also occurs in granular media, polymers and atomic/molecular systems. While the driving parameter for the disordered state varies from system to system, a common phenomenology exists between them [63–65]. Liu and Nagel have proposed a conceptual phase diagram for the jamming transition to unify the description of the behaviors of jammed systems [66]. The phase diagram is shown in figure 1.6(a). The axes of this phase diagram are applied stress σ, temperature T and inverse of particle density or volume fraction $1/\phi$. This phase diagram suggests that jamming in a system can be achieved when the number density of constituent particles increases. The jammed system can then be unjammed by applying stress or increasing temperature. This phase diagram attempts to unify a wide range of structural arrest phenomena seen in a variety of materials [66]. For attractive particle systems, the experimental phase jamming phase diagram differs somewhat from the one proposed by Liu and Nagel (figure 1.6(b)) [67]. It is to be noted that the phase boundaries have opposite curvatures to those suggested in [66]. This phase diagram indicates that apart from the applied stress and density, the ratio of

the thermal energy k_BT and the attractive potential U of the particles is also important for the jamming of colloidal suspensions. In the limit of low stresses and high volume fractions, the system exhibits a glass like amorphous structure at a very low attractive potential U or high k_BT/U values. On the other hand, in the limit of low stress σ and volume fraction ϕ, the attractive colloidal system undergoes irreversible aggregation leading to the formation of fractal clusters [68]. At higher volume fractions, strongly attractive particles form sintered solids with large yield stresses.

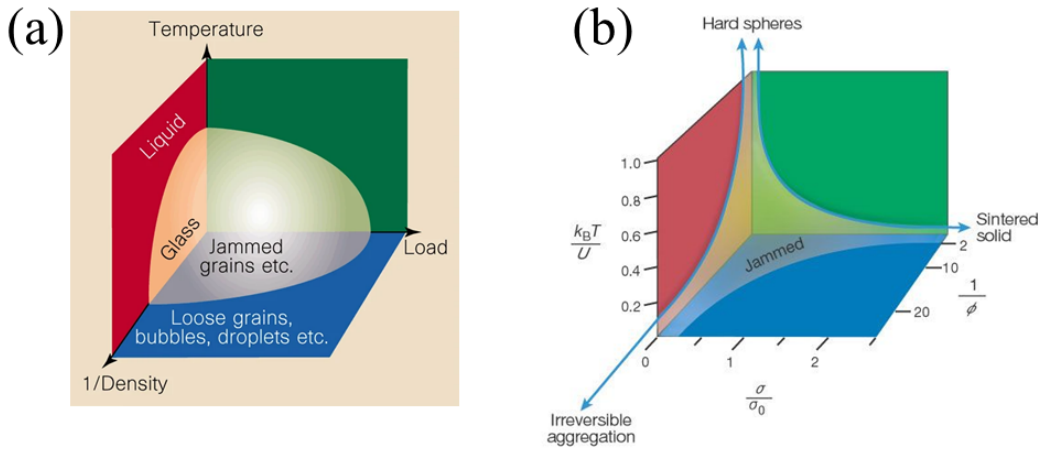

Figure 1.6: (a) Jamming phase diagram proposed by Liu and Nagel [66]. The phase diagram is plotted in the planes of load σ, temperature T and the inverse of density $1/\phi$. This figure is adapted from [66]. (b) The jamming phase diagram for attractive colloidal particles proposed by Trappe et al. in the planes of $1/\phi$, k_BT/U and σ/σ_0 [67]. Here, U is the attractive potential between two colloidal particles of diameter a and $\sigma_0 = k_BT/a^3$.

For athermal systems, the jamming transition is defined at $T = 0$. The phase change (liquid to solid) for this system occurs at a critical packing fraction near which various scaling laws have been predicted [66, 69, 70]. For thermal systems ($T > 0$), the jamming transition is sometimes referred to as the dynamic glass transition, which

is defined to arise when the particle relaxation time scale exceeds 100 s [71]. Thermoresponsive PNIPAM colloidal particles in suspension are a suitable alternative to hard spheres for studies of jammed systems due to the easy tunability of their packing fraction by changing the suspension temperature [16]. The structural signatures of jamming have been reported in binary mixtures of PNIPAM particles in two dimensions [72]. PNIPAM suspensions show behavior characteristic of a glass near their jamming point when the volume fraction of the constituent particles is varied by tuning the suspension temperature [72].

1.6 Phases in colloidal suspensions

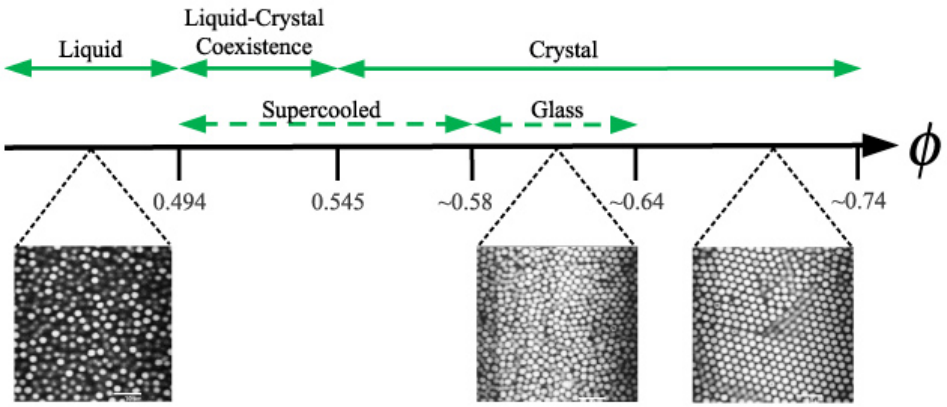

FIGURE 1.7: Top: Phase diagram of suspensions of monodisperse hard spheres as a function of volume fraction ϕ. Green solid arrows indicate equilibrium states, while dashed arrows are out of equlibrium states of these particles in a suspension. Samples of particle size polydispersity of at least 8% is required for the existence of the glassy state (dashed line). A monodisperse sample eventually crystallizes (solid line) when ϕ is increased. Bottom: Confocal microscope images of the sequence of phases in a colloidal suspension with 5% particle size polydispersity. This figure is adapted from [3].

The structure and dynamics of colloidal suspensions can be studied using several experimental techniques such as microscopy, rheology and light scattering [8, 73–75]. The phase behavior of concentrated colloidal suspensions was first studied experimentally by Pusey and van Megan in a suspension of nearly hard sphere PMMA particles

[34, 76]. The phase behavior in such colloidal suspensions is determined by the excluded volume interactions between the constituent particles [77]. The phase diagram of hard sphere colloidal suspensions is shown in figure 1.7 as a function of volume fraction ϕ [3]. It is seen that the suspension always remains in the liquid state below its freezing point $\phi_{freeze} = 0.494$. A coexistence of liquid and crystalline phases is observed when the volume fraction is increased above ϕ_{freeze}. With further increase in ϕ, the system slowly enters into the crystalline phase [34, 78]. However, a colloidal suspension in a liquid state enters a supercooled or glassy state when the volume fraction is increased at a fast rate. When the particle volume fraction is increased rapidly, a supercooled region arises for volume fractions $0.494 \leq \phi < 0.58$, while the glassy region appears between $0.58 < \phi < 0.64$ [3]. It has been observed experimentally that the system enters into glassy state at $\phi = \phi_g \approx 0.58$, where ϕ_g is known as the glass transition volume fraction [76]. Instead of rapidly increasing the particle volume fraction, the glassy phase of almost monodisperse hard sphere suspensions can also be obtained by slowly increasing the particle volume fraction of a suspension comprising polydisperse particles. A suspension constituted by hard spheres with a particle size polydispersity around $8 - 10\%$ forms the glassy state at $\phi \approx 0.58$ [11, 76]. The upper bound of the glassy region is the random close packing volume fraction ϕ_{rcp}, the maximum density of a completely random sphere packing. The exact value of ϕ_{rcp} depends on the size polydispersity of the particles [79]. For $\phi > \phi_{rcp}$, domains of crystalline order appear in monodisperse hard sphere suspensions. In these suspensions, the volume fraction can be increased upto the limit of hexagonal close packing $\phi_{hcp} = 0.74$.

The increase in size polydispersity of the hard spheres in a suspension shifts the glass transition volume fraction ϕ_g to higher values [78, 80]. On the other hand, adding charges to the particles shifts ϕ_g to lower values [81, 82]. For soft and deformable particles, the glass transition volume fraction depends on the softness of the particles [11, 28]. Suspensions of these particles exhibit the glass transition at particle concentrations much above the ϕ_{rcp} value of monodisperse hard spheres. Depending on the volume fraction, suspensions of soft particles also exhibit other phases such

as a liquid-crystal coexistence phase [83]. At volume fractions below the glass transition concentration, suspensions of uncharged or screened colloidal particles exhibit gel phases, where the structure of the gel-network is mediated by attractive interactions such as hydrogen bonding, electrostatic and van der Waals attractions [84–86].

1.7 Features of colloidal system approaching jammed or kinetically arrested states

1.7.1 Growth of viscosity and relaxation times

The viscosity η of a liquid increases while cooling. If the liquid is cooled at a fast rate, the molecules do not get enough time to reorient into an ordered state and, instead, form a disordered state. When the viscosity of the liquid increases to 10^{13} poise, which is 10^{15} times the viscosity of water at room temperature [65], the system enters the glassy state. For colloidal suspensions, the viscosity increases with increase in volume fraction of the colloidal particles. The relative low shear viscosities, η/η_0, for various colloidal suspensions of nearly monodisperse hard spheres, is plotted as a function of particle volume fraction ϕ (figure 1.8) [3, 87–90]. Here η_0 is the viscosity of the pure solvent. From this figure, it can be noticed that the maximum change of viscosity is of the order of 10^4. Indeed, the viscosity increase observed in the colloidal glass transition is not as great as in the molecular glass transition.

Marshall et al. measured the viscosity of a colloidal suspension comprised of small silica hard spheres (radius < 300 nm) in a decahydronapthalene solvent using a stress controlled rheometer [91]. For all the silica particle sizes, they observed a gradual increase in the viscosity of the suspension with particle volume fraction ϕ, followed by a sudden dramatic increase above a certain volume fraction. They also found that the viscosity versus volume fraction curve was well described by the Doolittle equation

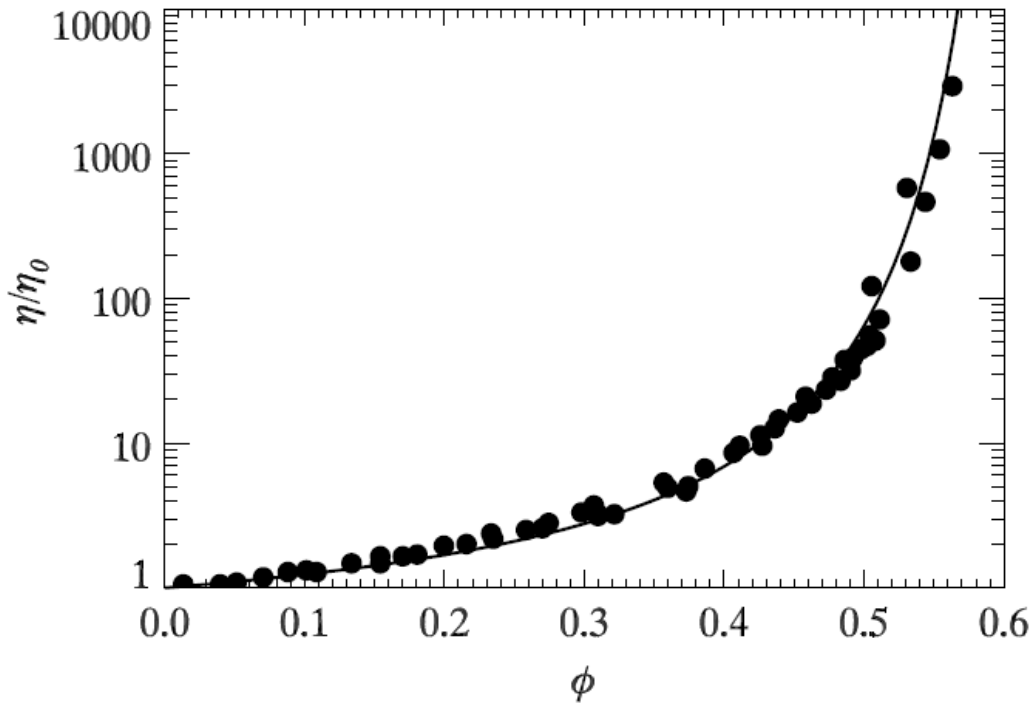

Figure 1.8: (a) The relative low shear viscosity η/η_0 is plotted as function of volume fraction ϕ for various colloidal suspensions of nearly monodisperse hard spheres. Here, η_0 is the viscosity of the pure solvent. The solid line is the fit to the equation 1.3. The data are taken from [3, 87–90].

[92],

$$\frac{\eta}{\eta_0} = C \exp\left[\frac{D\phi}{\phi_m - \phi}\right] \tag{1.3}$$

with $C = 1.2$, $D = 1.65$ and $\phi_m = 0.638$. Interestingly, the fitted value of $\phi_m = 0.638$ is close to the random close packing fraction of monodisperse hard speheres, ϕ_{rcp}, where all particle motion is expected to arrest.

The glass transition in colloidal suspensions is also associated with a dramatic increase in the microscopic relaxation time and a simultaneous significant decrease in diffusivity. For glassy colloidal suspensions, the long time self-diffusion coefficient $D_L(\phi)$ approaches zero while the microscopic relaxation time scale τ_α, obtained from the decay time of the self-intermediate scattering function, becomes large as the glass transition is approached [3, 93]. τ_α and D_L are related to the radius a of the colloidal particle by the relation: $\tau_\alpha \propto a^2/D_L$. The measurements of τ_α and D_L can therefore

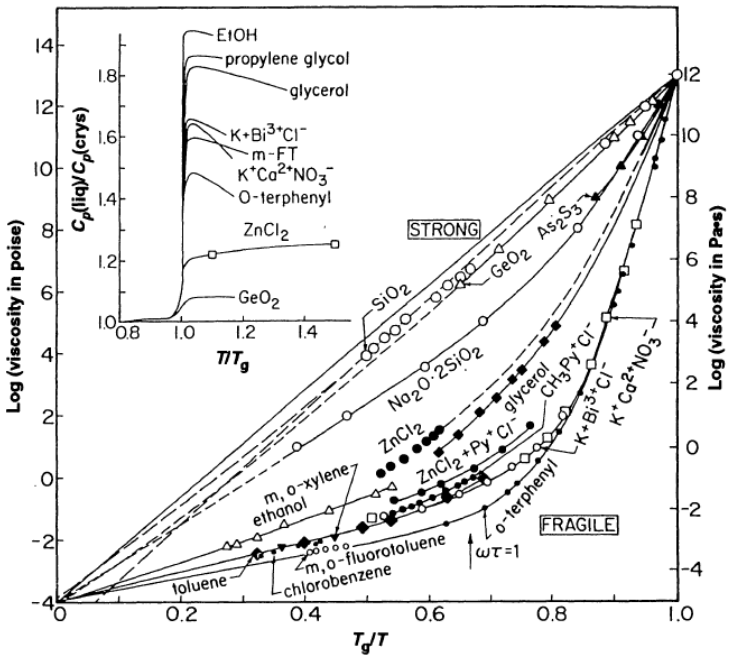

FIGURE 1.9: (a) The logarithm of the viscosity of molecular liquids is plotted as a function of the inverse of the temperature normalized by the glass transition temperature T_g/T. Straight solid lines in this plot show the Arrhenius dependence of viscosity on temperature observed in strong glass formers (SiO_2, GeO_2 etc). A non-Arrhenius dependence of viscosity with temperature is seen for fragile glass formers (o-terphenyl, toluene etc.) and is represented by curved solid lines. In the inset, specific heat C_p is plotted as a function T/T_g. C_p shows a jump at T_g. This figure is adapted from [65].

explain how the microscopic dynamics slow down near the glass transition [3].

1.7.2 Fragility

In molecular, polymer and colloidal glasses, the rate of growth of viscosity or the microscopic relaxation time scale varies between different samples. This difference is termed as the fragility [65]. The viscosity and microscopic relaxation time scales in a fragile glass former increase slowly over some range of control parameter and then grow dramatically as the glass transition is approached (figure 1.9). In contrast, 'strong' glasses exhibit Arrhenius behavior, where the logarithm of the viscosity (or time scale) grows linearly with inverse temperature $1/T$ as the glass transition is approached (figure 1.9) [65].

The fragility of molecular liquids can be obtained by fitting the viscosity versus temperature data to the Vogel-Fulcher-Tammann (VFT) equation [94–97]:

$$\frac{\eta}{\eta_0} = \exp\left[\frac{DT_0}{T - T_0}\right] \tag{1.4}$$

Here, η_0 is the viscosity of molecular liquids at large T and T_0, the Vogel temperature, indicates the temperature at which the viscosity diverges [98]. The parameter D is called the fragility parameter. The fragility, $1/D$, of glass forming liquids is defined as the deviation of the viscosity from Arrhenius growth upon cooling rapidly [65]. $1/D$ values are smaller for stronger glasses. For fragile molecular and polymer glasses, $1/D$ values are larger than 0.33 [65]. The origin of fragility still remains elusive despite many theoretical and experimental studies. A correlation is drawn between the fragility of a material and its physical properties i.e. Poissons ratio or the relative strength of its shear and bulk moduli [99]. The relation between fragility and the nature of the interaction potential has also been studied for model binary molecular and colloidal glass formers [28, 100]. For colloids, T is replaced with $1/\phi$ in equation 1.4. This results in the Doolittle equation with $C = 1$ [91]:

$$\frac{\eta}{\eta_0} = \exp\left[\frac{D\phi}{\phi_0 - \phi}\right] \tag{1.5}$$

Using the above definition, the values of D for hard sphere colloidal suspensions lie between $1 - 2$ [87, 91]. This formula is also applicable for microscopic relaxation time scales τ_α obtained from light scattering data by replacing η/η_0 with τ_α/τ_0 [101, 102]. The fragility of a colloidal suspension depends upon various parameters such as particle stiffness, size polydispersity and interaction potential between the particles [11, 28, 47].

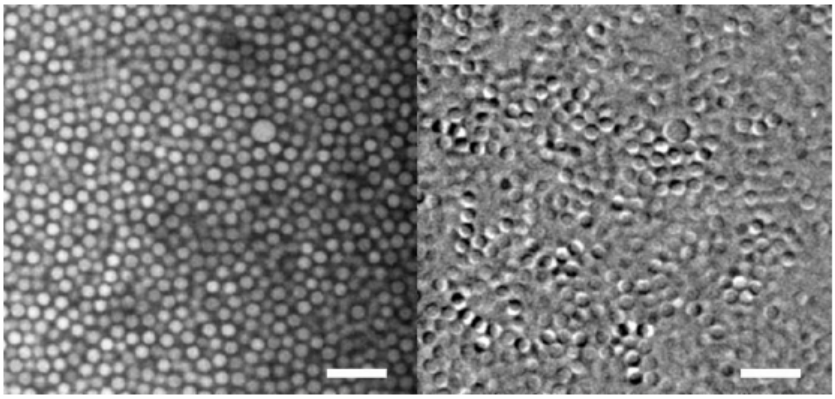

Figure 1.10: Left: Two dimensional confocal microscopy of a suspension of slightly charged polymethyl(methacrylate) (PMMA) particles at a volume fraction $\phi = 0.46$. Right: difference between the left image and an image taken 60 s later. In both images, the scale bar represents 10 μm. In the right image the grey region indicates zero movement of the particles, the black region indicates the smaller movement of the particles and the white region indicates the larger movement of the particles. This figure is adapted from [3].

1.7.3 Dynamical heterogeneity

When a liquid is rapidly quenched below its melting point such that crystallization is averted, some regions exhibit faster dynamics, *i.e.* they relax at a faster rate, than other regions. This behavior persists regardless of the spatial closeness of these regions [93, 103, 104] and is called dynamical heterogeneity. The length and time scales of a material exhibiting dynamical heterogeneity are coupled, that is, longer relaxation times are associated with larger number of particles moving in a group. This results from the cooperative motion of the particles (*i.e.* large clusters of molecules need to cooperate more in order to rearrange) near the glass transition [105]. Cooperative motion of a colloidal suspension is seen in figure 1.10 [3, 106]. The left image shows a two dimensional confocal microscope image of a suspension of PMMA particles at a volume fraction 0.46. The right image shows the difference between the particle positions between the left image and an image taken after 60 s. The grey regions in the right image indicate the places where particles move very little during this period of time, while the black and white regions indicate the movement of particles in a group. As the glass transition is approached, the regions of rearranging particles grow larger,

but the displacements during the rearrangements are smaller [107]. Evidence of spatial heterogeneity of a colloidal suspension has been obtained from microscope images of particles in several experiments [108–110].

The cooperative motion of the particles is very relevant to the cage trapping and cage rearrangement phenomena. At short time scales, particles move inside a cage due to Brownian motion. However, this motion of the particle is constrained due to collisions with the neighboring particles in a cage [111, 112]. At longer time scales, the cages relax and the system rearranges [107]. As the glass transition is approached, the sizes of the cooperative groups of particles and the time scales associated with their motion increase [11, 113, 114]. The growing length scale can extend upto $\sim 4-5$ particle diameters and rearrangements can involve upto ~ 200 particles [11, 114, 115]. The movement of a larger number of particles in a coordinated fashion is difficult and occurs less often. This intuition connects directly to the slowing time scales for the diffusion of particles in jammed environments. In this sense, dynamical heterogeneity and the glass transition are strongly connected to each other [3]. The evidence of the above statement comes from simulations that show the presence of dynamical heterogeneities near the glass transition [116–118]. Apart from the spatial variations in mobility, dynamical heterogeneity can also be studied from the temporal fluctuations of particle mobility [119, 120]. This can be quantified with a four-point susceptibility function called χ_4 [118, 121]. This function is related to the cooperative motion of the particles and can be used to find a time scale corresponding to the dynamical heterogeneity. The analysis has been successfully applied to colloidal experiments [122–124].

1.8 Soft particle suspension rheology

Suspensions of soft particles such as hydrogels, micelles, vesicles and biological cells are ubiquitous in nature and have been widely used in the industry. While the rheological behavior of suspensions of hard spheres such as polymethyl mathacrylate (PMMA),

polystyrene and silica particles is reasonably well understood, a detailed understanding of soft particle suspension rheology remains elusive [125]. The microstructure and flow behavior of soft particle suspensions are complex due to the multiple influences of single particle properties such as particle swelling and interparticle interactions on their structures and dynamics [83, 126]. As a result, the relation between single particle properties and macroscopic behavior needs to be thoroughly investigated. A model system of spherical PNIPAM hydrogel particles is used in this thesis to elucidate the influence of particle volume fraction and swelling behavior on the flow behavior of soft particle suspensions of different concentrations.

Studies of the flow behavior of suspensions of soft hydrogel particles demonstrate that soft particles behave like hard spheres at lower suspension volume fraction ϕ ($\phi \leq 0.4$) and deviate from this behavior when the volume fraction is increased further [127, 128]. The viscosity of suspensions of soft particles is strongly dependent on the particle volume fraction and the interaction potential between the particles. At dilute concentrations ($\phi < 0.02$), the viscosity (η) of suspensions of soft particles is related to the volume fraction by Einstein equation $\eta = \eta_s(1 + 2.5\phi)$, where η_s is the viscosity of the suspension medium [12]. At semi-dilute concentrations ($\phi < 0.15$), the hydrodynamic interaction between the particles are relevant and appear in the expression for viscosity in the form of a term of order ϕ^2 [129]. As a result, in the semi-dilute regime, the Batchelor's equation $\eta = \eta_s(1 + 2.5\phi + b\phi^2)$ establishes the relation between viscosity and volume fraction [130]. The constant b can have a range of values from 4.2 to 6.2 [130–132].

When the volume fraction is increased above 0.2, the MPQ model (developed by Maron, Pierce and Quemada by taking into account the multi-body particle interactions) predicts $\eta = \eta_s\left(1 - \frac{\phi}{\phi_m}\right)^{-2}$ and explains well the rise of viscosity with volume fraction [133, 134]. At volume fraction above ϕ_{rcp}, the soft hydrogel particles in a suspension deform due to the presence of neighboring particles [28]. As a consequence, these particles pack more efficiently, resulting in increase in the viscosity η of suspensions of these particles with increase in volume fractions above ϕ_{rcp}. The

behavior of the viscosity of the suspensions with variation in volume fraction is decided by the stiffness of the particles [10, 28]. The viscosity of suspensions of soft particles increases exponentially with volume fraction. The exponential dependence of η with ϕ ($\eta = \eta_s \exp[A\phi]$) is analogous to the Arrhenius behavior observed in strong molecular glass-formers [10, 28]. Here A is a constant and $\eta_s = \eta$ for $\phi = 0$. However, suspensions of relatively stiff particles show the super-Arrhenius dependence of viscosity with volume fraction, typically observed in fragile molecular glass-formers. The dependence of viscosity on volume fraction in these suspensions is well described by Vogel-Fulcher-Tammann (VFT) law: $\eta = \eta_s \exp(\frac{D\phi}{\phi_0 - \phi})$, where $1/D$ is the fragility which accounts for the deviation of the viscosity from an Arrhenius dependence on volume fraction [10, 28, 102].

References

[1] R. J. Hunter, *Foundations of Colloid Science*, Clarendon Press, Oxford, 1995, vol. I.

[2] W. B. Russel, D. A. Saville and W. R. Schowalter, *Colloidal dispersions*, Cambridge university press, 1992.

[3] G. L. Hunter and E. R. Weeks, *Rep. Prog. Phys.*, 2012, **75**, 066501.

[4] W. C. K. Poon, *Colloidal suspensions*, Clarendon press, Oxford, 2012.

[5] K. V. Hoecke, K. A. C. De Schamphelaere, P. V. D. Meeren, Stéphane Lcucas and C. R. Janssen *Environmental Toxicology and Chemistry*, 1948, **27**, 2009.

[6] G. E. Uhlenbeck and L. S. Ornstein, *Phys. Rev.*, 1930, **36**, 823.

[7] P. Varadan, and M. J. Solomon, *Langmuir*, 2003, **19**, 509512.

[8] E. R. Weeks, J. C. Crocker, A. C. Levitt, A. Schofield and D. A. Weitz, *Science*, 2000, **287**, 627631.

[9] M. Baus, L. F. Rull and J. P. Ryckaert *Observation, Prediction and Simulation of Phase Transitions in Complex Fluids*, Kluwer Academics Publishers, 1994.

[10] S. K. Behera, D. Saha, P. Gadige and R. Bandyopadhyay, *Phys. Rev. Materials*, 2017, **1**, 055603.

[11] W. C. K. Poon, E. R. Weeks and C. P. Royall, *Soft Matter*, 2012, **8**, 21-30.

[12] A. Einstein, A new determination of the molecular dimensions, *Annalen Der Physik*, 1906, **19(2)**, 289-306.

[13] J. Hierrezuelo, A. Sadeghpour, I. Szilagyi, A. Vaccaro and M. Borkovec, *Langmuir*, 2010, **26(19)**, 15109-15111.

[14] C. P. Royall, R. v. Roij and A. v. Blaaderen *J. Phys. Condens. Matter*, 2005, **17**, 23152326.

[15] B. R. Saunders and B. Vincent, *Adv. Colloid Interface Sci.*, 1999, **80**, 1-25.

[16] P. J. Yunker, K. Chen, M. D. Gratale, M. A. Lohr, T. Still and A. G. Yodh, *Rep. Prog. Phys.*, 2014, **77**, 056601.

[17] A. K. Lele, M. M. Hirve, M. V. Badiger and R. A. Mashelkar, *Macromolecules*, 1997, **30**, 157-159.

[18] M. Heskins and J. E. Guillet, *J. Macromol SCi.*, 1968, **2**, 1441.

[19] Y. Hirokawa and T. Tanaka, *J. Chem. Phys.*, 1984, **81**, 6379.

[20] R. Pelton, *Adv. Colloid Interface Sci.*, 2000, **85**, 1-33.

[21] R. H. Pelton, H. M. Pelton, A. Morphesis and R. L. Rowell, *Langmuir*, 1989, **5**, 816-818.

[22] X. Wu, R. H. Pelton, A. E. Hamielec, D. R. Woods, and W. McPhee, *Colloid & Polym Sci.*, 1994, **272**, 467-477.

[23] W. McPhee, K. C. Tam and R. Pelton, *J. Colloid and Interface Science*, 1993, **156**, 24.

[24] J. Gao and B. J. Frisken, *Langmuir*, 2003, **19**, 5217-5222.

[25] R. H. Pelton and P. Chibante, *Colloids and Surfaces*, 1986, **20**, 241-256.

[26] Z. Meng, J. K. Cho, V. Breedveld and L. A. Lyon, *J. Phys. Chem. B*, 2009, **113**, 4590-4599.

[27] M. Kwok and T. Ngai, *J. Colloid and Interface Sci.*, 2016, **461**, 409418.

[28] J. Mattsson, H. M. Wyss, A. Fernandez-Nieves, K. Miyazaki, Z. Hu, D. R. Reichman and D. A. Weitz, *Nature*, 2009, **462**, 83.

[29] H. Senff and W. Richtering, *Colloid Polym Sci*, 2000, **278**, 830-840.

[30] Y. Han, N. Y. Ha, A. M. Alsayed, and A. G. Yodh, *Phys. Rev. E*, 2008, **77**, 041406.

[31] H. Senff and W. Richtering, *J. Chem. Phys.*, 1999, **111**, 1705.

[32] A. M. Alsayed, M. F. Islam, J. Zhang, P. J. Collings and A. G. Yodh, *Science*, 2005, **309**, 1207.

[33] L. A. Lyon and A. Fernandez-Nieves, *Annu. Rev. Phys. Chem.*, 2012, **63**, 25.

[34] P. N. Pusey and W. Van Megen, *Nature*, 1986, **320**, 340.

[35] P.-G. de Gennes, *Angew. Chem. Int. Ed. Engl.*, 1992, **31**, 842.

[36] T. Ouchi, R. Nakamura, T. Suzuki, H. Minami, *Ind. Eng. Chem. Res.*, 2019, **XXXX**, XXX, XXX-XXX.

[37] L. Hong, A. Cacciuto, E. Luijten and S. Granick, *Nano Letters*, 2006, **6**, 2510-2514.

[38] B. Ren, A. Ruditskiy, J. H. Song, I. Kretzschmar, *Langmuir*, 2012, **28**, 1149-1156.

[39] A. Synytska, R. Khanum, L. Ionov, C. Cherif and C. Bellmann, *Appl. Mater. Interfaces*, 2011, **3**, 1216-1220.

[40] M. Yoshida, K. Roh, S. Mandal, S. Bhaskar, D. Lim, H. Nandivada, X. Deng and J. Lahann, *Adv. Mater.*, 2009, **21**, 4920-4925.

[41] S. Hu and X. Gao, *J. Am. Chem. Soc.*, 2010, **132**, 7234-7237.

[42] S. Jiang, Q. Chen, M. Tripathy, E. Luijten, K. S. Schweizer and S. Granick, *Adv. Mater.*, 2010, **22**, 10601071.

[43] J. R. Howse, R. A. L. Jones, A. J. Ryan, T. Gough, R. Vafabakhsh and R. Golestanian, *Phys. Rev. Lett.*, 2007, **99**, 048102.

[44] H. Gu, Z. Yang, J. Gao, C. K. Chang, B. Xu, *J. Am. Chem. Soc.*, 2005, **127**, 34-35.

[45] F. Valadares, Y. Tao, N. S. Zacharia, V. Kitaev, F. Galembeck, R. Kapral and G. A. Ozin, *small*, 2010, **6**, 565-572.

[46] R. Golestanian, T. B. Liverpool, and A. Ajdari, *Phys. Rev. Lett.*, 2005, **94**, 220801.

[47] Z. Zhang, P. J. Yunker, P. Habdas and A. G. Yodh, *Phys. Rev. Lett.*, 2011, **107**, 208303.

[48] J. Kaldasch, B. Senge and J. Laven, *Journal of Thermodynamics*, 2014, **2015**, 1-10.

[49] B. Ruzicka and E. Zaccarelli, *Soft Matter*, 2011, **7**, 1268.

[50] J. N. Israelachvili, *Intermolecular and Surface Forces*, Academic Press: New York 2010.

[51] H. v. Olphen, *An Introduction to Clay Colloid Chemistry*, Wiley: New York 1977.

[52] O. Stern, *Z. Elektrochem.*, 1924, **30**, 508-516.

[53] T. Cosgrove, *Colloid Science: Principles, Methods and Applications*, Wiley-Blackwell, 2010.

[54] A. Stone, *The theory of intermolecular forces*, Oxford University Press, 2013.

[55] D. J. Griffiths, *Introduction to electrodynamics*, Prentice-Hall, 1999.

[56] F. London, *Transactions of the Faraday Society*, 1937, **33**, 8b.

[57] H. Hamaker, *Physica*, 1937, **4**, 10581072.

[58] M. W. Cole, D. Velegol, H.-Y. Kim and A. A. Lucas, *Molecular Simulation*, 2009, **35**, 849866.

[59] Y. Liang, N. Hilal, P. Langston, V. Starov, *Advances in Colloid and Interface Science*, 2007, **134135**, 151166.

[60] J. N. Israelachvili and R. M. Pashley, *J Colloid Interface Sci*, 1984, **98**, 50014.

[61] P. M. Claesson and H. K. Christenson, *J Phys Chem*, 1988, **92**, 5-1650.

[62] Y. I. Rabinovich and B. V. Derjaguin, *Colloids Surf.*, 1988, **30**, 51-243.

[63] A. R. Abate and D. J. Durian, *Phys. Rev. Lett.*, 2008, **101**, 245701.

[64] J. Hutchinson, *Prog. Polym. Sci.*, 1995, **20**, 703.

[65] C. A. Angell, *Science*, 1995, **267**, 35-1924.

[66] A. J. Liu and S. R. Nagel, *Nature*, 1998, **396**, 21.

[67] V. Trappe, V. Prasad, L. Cipelletti, P. Segre and D. Weitz, *Nature*, 2001, **411**, 772775.

[68] D. Weitz and M. Oliveria, *Phys. Rev. Lett.*, 1984, **52**, 1433.

[69] C. S. O'Hern, L. E. Silbert, A. J. Liu and S. R. Nagel, *Phys. Rev. E*, 2003, **68**, 011306.

[70] L. E. Silbert, A. J. Liu and S. R. Nagel, *Phys. Rev. E*, 2006, **73**, 041304.

[71] C. A. Angell, K. L. Ngai, G. B. McKenna, P. F. McMillan and S. W. Martin, *J. Appl. Phys.*, 2000, **88**, 31133157.

[72] Z. Zhang, N. Xu, D. T. N. Chen, P. Yunker, A. M. Alsayed, K. B. Aptowicz, P. Habdas, A. J. Liu, S. R. Nagel and A. G. Yodh, *Nature*, 2009, **459**, 230.

[73] P. Pusey and R. Tough, *in Dynamic light scattering*, Springer, 1985, 85179.

[74] E. R. Weeks and D. Weitz, *Chemical physics*, 2002, **284** 361367.

[75] D. Saha, Y. M. Joshi and R. Bandyopadhyay, *Soft Matter*, 2014, **10**, 32923300.

[76] P. N. Pusey and W. van Megen, *Phys. Rev. Lett.*, 1987, **59**, 20832086.

[77] J. D. Bernal, *Proceedings of the Royal Society of London. Series A, Mathematical and Physical Sciences*, 1964, 299322.

[78] P. Pusey, E. Zaccarelli, C. Valeriani, E. Sanz, W. C. K. Poon and M. E. Cates, *Philosophical Transactions of the Royal Society of London A: Mathematical, Physical and Engineering Sciences*, 2009, **367**, 49935011.

[79] T. T. M. Torquato S and P. G. Debenedetti *Phys. Rev. Lett.*, 2000, **84**, 20642067.

[80] M. Fasolo and P. Sollich, *Phys. Rev. Lett.*, 2003, **91**, 068301.

[81] J. Hernández-Guzmán and E. R. Weeks, *Proceedings of the National Academy of Sciences*, 2009, **106**, 1519815202.

[82] A.-P. Hynninen and M. Dijkstra, *Phys. Rev. E*, 2003, **68**, 021407.

[83] B. Sierra-Martin and A. Fernandez-Nieves, *Soft Matter*, 2012, **8**, 4141.

[84] W.-H. Shih, W. Y. Shih, S.-I. Kim, J. Liu and I. A. Aksay, *Physical Review A*, 1990, **42**, 47724779.

[85] Y. Zhao, Y. Cao, Y. Yang and C. Wu, *Macromolecules*, 2003, **36**, 855-859.

[86] S. Ali and R. Bandyopadhyay, *Soft Matter*, 2016, **12**, 414.

[87] Z. Cheng, J. Zhu, P. M. Chaikin, S. E. Phan and W. B. Russel, *Phys. Rev. E*, 2002, **65**, 041405.

[88] S. E. Phan, W. B. Russel, Z. Cheng, J. Zhu, P. M. Chaikin, J. H. Dunsmuir and R. H. Ottewill, *Phys. Rev. E*, 1996, **54**, 45-6633.

[89] P. Pusey, P. Segre, O. Behrend, S. Meeker and W. Poon, *Physica A*, 1997, **235**, 1-8.

[90] J. Mewis, W. J. Frith, T. A. Strivens and W. B. Russel, *AIChE J.*, 1989, **35**, 22-415.

[91] L. Marshall and C. F. Zukoski, *J. Phys. Chem.*, 1990, **94**, 71-1164.

[92] A. K. Doolittle, *J. App. Phys.*, 1951, **22**, 5-1471.

[93] M. D. Ediger, *Annu. Rev. Phys. Chem.*, 2000, **51**, 99-128.

[94] H. Vogel, *Phys. Zeit*, 1921, **22**, 645-646.

[95] G. S. Fulcher, *J. Am. Ceram. Soc.*, 1925, **8**, 339-355.

[96] G. Tammann, *J. Soc. Glass Technol.*, 1925, **9**, 166-185.

[97] J. Rault, *J. Non-crystalline Solids*, 2000, **271**, 177-217.

[98] C. A. Angell, *J. Non-Crystalline Solids*, 1991, **131**, 13.

[99] V. N. Novikov and A. P. Sokolov, *Nature*, 2004, **431**, 961-963.

[100] S. Sengupta, F. Vasconcelos, F. A ouard and S. Sastry, *J. Chem. Phys.*, 2011, **135**, 194503.

[101] R. Kurita and E. R. Weeks, *Phys. Rev. E*, 2010, **82**, 041402.

[102] G. Brambilla, D. El Masri, M. Pierno, L. Berthier, and L. Cipelletti, *Phys. Rev. Lett.*, 2009, **102**, 085703.

[103] H. Sillescu, *J. Non-Cryst. Solids*, 1999, **243**, 81-108.

[104] R. Richert, *J. Phys.: Condens. Matter*, 2002, **14**, R703-R738.

[105] G. Adam and J. H. Gibbs, *J. Chem. Phys.*, 1965, **43**, 46-139.

[106] J. Hernández-Guzmán and E. R. Weeks, *Proc. Natl Acad. Sci. USA*, 2009, **106**, 202-15198.

[107] E. R. Weeks and D. A. Weitz, *Phys. Rev. Lett.*, 2002, **89**, 095704.

[108] A. H. Marcus, J. Schofield and S. A. Rice, *Phys. Rev. E*, 1999, **60**, 36-5725.

[109] W. K. Kegel and A. van Blaaderen, *Science*, 2000, **287**, 3-290.

[110] L. J. Kaufman and D. A. Weitz, *J. Chem. Phys.*, 2006, **125**, 074716.

[111] B. J. Berne, J. P. Boon and S. A. Rice, *J. Chem. Phys.*, 1966, **45**, 96-1086.

[112] K. S. Schweizer and E. J. Saltzman, *J. Chem. Phys.*, 2003, **119**, 96-1181.

[113] E. R. Weeks and D. A. Weitz, *Chem. Phys.*, 2002, **284**, 361-7.

[114] E. R. Weeks, J. C. Crocker and D. A. Weitz, *J. Phys.: Condens. Matter*, 2007, **19**, 205131.

[115] B. Doliwa and A. Heuer, *Phys. Rev. E*, 2000, **61**, 908-6898.

[116] L. Berthier, *Phys. Rev. E*, 2004, **69**, 020201.

[117] C. Donati, S. C. Glotzer, P. H. Poole, W. Kob and S. J. Plimpton, *Phys. Rev. E*, 1999, **60**, 19-3107.

[118] S. C. Glotzer, V. N. Novikov and T. B. Schrøder, *J. Chem. Phys.*, 2000, **112**, 12-509.

[119] R. E. Courtland and E. R. Weeks, *J. Phys.: Condens. Matter*, 2003, **15**, 359S365.

[120] L. Cipelletti, H. Bissig, V. Trappe, P. Ballesta and S. Mazoyer, *J. Phys.: Condens. Matter*, 2003, **15**, 62-S257.

[121] L. Berthier, G. Biroli, J. P. Bouchaud, W. Kob, K. Miyazaki and D. R. Reichman *J. Chem. Phys.*, 2007, **126**, 184504.

[122] L. Berthier, D. Chandler and J. P. Garrahan *Europhys. Lett.*, 2005, **69**, 6-320.

[123] T. Narumi, S. V. Franklin, K. W. Desmond, M. Tokuyama and E. R. Weeks *Soft Matter*, 2011, **7**, 82-1472.

[124] P. Ballesta, A. Duri and L. Cipelletti *Nature Phys.*, 2008, **4**, 4-550.

[125] P. Voudouris, B. V. Zanden, D. Florea, Z. Fahimi and H. Wyss, Shear thinning in soft particle suspensions, *American Physical Society Meeting*, Boston, Massachusetts, February 27-March 2, 2012.

[126] G. Romeo, A. Fernandez-Nieves, H. M. Wyss, D. Acierno and D. A. Weitz, *Adv. Mater.*, 2010, **22**, 3441.

[127] J. R. Stokes, Rheology of Industrially Relevant Microgels, 2011. *In:* A. Fernandez-Neives, H. Wyss, J. Mattson and D. A. Weitz (eds.) *Microgel Suspensions Fundamentals and Applications* Weinheim: Wiley-VCH Verlag.

[128] M. S. Wolfe and C. Scopazzi, *J. Colloid and Interface Sci.*, 1989, **133(1)**, 265-277.

[129] G. K. Batchelor and J. T. Green, *J . Fluid Mech.*, 1972, **56**, 375.

[130] G. K. Batchelor, *J . Fluid Mech.*, 1977, **83**, 97-117.

[131] C. I. Mendoza and I. Santamaria-Holek, *Journal of Chem. Phys.*, 2009, **130(4)**, 044904.

[132] J. Mewis and N. J. Wagner, Colloidal Suspension Rheology, London, Cambridge university press, 2011.

[133] S. H. Maron and P. E. Pierce, Colloidal Suspension Rheology, London, Cambridge university press, *Journal of Colloid Science*, 1956, **11**, 80-95.

[134] D. Quemada, Colloidal Suspension Rheology, London, Cambridge university press, *Journal of Colloid Science*, 1956, **11**, 80-95.

2

Materials and Methods

2.1 Introduction

This chapter discusses the synthesis methods used to prepare the colloidal suspensions studied in this thesis and the experimental techniques employed to study them. Colloidal particles with tunable size, size polydispersities, stiffness and activity are synthesized in order to study the effects of these parameters on the kinetically arrested state of colloidal suspensions. It is possible to tune the size, size polydispersity and stiffness of thermoresponsive poly(*N*-isopropylacrylamide) PNIPAM colloidal particles using one-pot and semi-batch methods. Furthermore, it is convenient to tune the activity or self-propulsion of chemically active Janus particles by varying the strength of the hydrogen peroxide solution. Dynamic light scattering is used to study the thermoresponsive behaviour of PNIPAM particles in aqueous suspensions. The rheological characterization of aqueous PNIPAM suspensions is performed using a commercially available rheometer. Scanning electron microscopy (SEM) is used to characterize the particle size and size distribution and to visualize these particles in their dried state.

The zeta potential of these particles in aqueous suspensions is estimated by using ultrasound attenuation spectroscopy. Confocal microscopy is used to study the dynamical and structural behaviour of aqueous PNIPAM colloidal suspensions in their dynamically arrested state.

2.2 Synthesis methods

2.2.1 Synthesis of PNIPAM colloidal particles

One-pot Method

In the one-pot method, the reaction ingredients are allowed to react together inside a reaction vessel. This method produces PNIPAM particles of sub-micron sizes with heterogeneously crosslinked polymer networks inside the particles [1]. The faster polymerization reaction of the crosslinker *N*, *N′*-methylenebisacrylamide (MBA), when compared to the monomer *N*-isopropylacrylamide (NIPAM), produces inhomogeneously cross-linked PNIPAM particles with densely crosslinked cores and loosely crosslinked shells [2].

All the chemicals are purchased from Sigma-Aldrich and are used as received without any further purification. In a typical experiment, 7.0 g monomer *N*-isopropylacrylamide (NIPAM) ($\geq$ 99%), 0.7 g crosslinker *N,N'*-methylenebisacrylamide (MBA) ($\geq$ 99.5%) and 0.03 g sodium dodecyl sulfate (SDS) are dissolved in 470 mL of Milli-Q water (Millipore Corp.) in a three-necked round-bottomed (RB) flask fitted with a reflux condenser, a temperature sensor and a N_2 inlet/outlet. The RB flask is placed on a magnetic stirrer (Heidolph MR Hei-Tec) with heating. The solution is stirred at 600 rpm and purged with N_2 gas for 30 min to remove oxygen dissolved in water. The temperature of the heat bath is raised to 70°C. The free radical polymerization reaction is initiated by the addition of 0.28 g of potassium persulfate (KPS) (99.99%) dissolved in 30 mL of Milli-Q water in the preheated bath at 70°C. The reaction is allowed to

Water (mL)	NIPAM (g)	MBA (g)	SDS (g)	KPS (g)
500	7	0.7	0.15	0.28
500	7	0.7	0.03	0.28
500	7	0.7	0.005	0.28
500	7	0.7	0.0025	0.28
500	7	2.1	0.03	0.28
500	7	1.4	0.03	0.28
500	7	0.7	0.03	0.28
500	7	0.035	0.03	0.28
500	7	0.007	0.03	0.28
500	7	0.0007	0.03	0.28

Table 2.1: Summary of synthesis conditions for preparing PNIPAM particles of various sizes and stiffnesses in the one-pot method. The particles are synthesized at 70°C by varying the SDS and MBA concentrations.

proceed for 4 hours with a constant stirring speed using a magnetic stirrer. After 4 hours, the reaction is stopped and the colloidal suspension is cooled down rapidly in an ice bath.

In this method, concentration of SDS and MBA are both varied to synthesize PNIPAM colloidal particles of different sizes and stiffnesses. The summary of the latex recipes is shown in table 2.1.

Semi-batch Method

In the semi-batch method, out of the total volume of the reaction solution, half of the solution is allowed to react inside the reaction vessel, while the remaining half of the solution is added externally. The continuous addition of monomer and crosslinker into the reaction vessel in this method produces homogeneously crosslinked micrometer sized particles [3, 4].

7.0 g of NIPAM, 0.46 g of MBA and 34.4 mg of 2-aminoethylmethacylate hydrochloride (AEMA) are dissolved in 200 mL of water in a three-necked round bottomed (RB) flask fitted with a reflux condenser, a temperature sensor and a N_2 inlet/outlet. The three-necked RB flask is placed on a magnetic stirrer (Heidolph MR Hei-Tec) with heating. The solution is stirred at 600 rpm for 20 min and also purged

Water (mL)	NIPAM (g)	MBA (g)	AEMA (mg)	APS (mg)	Flow rate
320	7	0.46	34.4	41.6	1.5 mL/min
320	7	0.46	34.4	41.6	1 mL/min
320	7	0.46	34.4	41.6	0.7 mL/min
320	7	0.46	34.4	41.6	0.5 mL/min

Table 2.2: Summary of synthesis conditions for preparing PNIPAM particles of various sizes in the semi-batch method. The particles are synthesized at 80°C by varying the flow rates of the reaction ingredients (aqueous solutions of NIPAM, MBA and AEMA).

with N_2 gas for 20 min. 180 mL of this solution is taken out in a syringe and 120 mL of water is added to the 20 mL solution remaining in the flask. The temperature of the heat bath is raised to 80°C and the bath is purged with N_2 gas for 20 min. The free radical precipitation reaction is initiated by the addition of 41.6 mg ammonium persulfate (APS) dissolved in 8 mL of water. Primary nucleation sites start to form after about 5 min, following which the solution present in the syringe is fed into the reaction vessel at a constant flow rate using a syringe pump (Chemyx Inc.). The reaction is stopped 5 min after all the ingredients are added. The latices are cooled down rapidly in an ice bath.

In this method, PNIPAM colloidal particles of different sizes are synthesized by varying the flow rates of the reaction ingredients into the RB flask. The preparation of the latex recipes is summarized in table 2.2.

Preparation of functionalized fluorescein

0.5g of fluorescein is added to 13.33 mL of dry tetrahydrofuran (THF) in a 100 mL round bottom flask fitted with a N_2 inlet/outlet. 4.67 ml of triethylamine (TEA) is added to the above solution while continuously stirring and purging the solution with N_2 gas. Under these conditions, TEA forms an acid hydrogen bonding with fluorescein dye and produces triethylammonium salts [5]. Next, 0.33 ml of acryloyl chloride is added while keeping the solution in an ice bath. The reaction is allowed to proceed overnight. The mixture is filtered with paper filters to remove the triethylammonium chloride salt produced in the reaction. The filtered mixture is kept for desiccation for

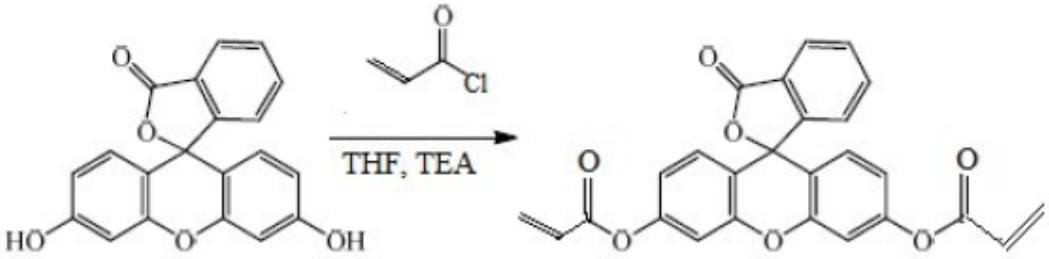

Figure 2.1: Synthetic scheme for functionalizing the fluorescein. The reactant fluorescein is functionalized in the presence of tetrahydrofuran (THF), triethylamine (TEA) and acryloyl chloride.

2 − 3 hours and pumped with nitrogen gas for about 5 min for complete removal of moisture from the mixture. Finally, the fluorescent crosslinker formed in this reaction is dried under a reduced pressure to retrieve the orange product. The final product is characterized by infrared (IR) spectroscopy. Figure 2.1 shows the synthetic scheme for functionalizing the fluorescein dye.

Synthesis of fluorescent PNIPAM particles

Fluorescent PNIPAM particles are prepared by incorporating functionalized fluorescein dye as a crosslinker in the polymer network in a semi-batch method. In a typical experiment, 2.0 g NIPAM (≥ 99%), 0.05 g MBA (≥ 99.5%), 8.3 mg of AEMA and 0.18 g of functionalized fluorescein are dissolved in 50 mL of Milli-Q water (Millipore Corp.) in a three-necked round-bottomed (RB) flask fitted with a reflux condenser, a temperature sensor and a N_2 inlet/outlet. The three-necked RB flask is placed inside a heat bath in contact with the hot plate of the magnetic stirrer (Heidolph MR Hei-Tec). The solution is stirred at 600 rpm for 20 min and also purged with N_2 gas for 20 min. 30 mL of this solution is taken out in a syringe and 10 mL of water is added to the remaining 20 mL of solution present in the flask. The temperature of the heat bath is

raised to 80°C and the bath is purged with N_2 gas for 20 min. The free radical precipitation polymerization reaction is initiated by the addition of 11.4 mg ammonium persulfate (APS) dissolved in 2 mL of water. Primary nucleation sites start to form after about 5 min, following which the solution present in the syringe is fed into the reaction vessel at a constant flow rate using a syringe pump (Chemyx Inc.). The reaction is stopped 5 min after all the ingredients are added. The latices are cooled down rapidly in an ice bath.

2.2.2 Synthesis of chemically active Janus particles

Flash red colored fluorescent polystyrene (PS) microspheres with a mean diameter 2.07 μm and standard deviation 0.15 μm suspended in aqueous medium are purchased from Bangs laboratories Inc. and are used as the stock suspension for the synthesis of Janus particles. The stock suspension contains 1 wt% PS microspheres and is diluted further with a 1 : 1 v/v of ethanol:Milli-Q water (resistivity 18.2 MΩ cm) mixture to prepare an 80% v/v of stock suspension. The diluted suspension is used to produce a monolayer of PS microspheres over a glass microscope slide. A cleaning procedure is followed for the glass microscope slides to remove dust particles, metals and organic contaminants. The glass slides are ultrasonicated in acetone, ethanol and Milli-Q water respectively for 15 min. They are immersed in piranha solution (mixture of 3 : 1 sulfuric acid and hydrogen peroxide) for 1 hour and rinsed with Milli-Q water. Before the deposition of PS microspheres, the glass microscope slides are dried in a hot air oven. A dense monolayer of PS microspheres over glass microscope slides is prepared by the spin coating method using an EZspin-A1 Apex Instruments spin coater. A dense monolayer of PS microspheres is obtained, when the glass substrate is rotated at a speed of 1000 rpm for 40 s with an acceleration time of 5 s. The SEM image shown in figure 2.2(a) confirms the formation of a dense monolayer of PS microspheres over a glass microscope slide. A thin layer of platinum of 5 nm thickness is deposited on one hemisphere of the PS microsphere by evaporating the platinum onto the PS coated slides for 50 s at 20 mA current using Quorum Q150R S sputter coater. The energy-dispersive

X-ray spectroscopy (EDAX) profile in figure 2.2(b) confirms the presence of 8.48 wt% of platinum on the PS microspheres. The half-platinum-coated microspheres are detached from the glass substrates using a 200 μm thick sheet of polytetrafluoroethylene (Goodfellow) which acts as a blade. The detached microspheres are redispersed in 5 mL of Milli-Q water of resistivity 18.2 MΩ cm. These PS microspheres with platinum coating on one hemisphere are self-propelled in the presence of hydrogen peroxide solution due to platinum induced catalytic decomposition of hydrogen peroxide into water and oxygen.

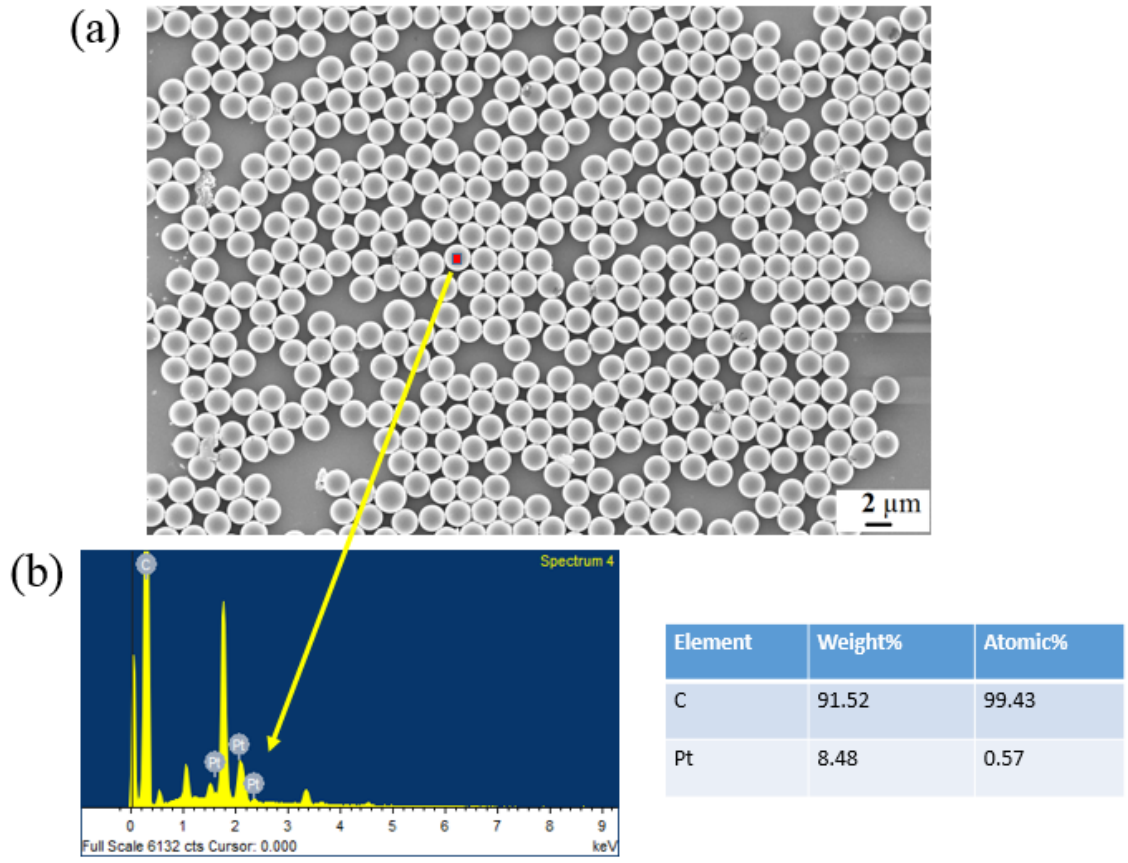

Element	Weight%	Atomic%
C	91.52	99.43
Pt	8.48	0.57

Figure 2.2: (a) SEM image of platinum coated polystyrene microspheres of mean diameter 2.07 μm with a standard deviation 0.15 μm quoted by the manufacturer (Bangs Laboratories Inc.). (b) Energy-dispersive X-ray spectroscopy (EDAX) profile of platinum coated PS microspheres. The table in this figure shows the wt% of platinum (Pt) present on the PS microspheres.

2.3 Experimental techniques

2.3.1 Dynamic Light Scattering

Dynamic light scattering (DLS) also known as photon correlation spectroscopy is an efficient technique used to determine the size and size distribution profile of colloidal particles in suspension. This technique is also employed to study the relaxation dynamics of colloidal suspensions.

Colloidal particles in a very dilute suspension are affected by thermal fluctuations and exhibit Brownian motion due to random collisions with the molecules of the suspension medium. Light is scattered by the colloidal particle due to the refractive index difference between the particle and suspension medium. The light is scattered in all directions when the size of the particle is less than the wavelength of the light. The intensity of the scattered light depends on the scattering angle and fluctuates due to the thermal motion of the scatterers. The scattering volume is defined as the volume of intersection between the incident and scattered beams [6]. The shape and size (hydrodynamic diameter) of the colloidal particle is measured from the angular dependence of the intensity fluctuations of the scattered light. A brief theory is given below for measuring the size of monodisperse spherical scatterers diffusing in a dilute suspension.

When a monochromatic plane wave of frequency ω_0 polarised perpendicular to the scattering plane is incident on a sample of scattering volume V containing N identical scatterers, the light scattered by the jth scatterer at an angle θ and at a distance R_0 is given by [7, 8]:

$$E_j = A_j(t)\exp(i\phi)\exp(-i\omega_0 t) \tag{2.1}$$

where A_j is the amplitude of the scattered field E_j. For a scatterer situated at the origin, the phase $\phi = 0$. However, the phase for the jth scatterer with a position vector

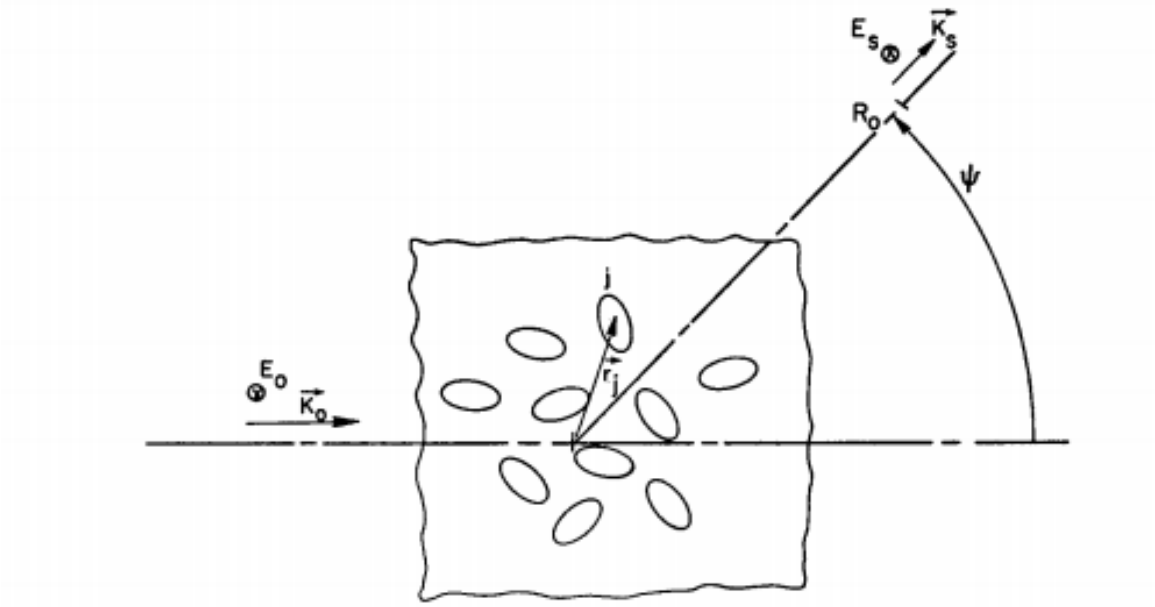

Figure 2.3: Schematic diagram of the geometry of a scattering system. This figure is adapted from [7]

r_j with respect to the origin is:

$$\phi_j = (\vec{K_0} - \vec{K_s}) \cdot \vec{r_j} = \vec{q} \cdot \vec{r_j} \tag{2.2}$$

where $\vec{K_0}$ and $\vec{K_s}$ are the incident and scattered wave vectors respectively. For quasi-elastic light scattering, $|\vec{K_0}| \approx |\vec{K_s}|$ and $|\vec{q}| = 2|\vec{K_0}| \sin(\theta/2) = \frac{4\pi n}{\lambda} \sin(\theta/2)$. Here, n and λ are the refractive index of the scatterer and wavelength of the laser light respectively [6, 9]. The total scattered field at a distance R_0 is given by:

$$E_s = \sum_{j=1}^{N} A_j(t) e^{i\vec{q}\cdot\vec{r_j}} e^{-i\omega_0 t} \tag{2.3}$$

The average scattered intensity at R_0 is given by $I_s = \langle |E_s|^2 \rangle$. The angular bracket $\langle\rangle$ represents an average over time. If the motion of the scatterers are independent and uncorrelated, all the cross terms in the expression of I_s in the time average vanish to

yield $I_s = \langle \sum_{j=1}^{N} |A_j|^2 \rangle = N\langle |A|^2 \rangle$. The electric field autocorrelation function $C(\tau) = \langle E_s^*(t) E_s(t+\tau) \rangle$ of a stationary random process is related with its intensity spectrum $I(\omega)$ by the relation [10]:

$$I(\omega) = \frac{1}{2\pi} \int_{-\infty}^{\infty} C(\tau) e^{i\omega\tau} d\tau \tag{2.4}$$

Here, E_s^* is the complex conjugate of E_s. Substituting the values of E_s and E_s^* in the expression for $C(\tau)$:

$$C(\tau) = N e^{-i\omega_0\tau} \langle A^*(t) A(t+\tau) \rangle \left\langle e^{-i\vec{q}\cdot\vec{r}(t)} e^{i\vec{q}\cdot\vec{r}(t+\tau)} \right\rangle \tag{2.5}$$

The above relation is obtained by assuming the positions and orientations of all the scatterers are independent of each other. Here all the N scatterers are identical and have the same autocorrelation function. Substituting the above value of $C(\tau)$ in equation 2.4, for identical and statistically independent scatterers, we get:

$$I(\omega) = \frac{N}{2\pi} \int_{-\infty}^{\infty} e^{i(\omega-\omega_0)\tau} [C_A(\tau)][C_\phi(\tau)] d\tau \tag{2.6}$$

For identical spherical scatterers undergoing translational diffusion, the scattering amplitude $A(t)$ is constant. Therefore, $[C_A(\tau)] = 1$ and the phase autocorrelation function $[C_\phi(\tau)] = e^{-Dq^2\tau}$ [7], where D is the translational diffusion coefficient and is related to the hydrodynamic radius r_h of the scatterer by the Stokes-Einstein relation [11],

$$D = \frac{k_B T}{6\pi\eta r_h} \tag{2.7}$$

Here k_B is the Boltzmann constant, η is the viscosity of the suspension medium at temperature T.

Depending on the optical mixing protocol of the spectrum of scattered light, the

DLS measurement techniques are divided into homodyne and heterodyne measurements. In the homodyne measurement, the scattered spectrum is mixed with itself. However, in heterodyne measurements, a part of the incident beam is mixed with the scattered beam. The homodyne measurement technique is used for all the DLS experiments reported in this thesis. In this method, the output of the detector is either analyzed by an autocorrelator to generate the autocorrelation function or is sent to a spectrum analyzer. The instantaneous intensity $I(t)$ of the spatially coherent optical field is related to the electric field $E(t)$ by the relation: $I(t) = E^*(t)E(t)$. The second-order intensity autocorrelation function $g^{(2)}(\tau)$ can therefore be related to the first-order electric field autocorrelation function $g^{(1)}(\tau)$ by the Siegert relation [12]:

$$g^{(2)}(\tau) = 1 + A|g^{(1)}(\tau)|^2 \tag{2.8}$$

where $g^{(1)}(\tau) = \langle E^*(t)E(t+\tau)\rangle \,/\, \langle E^*(t)E(t)\rangle$, $g^{(2)}(\tau) = \langle E^*(t)E(t)E^*(t+\tau)E(t+\tau)\rangle \,/\, \langle E^*(t)E(t)\rangle^2$ and A is the coherence factor. For a dilute suspension of identical spherical scatterers undergoing translational diffusion, $g^{(1)}(\tau) \propto e^{-Dq^2\tau}$ and therefore $g^{(2)}(\tau) - 1 \propto e^{-2Dq^2\tau}$.

A basic DLS set up consists of a monochromatic and coherent source or laser, a bath containing a liquid whose refractive index matches with the wall of the sample cell, a very fast and efficient detector (photo multiplier tube (PMT) or avalanche photo diode (APD)) and a correlator. A schematic diagram and snapshot of a DLS setup is shown in figure 2.4. For the DLS experiments reported here, a 150 mW solid state laser ($NdYVO_4$, Coherent Inc., Spectra Physics Excelsior) with an emission wavelength of 532 nm is used as a light source. A bath containing a sample holder is filled with decalin, a refractive index matching liquid to avoid scattering from the wall of the sample cell. The temperature of the sample cell is maintained by a water circulation temperature controller (Polyscience Digital). A Brookhaven Instruments Corporation (BIC) BI-200SM spectrophotometer is used to measure the intensity of light scattered

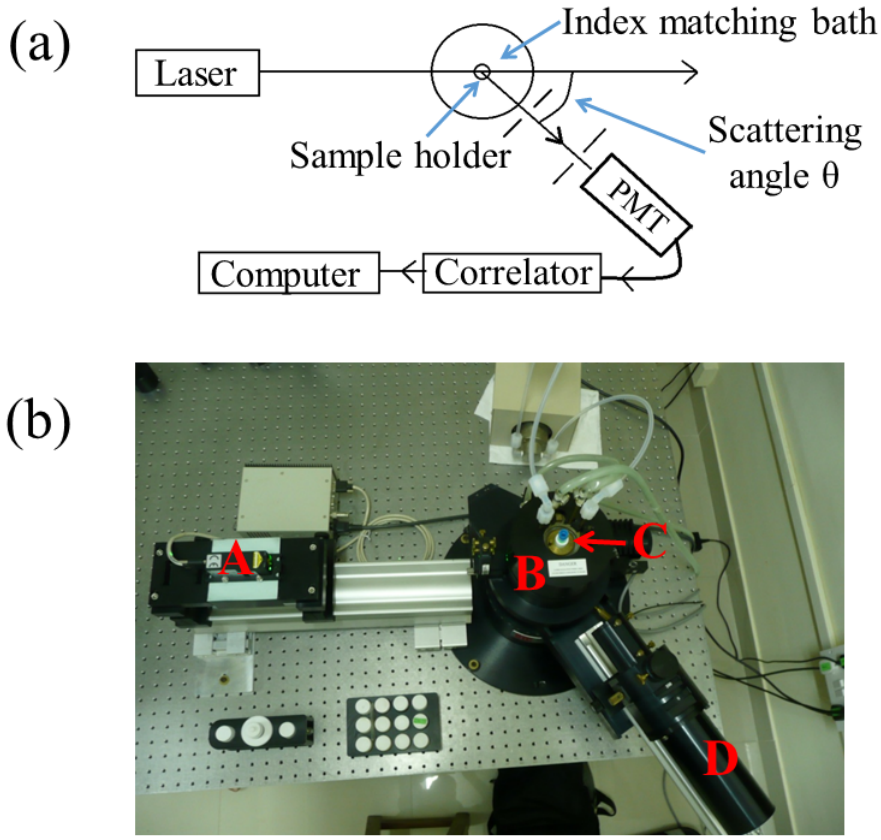

Figure 2.4: (a) A schematic diagram of a dynamic light scattering (DLS) setup. (b) Photo of BIC 200SM DLS setup with a laser (A), a bath (B) containing refractive index matching liquid and sample holder (C) and a photo multiplier tube (D).

from the sample at angles between 10° to 150°. The scattered photons generate secondary electrons inside the detector which set off voltage pulses in the PMT [13]. A Brookhaven BI-9000AT digital autocorrelator connected to the output of the detector is used to measure the intensity autocorrelation function of the light scattered from the sample. BI-9000AT is a high speed signal processor and operates in real time over 10 decades in delay time. It can also be used as a cross correlator in DLS measurements. The scattered photon pulses are registered in correlator channels, which are separated by logarithmically or linearly spaced delay times. The maximum number of channels used in the autocorrelator are 522 (240 channels for low speed, 256 channels for medium speed and 26 channels for high speed circuits) [13]. In the linearly spaced

correlator, the delay time is proportional to the sampling time. The last delay time is equal to the sampling time multiplied by the number of channels. In the BI-9000AT, four different sampling times are possible: 25 and 100 ns for the high speed circuits and two variable sampling times, one each for the medium and high speed circuits. The intensity autocorrelation function $g^{(2)}(\tau)$ is calculated by the autocorrelator using the following expression [13]:

$$g^{(2)}(\tau_j) = \lim_{N\to\infty} \frac{1}{N} \sum_{i=1}^{\infty} n_i n_{i-j} \qquad j = 1, 2, ...M \tag{2.9}$$

where N is the total number of samples, n_i and n_{i-j} are the number of pulses during the sampling time $\Delta\tau$ centered at some time t and $t - \tau_j$ respectively and M is the number of correlator channels [13].

The average number of pulses $< n >$ in a sampling time $\Delta\tau$ can be obtained from the average count rate <CR> by the relation $< n >$=<CR>$\Delta\tau$ [13]. The ability of the correlator to form the complete product while multiplying the pulses is limited by the number of bits allocated to a section of the circuit.

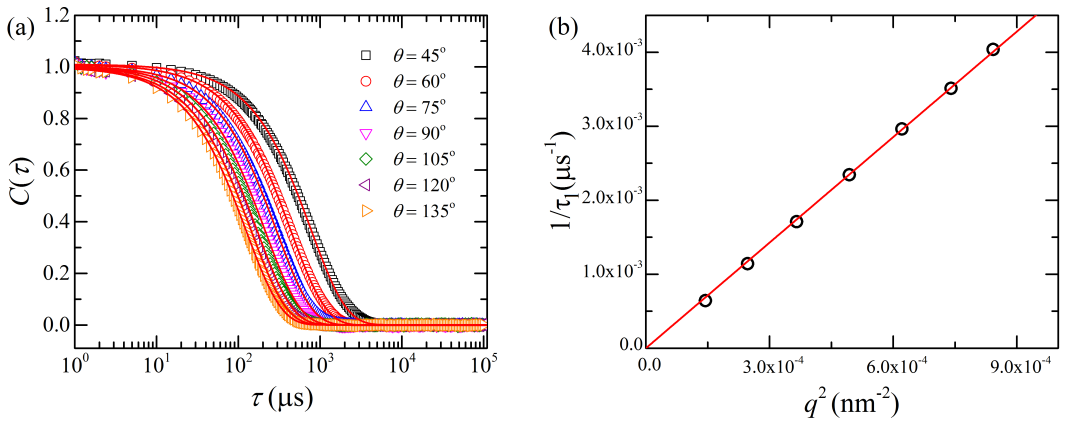

FIGURE 2.5: (a) The normalized intensity correlation function $C(\tau)$ *vs.* the delay time τ for scattering by 100 nm standard polystyrene (PS) particles in a dilute aqueous suspension at 25°C and at different scattering angles θ. The solid lines are fits to the equation: $C(\tau) = [\exp(-\tau/\tau_1)]^2$. (b) $1/\tau_1$ *vs.* q^2 plot showing diffusive behaviour of the PS particles. The translational diffusion coefficient D is extracted from the slope of the linear fit (solid line). Application of the Stokes-Einstein relation yields 102 ± 1 nm as the size of the PS particle.

Data analysis

The normalized intensity autocorrelation function $C(\tau) = g^{(2)}(\tau)-1$ of standard polystyrene (PS) particles in a very dilute suspension is plotted as a function of the delay time τ in figure 2.5(a) at several different scattering angles θ and at a temperature $T = 25°C$. The mean size of the PS particles is 100 nm with a polydispersity of 3.7% as quoted by the manufacturer (Bangs Laboratories Inc.). A very dilute PS suspension of volume fraction $\phi = 10^{-5}$ is prepared from the supplied stock suspension to ensure single scattering. The intensity autocorrelation function at a certain scattering angle θ is defined as $g^{(2)}(\tau) = \frac{<I(0)I(\tau)>}{<I(0)>^2} = 1 + A|g^{(1)}(\tau)|^2$ [6], where $I(\tau)$, $g^{(1)}(\tau)$ and A are the intensity at a delay time τ, the normalized electric field autocorrelation function and the coherence factor, respectively. The angular bracket <> represents an average over time. The intensity autocorrelation functions are acquired at seven different scattering angles (corresponding to seven different q). The decays of the normalized autocorrelation functions $C(\tau) = \frac{g^{(2)}(\tau)-1}{A}$ are fitted to exponential functions of the form $C(t) = \left[\exp(-\tau/\tau_1)\right]^2$ (solid line fits in figure 2.5(a)). Here τ_1 is the relaxation time of the PS particles. τ_1 values obtained from the fits to the $C(\tau)$ *vs.* τ_1 data at seven different scattering angle θ are plotted as $1/\tau_1$ *vs.* q^2 in figure 2.5(b). A straight line passing through the origin (solid line in figure 2.5(b)) indicates diffusive behaviour *i.e.* $1/\tau_1 = Dq^2$. Here D is the translational diffusion coefficient and is obtained from the slope of the $1/\tau_1$ *vs.* q^2 plot. The size of the polystyrene particles dispersed in aqueous medium ($\eta = 0.89$ mPa.s at 25°C) is calculated by using the Stokes-Einstein relation (equation 2.7). The estimated size of the PS particle is 102 ± 1 nm which matches fairly well with the size quoted by the manufacturer.

2.3.2 Rheological measurements

Rheology is the study of the flow and deformation of a material under applied stress or strain. Rheological measurements are used to characterize the mechanical properties of liquids, solids and viscoelastic materials. The rheological parameters of a material

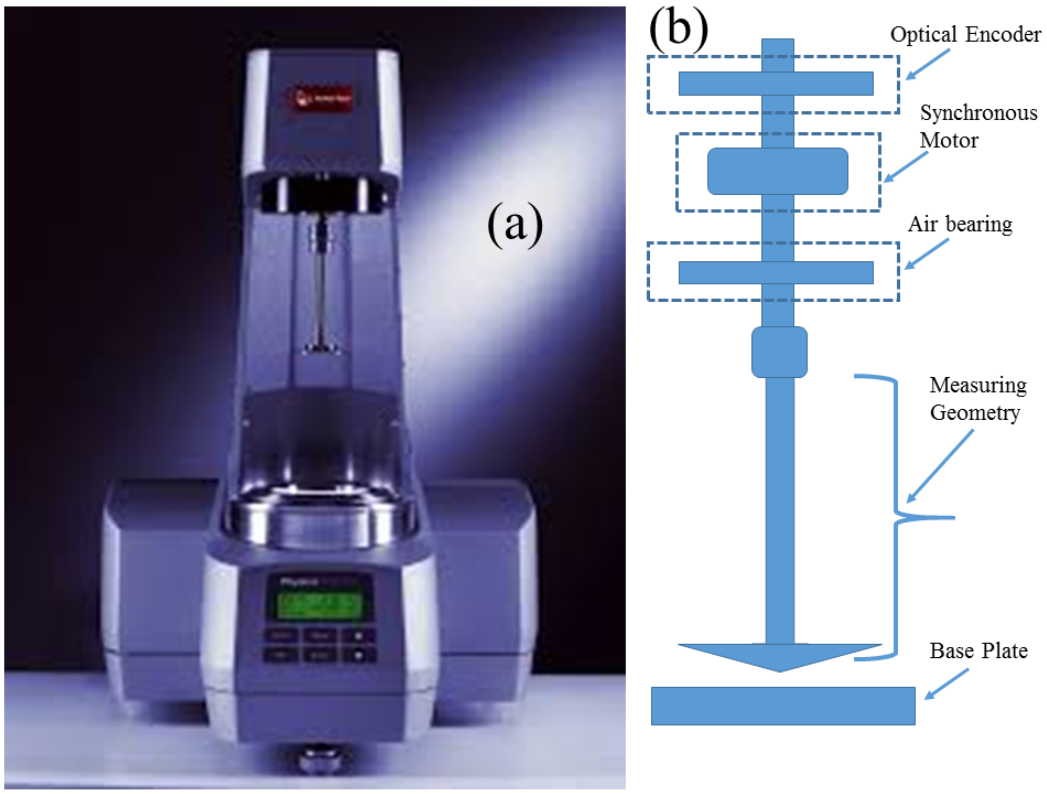

Figure 2.6: (a) The Anton Paar MCR 501 rheometer. This figure is adapted from [14]. (b) A schematic diagram of the main components of the Anton Paar MCR series rheometer.

can be measured using a rheometer. A rheometer can be operated either in stress or in strain controlled modes, depending upon the control parameters. In a stress controlled rheometer, a shear stress (constant or time dependent) is applied to a material and the resultant strain is measured. In a strain controlled rheometer, a shear strain (constant or time dependent) is applied and the resultant stress is measured. The rheological measurements reported in this thesis are performed using stress controlled modular compact Anton Paar MCR 501 (figure 2.6(a)) and MCR 702 rheometers. These instruments can also be used to control strain or shear rate through a feedback mechanism [14]. Figure 2.6(b) shows the main components of the Anton Paar MCR series rheometer. The key component of MCR series rheometers is the air-bearing-supported synchronous electrically commutated (EC) DC motor [14]. The rotor of the EC motor consists of permanent magnets. The magnets in the rotor and the stator coils attract

each other. As a result, a rotating flux of current in the coil windings produces a frictionless synchronous movement of the rotor. The instantaneous buildup of a magnetic field in the EC motor generates a fast response time for step strain tests [14]. Moreover, the existence of a linear relationship between the electromagnetic torque and the stator current is an advantage for precise torque and deflection angle control and measurements. The air bearing technology allows the friction free motion of the motor which is achieved by maintaining a high steady pressure in the head which supplies dust-free and moisture-free compressed air using a compressor [14]. This feature allows the user to achieve very low torque measurements down to a minimum of 0.5 nN.m with a resolution of 0.01 nN.m [14]. The high sensitivity normal force sensor integrated in the air bearing enables the measurement of normal forces during the transient and steady states. The normal force sensor detects the natural movement of the air bearing and precisely converts the extremely small deflections into normal forces in the range between 0.01 μN.m to 300 mN.m with a resolution of 0.01 nN.m [14].

The high resolution optical encoder is used to measure the strain. This enables the precise measurement and control of angular deflection with a resolution $< 1\ \mu$ rad. The rheological data reported in this thesis are acquired using Rheoplus software in MCR 501 rheometer and RheoCompass software in MCR 702 rheometer. For temperature control in the range between 0°C and 180°C, with a temperature stability of ±0.1°C, a Peltier unit is used. A water circulation unit (Viscotherm VT2) is used to control the temperature of the sample in the measuring geometry in the range between 5°C and 80°C with a temperature stability of ±0.1°C.

For various rheological tests, a measuring geometry is attached to the rotating rod of the rheometer and is automatically detected. The exact gap size for a geometry is maintained using the TruGap^{TM} technology which eliminates errors from thermal expansion and normal force. Depending on the nature of the sample and our experimental requirements, we have used different types of measuring geometries. These geometries are described below:

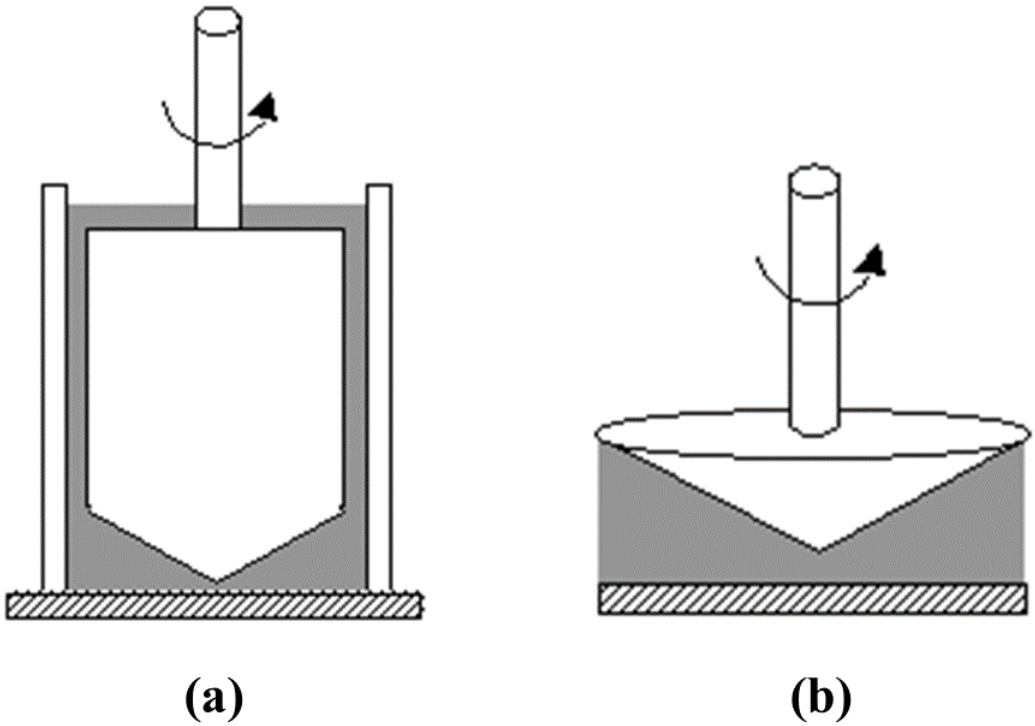

Figure 2.7: Schematic diagram of various rheometer geometries: (a) concentric cylinder and (b) cone and plate. The figure is adapted from https://ciks.cbt.nist.gov/~garbocz/SP946/node14.htm.

Concentric cylinder geometry

A concentric cylinder geometry is used for rheological measurements of samples of intermediate concentration or viscosity. The concentric cylinder geometry consists of a co-axially arranged cylindrical cup and a rotating cylindrical measuring head (figure 2.7(a)). The sample is kept in the annulus between the cylindrical surfaces. The concentric cylinder CC-17 geometry, used for our rheological measurements, has a gap of 0.71 mm, an effective length of 24.99 mm and requires a sample volume of 4.72 ml for each run. This geometry can measure shear stresses in the range between 771.345×10^{-6} Pa and 17740.935 Pa, shear strains above 1.23×10^{-5} and strain rates between 1.283×10^{-7} s^{-1} and 3.849×10^{3} s^{-1}.

Cone and plate geometry

The cone and plate geometry is used for rheological measurements of samples of high viscosity such as pastes, gels and concentrated suspensions. The cone and plate geometry consists of a rotating inverted cone placed over a fixed flat plate (figure 2.7(b)). The sample is placed in the gap between the cone and the plate. This geometry is used for suspensions of particles of sizes $\leq 1/10$th of the trucation height. In this geometry, a uniform shear rate is maintained in all the sections of the samples. The cone and plate CP-25 geometry, used for our rheological measurements, has a measuring gap $d = 0.048$ mm with cone radius $r_c = 12.49$ mm, cone angle $\alpha = 0.979°$. The truncation of cone in this geometry is 48 μm. This geometry requires a very small sample volume of 0.07 ml for each experiment.

Applications of the rheometer

The Anton Paar MCR 501 and 702 rheometers are used to perform different rheological measurements. These rheometers have two basic modes of operation viz. rotational and oscillatory.

Rotational experiments

In rotational experiments, a shear stress, strain or shear rate is applied to the sample along a certain direction to estimate its shear flow behaviour by measuring the shear strain, stress or viscosity. These experiments are useful for studying the shear thinning, shear thickening, shear banding, creep and stress relaxation behaviors of fluids, solids and viscoelastic materials. Flow curves and viscosity measurements are the only rotational experiments that we used in this thesis to measure the shear stress and viscosity of the PNIPAM suspensions. The flow curve is measured by controlling shear rate $\dot{\gamma}$ or stress σ and measuring the response in terms of σ or $\dot{\gamma}$ respectively. Flow curves are useful for estimating the sample viscosities. Figure 2.8(a) shows the flow curve (shear stress σ *vs.* shear rate $\dot{\gamma}$) and the corresponding viscosity plot (viscosity η *vs.* $\dot{\gamma}$)

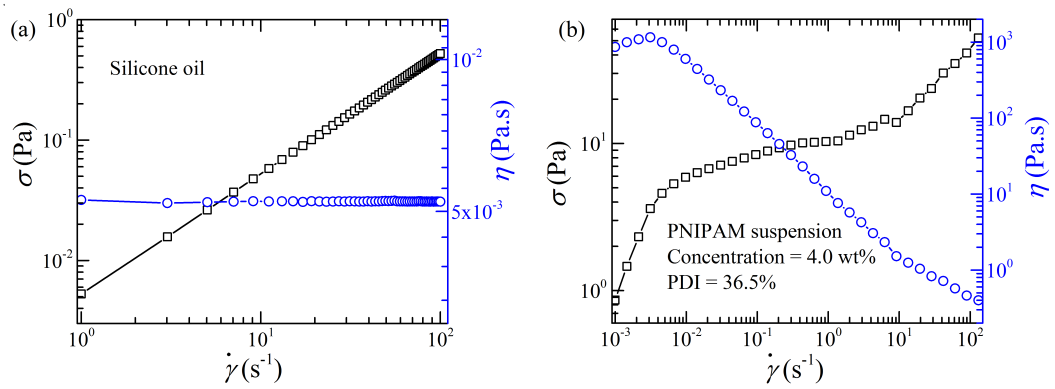

Figure 2.8: (a) Plot of shear stress σ (□) and the viscosity η (○) as a function of applied shear rate $\dot{\gamma}$ of silicone oil at a temperature 25°C. A double gap DG-26.7/Q1 geometry [14] is used for this measurement. Viscosity remains constant at 0.0052 Pa.s in this regime, confirming the Newtonian flow behavior of silicone oil. (b) Plot of shear stress σ (□) and the viscosity η (○) as a function of applied shear rate $\dot{\gamma}$ of PNIPAM suspension synthesized by the semi-batch method and characterized by PDI = 36.5% at a concentration of 4.0 wt% at 25°C. CC-17 geometry is used for this measurement. The viscosity decreases with shear rate, indicating the non-Newtonian nature of PNIPAM suspensions.

of silicone oil. The viscosity η of silicone oil is independent of shear rate $\dot{\gamma}$, thereby revealing its Newtonian liquid behaviour. Figure 2.8(b) shows the flow curve of a 4 wt% PNIPAM suspension at 25°C. The viscosity of PNIPAM suspension decreases with increasing shear rate, reflecting the shear thinning behavior of this suspension.

Oscillatory experiments

In an oscillatory rheological experiment, a sinusoidal perturbation (strain or stress) is applied to a material and the corresponding response (stress or strain) of the material is measured. For instance, if a sinusoidal strain γ of amplitude γ_0 and angular frequency ω is applied to a material:

$$\gamma(\omega) = \gamma_0 \sin(\omega t) \tag{2.10}$$

the corresponding stress response σ of the material at small strain amplitudes is given by [15]:

$$\sigma(\omega) = \sigma_0 \sin(\omega t + \delta) \tag{2.11}$$

Here, σ_0 and δ are respectively the shear stress amplitude and phase lag. The value of δ is zero for purely elastic material and 90° for purely viscous material. For a viscoelastic material, δ lies between zero and 90°.

A complex shear strain $\gamma^\star = \gamma_0 e^{i\omega t}$ is applied to the material and the corresponding stress response $\sigma^\star = \sigma_0 e^{i\omega t+\delta}$ is measured. The complex shear modulus $G^\star(\omega)$ of the material can be written as [15]:

$$G^\star(\omega) = \frac{\sigma^\star}{\gamma^\star} = \frac{\sigma_0}{\gamma_0} e^{i\delta} = |G^*|(\cos(\delta) + i\sin(\delta)) = G'(\omega) + iG''(\omega) \tag{2.12}$$

where $G'(\omega)$ and $G''(\omega)$ are the elastic and viscous moduli of the material respectively. The absolute value of the complex modulus can be calculated as $|G^*(\omega)| = [G'(\omega)^2 + G''(\omega)^2]^{1/2}$. The ratio of the viscous and elastic moduli is called the loss factor and is defined as $\tan(\delta) = G''(\omega)/G'(\omega)$ [15].

The oscillatory rheological measurements used for this thesis work are described below:

Strain amplitude sweep:

In amplitude sweep experiments, viscoelastic moduli (G' and G'') of a material are measured by varying the amplitude of the applied oscillatory strain at a constant ω. This experiment is usually performed to find the linear viscoelastic (LVE) regime of a material. Figure 2.9 shows the plot of an amplitude sweep test for a 25 wt% aqueous PNIPAM suspension which is in a soft solid phase at 15°C. The range of the amplitudes of the applied strain γ_0, where the viscoelastic moduli show constant values, is defined as linear viscoelastic (LVE) regime. In this plot, the linear regime is seen for $\gamma_0 \leq 7\%$. In this LVE regime $G' > G''$, which indicates the viscoelastic solid nature of the

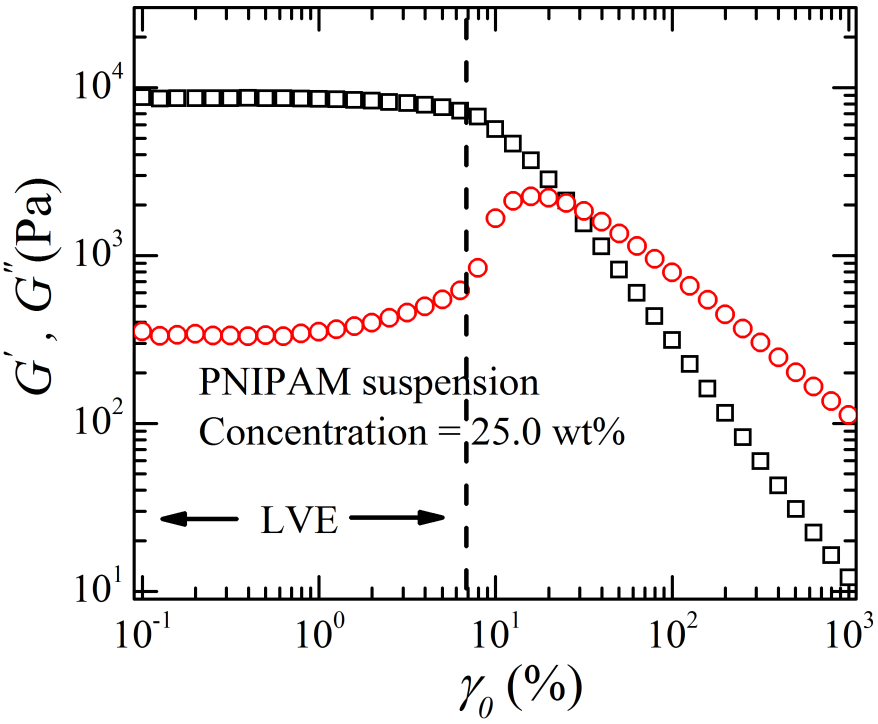

FIGURE 2.9: Elastic modulus G' (□) and viscous modulus G'' (○) *vs.* applied oscillatory strain amplitude (γ_0) at an angular frequency ω of 1 rad/s for a 25 wt% aqueous PNIPAM suspensions at 15°C. The range of the amplitudes of the applied strain γ_0 ($\gamma_0 \leq 7\%$) upto the dashed line), where the viscoelastic moduli (G', G'') show constant values, is the linear viscoelastic (LVE) regime and is marked with the arrow lines.

PNIPAM suspension. For γ_0 values above the LVE regime, G' decreases monotonically while G'' shows a peak before decreasing monotonically due to the break down of the sample's microstructures under high strains.

Frequency sweep:

In frequency sweep experiments, viscoelastic moduli of a material is measured by varying the angular frequency ω of the oscillatory strain while keeping the strain amplitude γ_0 at a constant value. These measurements are generally performed in the LVE regime of materials. Figure 2.10 shows the plots of G' and G'' as a function of ω for a 24 wt% aqueous PNIPAM suspensions at 25°C, where the amplitude of strain

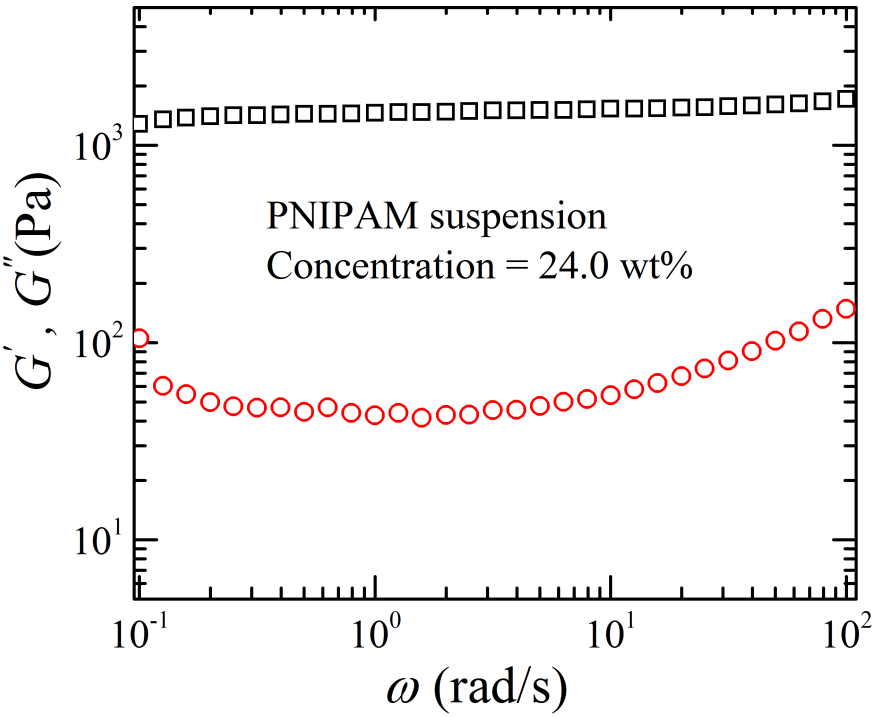

Figure 2.10: Elastic modulus G' (□) and viscous modulus G'' (○) *vs.* angular frequency (ω) at an applied strain amplitude γ_0 of 0.1% for a 24 wt% aqueous PNIPAM suspensions at 25°C.

γ_0 is kept constant at 0.1%. It is seen that G' is independent of the frequency of the applied strain, while G'' shows a weakly frequency dependent behavior. This suggests the presence of ultraslow glassy dynamics in this sample. In the entire frequency range, $G' > G''$, indicating the solid-like behaviour of this suspension under the experimental conditions.

Temperature sweep:

In temperature sweep experiments, the amplitude γ_0 and angular frequency ω of the applied oscillatory strain is kept constant, the temperature of the sample is varied at a certain rate and the corresponding G' and G'' are measured. These experiments are useful to study the mechanical behavior of the material as a function of temperature. Figure 2.11 shows the plots of G' and G'' as a function of temperature for a 24 wt%

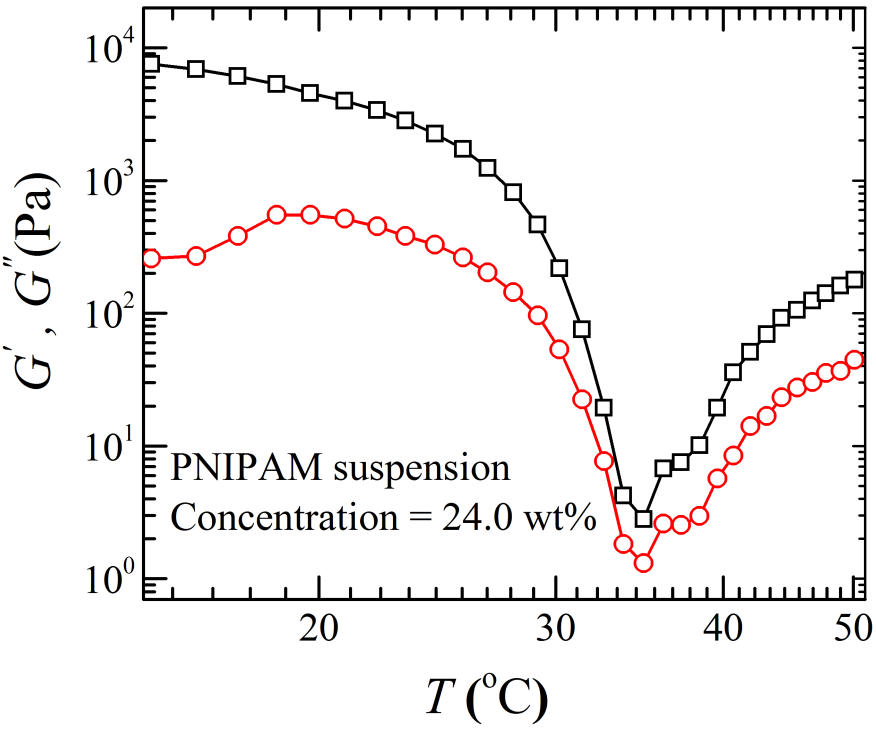

FIGURE 2.11: Elastic modulus G' (□) and viscous modulus G'' (○) is measured as function of temperature T of a 24 wt% aqueous PNIPAM suspensions at an angular frequency ω = 1.0 rad/s and at an applied strain amplitude γ_0 = 0.1%.

aqueous PNIPAM suspension, where the amplitude of strain γ_0 and angular frequency ω are kept constant at 0.1% and 1 rad/s respectively. From this plot, it is seen that the viscoelastic moduli G' and G'' show a non-monotonic change with the increase in temperature. This shows the typical behavior of a dense suspension of thermoresponsive PNIPAM microgel particles.

Medium amplitude oscillatory shear (MAOS) experiments:

Medium amplitude oscillatory shear (MAOS) tests are useful for studying the linear and nonlinear responses of a material. In these experiments, the viscoelastic moduli of a material at odd harmonics are measured by varying the strain amplitude γ_0, while keeping the angular frequency ω constant. Here, Anton Paar MCR 702 rheometer is

used for MAOS tests. Figures 2.12(a) and 2.12(b) respectively show the plots of the Fourier coefficients of G' and G'' at first and third harmonics as a function of γ_0 for a 20 wt% PNIPAM suspension of PDI = 11.6% measured at an angular frequency ω = 1.0 rad/s. In the LVE regime, the viscoelastic moduli at first harmonic G'_1 and G''_1 have finite values with $G'_1 > G''_1$, while the values of viscoelastic moduli at the third harmonic G'_3 and G''_3 are vanishingly small and positive with $G'_3 \approx G''_3$. With increasing γ_0, G'_3 and G''_3 exhibit finite values and pass through a maximum before decreasing rapidly. These trends are very sensitive to the applied angular frequency and volume fraction of the material [16]. The intrinsic nonlinear behavior of a material can be studied by extrapolating the values of Fourier coefficients of the viscoelastic moduli at the first and third harmonics to extremely small strain amplitudes ($\gamma_0 \to 0$) [16].

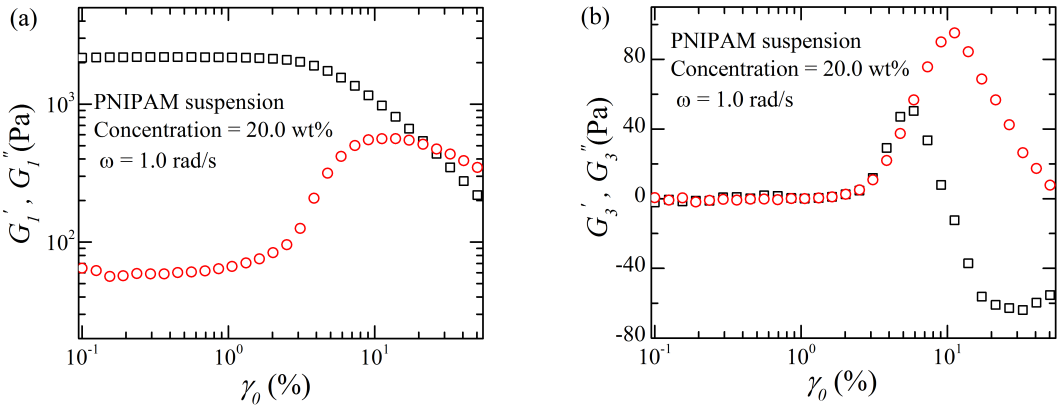

Figure 2.12: (a) Fourier coefficients of the elastic and viscous moduli at the first harmonic (G'_1 (□), G''_1 (○)) *vs.* strain amplitude γ_0 for a 20 wt% PNIPAM suspensions of PDI = 11.6% measured at an angular frequency ω = 1.0 rad/s at 25°C. (b) Fourier coefficients of the elastic and viscous moduli at the third harmonic (G'_3 (□), G''_3 (○)) vs. strain amplitude γ_0 for a 20 wt% PNIPAM suspensions of PDI = 11.6% measured at an angular frequency ω = 1.0 rad/s at 25°C.

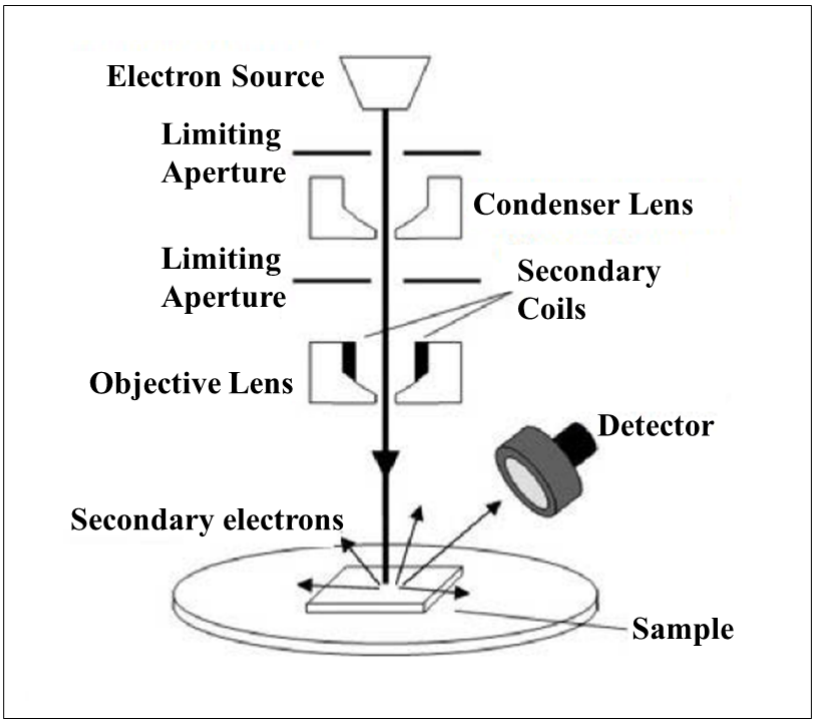

FIGURE 2.13: Schematic diagram of a scanning electron microscopy setup. This figure is adapted from [23].

2.3.3 SEM

Scanning electron microscopy (SEM) is used to produce images of the suspensions down to a few nanometers [17]. Over the last decades, this technique has been widely used in the field of soft matter to investigate the structures and measure the sizes of biological samples, polymer blends, hydrogels, colloidal suspensions and micellar solutions at nanometer or micrometer level [18–22]. In this technique, a dried sample deposited on a conducting plate such as an indium tin oxide (ITO) plate or a cryo-fractured sample coated with a thin metal layer is irradiated with a high power electron beam. The electron beam interacts with the atoms of the sample and the secondary electrons emitted or the back-scattered electrons from the sample are used to produce the surface images of the sample.

A field effect scanning electron microscope (ULTRA-PLUS FESEM) from Carl Zeiss is used to visualize our samples at the nanometer or micrometer level. Figure 2.13 shows a schematic diagram of the main components of the SEM setup. It consists

of an electron column, a scanning system, a detector, a vacuum system and a display unit [23]. The electron column consists of an electron gun and two or more electromagnetic lenses operating in vacuum. The electron gun generates free electrons. These are emitted when the applied energy is greater than the work function of the source material. The free electrons generated by the electron gun are accelerated to energies in the range 1-100 keV [23]. A set of electromagnetic lenses are used to control the path of the electron beam. Two types of electromagnetic lenses are used. The first lens system contains the scanning coils and is used to raster the beam onto the specimen. These lenses are also combined with the apertures in order to control the size of the beam. Next, a condenser lens is used to control the size of the electron beam (which defines resolution), while an objective lens is used to focus the electron beam onto the surface of the specimen [23]. Each surface point of the specimen that is struck by accelerated electrons emits various types of electrons such as backscattered electrons (BSE) and secondary electrons (SE). BSEs are in fact a part of the incident electrons which enters the specimen and reflects back after the elastic interaction between the electron beam and the specimen. On the other hand, SE are originated from the atoms of the specimen due to the inelastic interaction between the electron beam and the specimen. The BSE originates from the deeper regions of the sample, while SE originates from the surface regions [23]. The yield of SE increases with decreasing the angle between the incident beam and the specimen surface (figure 2.13) [24]. The SEs are distinguishable from the BSEs owing to their much lower energies of the order of a few electron volts [24]. BSE imaging is sensitive to the atomic number of the material. The higher the atomic number, the brighter the material appears in the image. The SE imaging provides detailed surface information of the material.

In this work, both secondary and backscattered electrons are used to obtain the images of microstructures of the samples. Secondary electrons collected by the Everhart-Thornley detector are placed at an angle near the sample, while backscattered electrons collected by the solid state detectors are placed above the sample [23]. The output signal of electron detectors is amplified and displayed on the screen of a synchronously

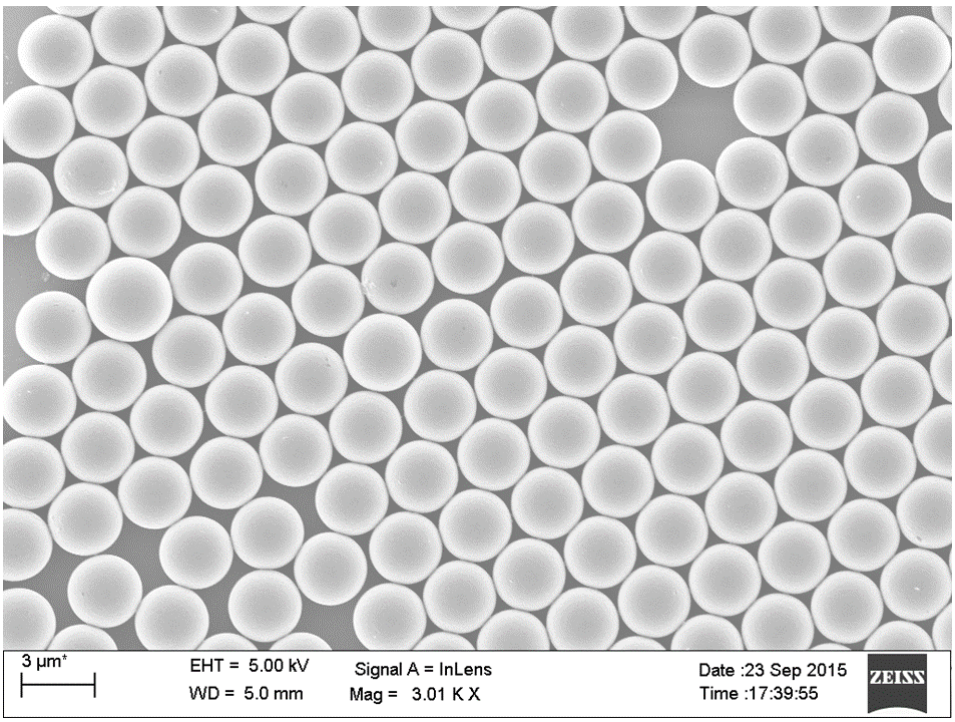

FIGURE 2.14: SEM image of polystyrene microspheres of mean diameter 2.85 μm with a standard deviation 0.15 μm quoted by the manufacturer (Bangs Laboratories Inc.) is obtained using a field effect scanning electron microscope (FESEM) from Carl Zeiss at an electron beam strength of 5 KeV.

scanned visual display unit such as a computer monitor [23]. The electron imaging in this work is performed using an electron beam of strength in the range of $2 - 5$ KeV.

Sample preparation for SEM imaging

Glass plates coated with indium tin oxide (ITO) are used to scan the dried samples. An ITO substrate is cleaned with acetone and a polystyrene (PS) suspension of concentration 0.01 wt% is added on the ITO coated side of the substrate using a pipette. The sample placed on the ITO substrate is dried overnight at 25°C and is then loaded on the SEM stage for imaging. Data acquisition and size measurements are carried out using SmartSEM (Carl Zeiss) and ImageJ softwares respectively. Figure 2.14 shows an SEM-micrograph of standard polystyrene spheres procured from Bangs Laboratories, Inc. The average diameter of PS particles estimated from approximately 1000

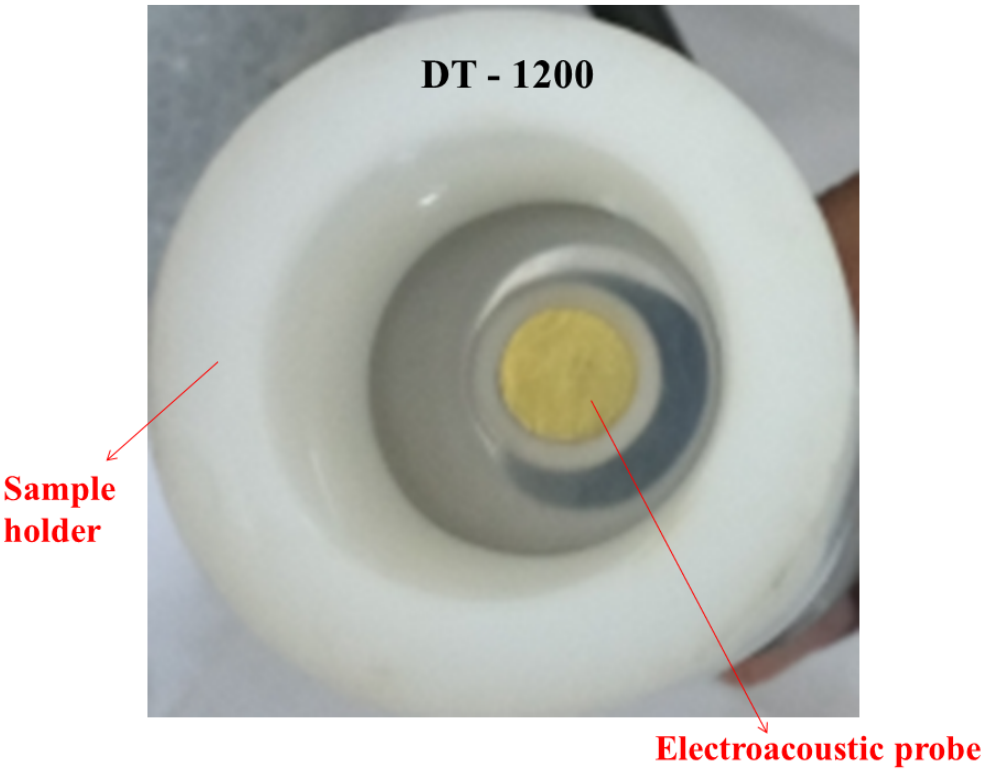

Figure 2.15: Electroacoustic probe from Dispersion Technology used for the zeta potential measurements of PNIPAM suspensions.

particles is 2.84 ± 0.21 μm which is very close to the value 2.85 ± 0.15 μm specified by the supplier.

2.3.4 Zeta potential measurements:

The zeta potentials (ζ) of the fluorescent PNIPAM suspensions are studied using an electroacoustic probe (figure 2.15) manufactured by Dispersion Technology, USA (Model DT-1200). A specially designed electroacoustic probe, DT-1200 of cylindrical shape and with a flat metal surface (figure 2.15), is immersed in the suspension. The probe, equipped with an ultrasound transducer, generates ultrasound waves of 3MHz frequency which propagate through the suspension. The diffuse charges of the electrical double layer surrounding the charged colloidal particles oscillate in response to the propagating ultrasound waves, producing a current called the colloidal vibration

current (CVI). The CVI and its phase are detected by the gold metal surface of the electroacoustic probe. The measured CVI data is analyzed by the DT-1200 software to compute ζ. Details of the instrument and the relevant electroacoustic principles can be found in [25]. For all the measurements, sample cells are held in a thermostated water bath at 25°C.

2.3.5 Confocal microscopy

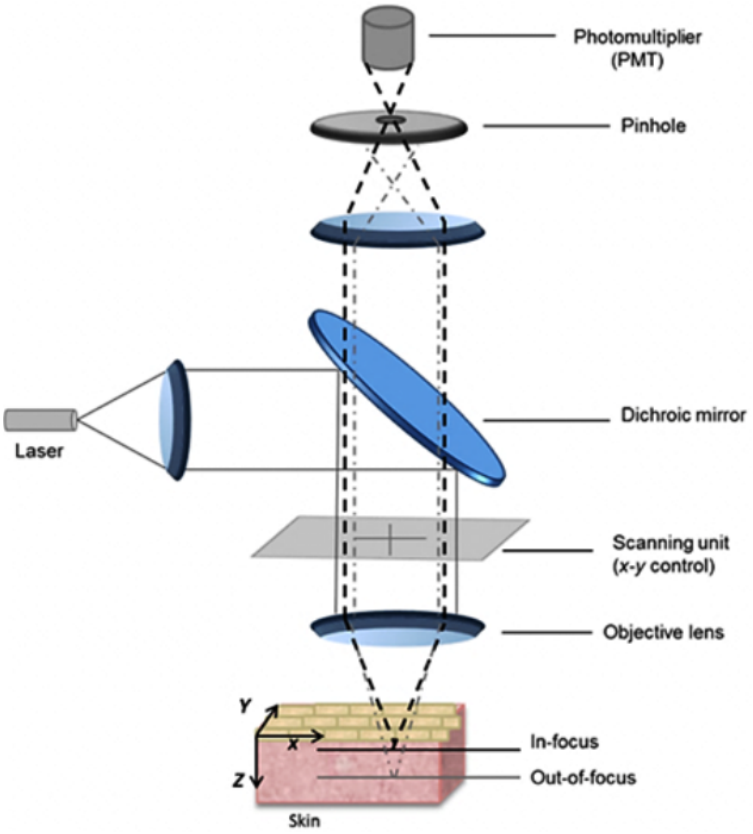

Figure 2.16: Schematic diagram of a confocal microscope setup. This figure is adapted from [26].

Confocal microscopy is an optical imaging technique used for increasing the optical resolution and contrast of a micrograph with the help of a spatial pinhole which blocks the out-of-focus light in image formation. In confocal microscopy, a three dimensional image of a sample can be obtained by the reconstruction of stacks of two

dimensional images captured at different depths of the sample. In this thesis work, confocal microscopy images of the samples are acquired using a Leica TCS SP8 confocal microscope system, with a 100x Nikon plan oil immersion objective (NA = 1.40). Figure 2.16 shows the schematic diagram of the main components of the confocal microscope setup [26]. The main components of a typical confocal microscope consist of a collimated laser light source, a dichroic mirror, a scanning unit, an objective lens, a pinhole and a detector (photo multiplier tube) [27]. The illumination in a confocal microscopy experiment is achieved by using a collimated laser beam. The laser beam from the source is reflected by a dichroic mirror. The reflected beam is then focused on the sample through an objective lens. The scanning unit contains a number of oscillating mirrors which allow the laser beam to scan the sample in the horizontal plane. The incident light excites the fluorescence probe in the sample. As a result, the light emitted from the sample at a different wavelength can pass through the dichroic mirror and is again focused at the upper pinhole aperture. With confocal laser scanning microscopy (CLSM), out-of-focus light (coming from places of the sample above or below the focus) is cut off before the beam hits the electronic detector due to the addition of a spatial filter containing a pinhole or slit. This improves the contrast of the image. In addition, high resolution images of the sample can be obtained with the help of CLSM. This increases the accuracy of the microscopic images.

Sample preparation for confocal microscope imaging

To visualize the PNIPAM collloidal particles under the confocal microscope, a suitable fluorescent dye named fluorescein is attached to these particles. All the glasswares required for designing the sample cell are sonicated in 1.5% v/v Hellmanex III solution at 70°C and then rinsed twice with Millipore water. These glasswares are ready to use after they are dried in a hot oven at 60°C for 1 h. This cleaning procedure ensures that a very tiny fraction of particles are stuck to the coverslip surfaces. A sample cell of thickness $\approx$100 μm and width 5 mm is prepared from a microscope slide and three cover slips. Two of them are used as spacers (number 0 thickness, supplied by

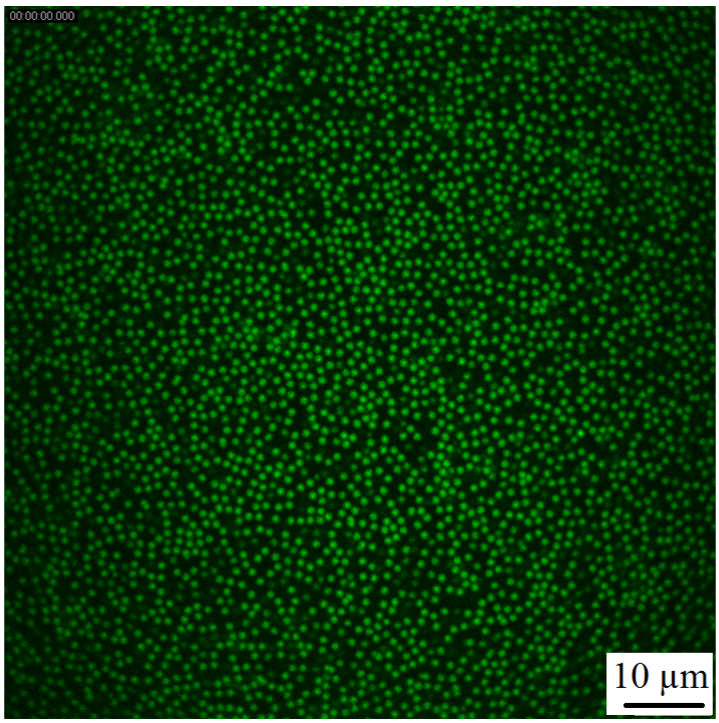

Figure 2.17: Confocal microscopy image of a 4 wt% suspension of fluorescent PNIPAM particles. The scale bar shown in the image is 10 μm.

Blue Star) with a horizontal gap between them and the third one on the top (number 1 thickness, supplied by Blue Star) to create a narrow capillary [28]. A coverslip of number 1 thickness is used to allow imaging of the particles using a high resolution 100x Nikon plain oil immersion objective (NA = 1.40). The sample cell is filled with the PNIPAM suspension of a certain concentration using a pipette and is sealed with UV glue. Confocal images of these particles are taken in a two dimensional slice at a height 10 μm away from the boundary of the cell to avoid wall effects [29]. The images are captured at a rate of 1 frame every 1.47 second over 300 seconds in a field of view of 91.18 μm x 91.18 μm containing more than 2000 particles. Figure 2.17 shows a confocal microscope image of 4 wt% suspension of fluorescent PNIPAM particles. The average size of PNIPAM particles estimated from approximately 2000 particles is 1.1 ± 0.2 μm.

References

[1] X. Wu, R.H. Pelton, A.E. Hamielec, D.R. Woods, W. McPhee, *Colloid Polym. Sci.*, 1994, **272**, 467.

[2] R.H. Pelton, H.M. Pelton, A. Morphesis, R.L. Rowell, *Langmuir*, 1989, **5(3)**, 816.

[3] T. Still, K. Chen, A. M. Alsayed, K. V. Aptowicz and A. G. Yodh, *J. Colloid and Interface Science*, 2013, **405**, 96.

[4] R. Acciaro, T. Gilányi, I. Varga, *Langmuir*, 2011, **27(12)**, 7917.

[5] T. Deptula (2015). *pNiPAM nanoparticles suspensions as model crowded complex systems: synthesis, characterization and properties* (Doctoral dissertation). Adam Mickiewicz University, Poznan, Poland..

[6] B. J. Berne and R. Pecora, Dynamic Light Scattering: With application to Chemistry, Biology and Physics, *Wiley-Interscience*, New York, 1976.

[7] H. Z. Cummins, F. D. Carlson, T. J. Herbert and G. Woods *Biophys. J.*, 1969, **9**, 518.

[8] Donald A. McQuarrie, Statistical Mechanics. Harper & Row, Publishers, Inc., New York 1976.

[9] R. Pecora, Dynamic Light scattering: Applications of Photon Correlation Spectroscopy, Plenum Press, New York, 1985.

[10] Norbert Wiener. Time Series. M.I.T Press, Cambridge, Massachusetts. p. 42, 1964.

[11] A. Einstein, *Annalen der Physik* (in German), 1905, **322(8)**, 549.

[12] A. J. F. Siegert, M.I.T. Rad. Lab. Rep., No.465, 1943.

[13] BI-200SM and BI-9000AT user manual, Brookhaven Instruments Corporation.

[14] Anton paar MCR 501 rheometer users manual.

[15] C. W. Macosko, Rheology: Principles, Measurements and Applications, VCH Publishers, New York, 1993.

[16] R. Seyboldt, D. Merger, F. Coupette, M. Siebenbürger, M. Ballauff, M. Wilhelmc and Matthias Fuchs, *Soft Matter*, 2016, **12**, 8825.

[17] R. Egerton, *Physical principles of electron microscopy: an introduction to TEM, SEM, and AEM*, Springer Science & Business Media, 2006.

[18] J. Bastacky, C. Wodley, R. LaBrie and C. Backhus, *Scanning*, 1987, **9**, 219–225.

[19] S. L. Erlandsen, C. Ottenwaelter, C. Frethem and Y. Chen, *BioTechniques*, 2001, **31**, 300–305.

[20] H. M. Wyss, M. Hütter, M. Müller, L. P. Meier and L. J. Gauckler, *Journal of colloid and interface science*, 2002, **248**, 340–346.

[21] R. P. Apkarian, E. R. Wright, V. A. Seredyuk, S. Eustis, L. A. Lyon, V. P. Conticello and F. M. Menger, *Microscopy and Microanalysis*, 2003, **9**, 286–295.

[22] R. Basak and R. Bandyopadhyay, *Langmuir*, 2013, **29**, 4350–4356.

[23] *User's Guide: ULTRA-PLUS FESEM*, Carl Zeiss, www.zeiss.com, 2013.

[24] S. J. B. Reed, *Electron microprobe analysis and scanning electron microscopy in geology*, Cambridge University Press, 2005.

[25] A. S. Dukhin and P. J. Goetz, *Characterization of Liquids, Nano and Microparticulates and Porous Bodies using Ultrasound.*, 2nd ed. Elsevier: New York, 2010.

[26] F. C. Rossetti, L. V. Depieri and M. V. L. B. Bentley, Confocal Laser Microscopy - Principles and Applications in Medicine, Biology, and the Food Sciences, 2013.

[27] Leica TCS SP8 confocal microscopy users manual.

[28] R. D. L. Hanes, C. Dalle-Ferrier, M. Schmiedeberg, M. C. Jenkinsa and S. U. Egelhaaf, *Soft Matter*, 2012, **8**, 2714.

[29] I. Cohen, T. G. Mason and D. A. Weitz, *Phys. Rev. Lett.*, 2004, **93**, 046001.

3

Effects of polydispersity on the glass transition dynamics of aqueous suspensions of soft spherical colloidal particles

3.1 Introduction

Thermoresponsive poly(*N*-isopropylacrylamide) (PNIPAM) hydrogel suspensions undergo a reversible volume phase transition above the lowest critical solution temperature (LCST) of ≈ 32 °C in water [1, 2]. This property of PNIPAM hydrogels provides

an opportunity to tune the particle size, volume fraction (ϕ) and inter-particle interactions in suspension by changing the temperature, thus enabling the study of the complex phase behaviours of soft colloidal suspensions [3, 4]. Furthermore, suspensions of PNIPAM colloidal particles have been in focus for their applications in controlled and self regulated drug delivery [5], bioconjugation [6], biosensors [7], pollution control [8], as viscosity modifiers of liquids and semisolids and in enhanced oil recovery [9] and chemical separation.

The zero-shear viscosity η_0 of a suspension of hard sphere colloids characterized by a significant polydispersity index (ratio of width and mean size of the probability distribution of particle sizes $\approx 10\%$) increases significantly when its volume fraction ϕ increases above $\phi \approx 0.53$, with the system entering a glassy state at $\phi_g \approx 0.58$ [10, 11]. The dynamics of the colloidal particles freeze at ϕ_g due to the kinetic constraints imposed on their motion. In order to understand the dramatic slowdown of the dynamics and the formation of disordered glassy phases, the use of colloidal suspensions having a significant polydispersity index (PDI $\approx 10\%$) is essential to prevent the system from entering a crystalline phase [12]. The increase in viscosity of fragile glass-forming molecular liquids with decreasing temperature (T) is well described by the Vogel-Fulcher-Tammann (VFT) law [13]. For colloidal glasses, the inverse of the volume fraction ($1/\phi$) of the colloidal suspension plays the role of temperature (T) [14–16]. To use the VFT law for colloidal glasses, therefore, T is replaced with $1/\phi$. The modified VFT equation, $\eta = \eta_0 \exp\left(\frac{D\phi}{\phi_0 - \phi}\right)$, explains the rise in the viscosity of a colloidal suspension with ϕ and its dramatic increase near $\phi = \phi_0$ [14, 16]. Here, $1/D$ is the fragility and accounts for the deviation of the viscosity from an Arrhenius dependence on ϕ as the sample approaches the glassy state. In the modified VFT equation, $\eta_0 = \eta\ (\phi = 0)$. A super-Arrhenius dependence of viscosity on the appropriate control parameter ($1/T$ or ϕ) is an ubiquitous characteristic of a fragile glass former [17].

An increase in the width of the particle size distribution in a mixture of fine powders (fly-ash and silica powder) increases the packing efficiency due to the decrease in the void fraction of the tapped powder beds [18]. Experiments and a self consistent theory

have shown that polydispersity affects the linear viscoelasticity of concentrated polymer solutions and melts [19]. In suspensions of the triblock copolymer Pluronic F127, it is shown that the addition of an anionic surfactant, sodium dodecyl sulfate (SDS), breaks the large spherical micelles into smaller, anisotropic polydisperse micelles [20]. This speeds up the dynamics of the constituents of these mixtures and results in more efficient packing configurations, with the particle volume fraction for random close packing exceeding the value for suspensions of monodisperse hard spheres.

The transition between different arrested states of concentrated binary colloidal mixtures characterized by large size asymmetries has been well-documented in the literature [21–23]. In these experiments, a significant polydispersity value, which is essential to form colloidal glasses, is maintained by mixing the colloidal particles of two different sizes in a certain ratio.

The colloidal glass transition has also been studied for colloidal suspensions comprising particles of significant size polydispersity without mixing batches of monodisperse colloidal particles. The colloidal glass transition of moderately polydisperse hard sphere colloids is reported to smear out with increase in polydispersity [14]. The presence of heterogeneous dynamics among the small particles, together with the decoupling of the dynamics of the smallest and largest particles in jammed suspensions of polydisperse hard sphere colloids, shifts ϕ_g to higher values [24]. Recently, Sollich et al. have reported that the phase boundaries of fluid, fluid-solid and solid phases of hard sphere colloids move to higher ϕ with increase in polydispersity [25]. Even though there are several simulation results and theoretical models that investigate the effects of polydispersity on the random close packing volume fraction ϕ_{rcp} of hard sphere colloids [12, 26], these results are difficult to verify experimentally because of the difficulty in systematically controlling the polydispersities of particles synthesized in the laboratory.

Particle polydispersity is an extremely crucial parameter in determining the fragilities and critical volume fractions of soft glassy suspensions. Local structural correlations in supercooled liquids, which have been shown in simulations to vary with

polydispersity, can profoundly influence the glass transition [27]. The intrinsic nonlinearity of a sample, Q_0, can be obtained by analysing the response at the third harmonic to the applied sinusoidal perturbation [28]. Q_0 is seen to grow as the glass transition is approached [29]. A detailed study of the approach of the suspension to a non-ergodic state in the presence of varying degrees of polydispersity is therefore important to obtain a clear understanding of the jamming transition. Both the stiffnesses and the polydispersities of soft particles are expected to affect the particle dynamics in suspensions near the colloidal glassy state. Since there is a conspicuous absence of detailed and systematic experimental studies of the dependence of the colloidal glass transition on the size polydispersity of the colloidal particles in suspension, we investigate the glass formation phenomenon in aqueous suspensions of soft PNIPAM particles by changing the particle polydispersity in a controlled manner, while keeping the crosslinker concentration constant to ensure approximately constant particle stiffnesses.

In this chapter, PNIPAM particles characterized by a wide range of PDI values (7.4%-48.9%) are successfully synthesized by using one-pot (OP) and semi-batch (SB) methods [30, 31]. In the OP method, PNIPAM particles of lower polydispersities are synthesized by varying the sodium dodecyl sulfate (SDS) concentration, while in the SB method, the size polydispersity of the particles is controlled by controlling the feeding rates of the monomer, co-monomer and crosslinker solutions into the reaction vessel. These simple methods are used to control the polydispersity of soft colloidal suspensions and to provide an easy alternative for synthesizing highly polydisperse particle suspensions without mixing batches of monodisperse PNIPAM particles. Dynamic light scattering (DLS) and scanning electron microscopy (SEM) are performed to study the thermoresponsivity and the size distributions of these particles.

The dynamic flow behaviors of the suspensions of soft PNIPAM colloids of varying polydispersities and with increasing particle volume fractions are studied in rheological experiments. Since these particles are soft and deformable, we quantify their packing in aqueous suspensions in terms of an effective volume fraction ϕ_{eff}. Zero shear viscosity η_0 values, which are extracted from steady shear measurements as a

function of the effective volume fraction ϕ_{eff}, are observed to increase with increase in ϕ_{eff} and show a dramatic increase at $\phi_{eff} = \phi_0$ (ϕ_0 is the volume fraction at which the viscosity η is expected to diverge). The η_0 *vs.* ϕ_{eff} data are analysed using the VFT law to calculate D and ϕ_0 values for suspensions of different ϕ_{eff}. Furthermore, the intrinsic nonlinearity of these suspensions at the third harmonic is measured from the stress response to oscillatory strains for several colloidal suspensions comprising particles over a range of PDIs. Our results, which confirm earlier numerical and analytical studies of polydisperse hard sphere colloidal systems [12, 24, 26, 32], demonstrate that the particle packing behaviour, and therefore the glass transition of colloidal suspensions, can be controlled effectively by controlling the polydispersities of the particles in suspension.

3.2 Sample preparation

PNIPAM colloidal particles obtained from semi-batch (SB) and one-pot (OP) methods (discussed in detail in section 2.2.1 of chapter 2) are purified by four successive centrifugations, decantations and redispersions in Milli-Q water to remove SDS, the remaining monomers, oligomers and impurities. Centrifugation is performed at a speed of $11,000$ rpm for 60 min. Dried polymers are collected by evaporating water from both the supernatant and residue. Fine PNIPAM powders are prepared by crushing and grinding the dried polymers with a mortar and pestle. For the dynamic light scattering (DLS) measurements and scanning electron microscopy (SEM) images, aqueous PNIPAM suspensions of a very dilute concentration ($c = 0.01$ wt%) are prepared by adding dried PNIPAM powder in Milli-Q water. However, for rheological measurements, aqueous PNIPAM suspensions of very high concentrations are prepared by adding dried PNIPAM powder in Milli-Q water. The suspension is then stirred for 24 hours and sonicated for 45 minutes. PNIPAM suspensions of different concentrations are prepared by diluting suspensions of the highest PNIPAM particle concentration with Milli-Q water. The concentration is measured in wt% (the weight of the dried

PNIPAM powder in 100 ml of water).

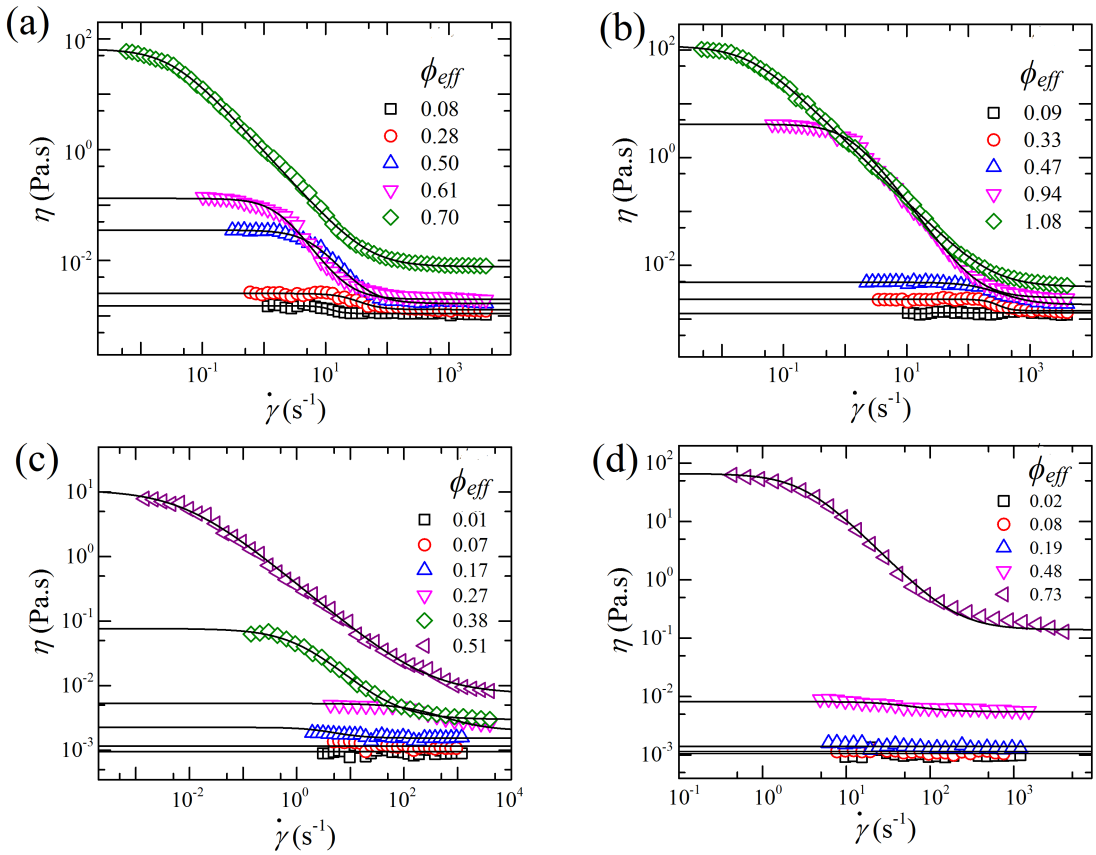

Figure 3.1: Viscosity η *vs.* shear rate $\dot{\gamma}$ of aqueous suspensions of PNIPAM particles of (a) mean diameter 156 nm and polydispersity index (PDI) of 7.4%, (b) mean diameter 469 nm and polydispersity index (PDI) of 13.5%, (c) mean diameter 1.24 m and polydispersity index (PDI) of 15.3% and (d) mean diameter 2.78 m and PDI of 48.9% at 25°C, for several different effective volume fractions. The solid lines are the fits to equation 3.1.

3.3 Results and discussion

Steady state flow experiments of PNIPAM suspensions are performed at 25°C. The viscosity η of each suspension is measured by varying the shear rate $\dot{\gamma}$ between 0.001 and 4000 s^{-1}. The zero-shear viscosity η_0 of each suspension is calculated by fitting

the viscosity η versus shear rate $\dot{\gamma}$ curve (figure 3.1) with the Cross model [33]:

$$\frac{\eta - \eta_\infty}{\eta_0 - \eta_\infty} = \frac{1}{1 + (k\dot{\gamma})^m} \tag{3.1}$$

where η_0 and η_∞ correspond to the viscosity plateaus at very low and very high shear rates respectively, k is a time constant related to the relaxation time of the polymer in solution and m is a dimensionless exponent. The relative viscosity η_{rel} of a PNIPAM suspension is defined as the ratio of its zero-shear viscosity η_0 and the viscosity of water η_s: $\eta_{rel} = \eta_0/\eta_s$.

The PNIPAM particles are soft and start deforming in the presence of neighbouring particles at volume fractions above the random close packing volume fraction of undeformed monodisperse spheres ($\phi_{RCP} = 0.64$) [15, 16]. Since the volume fraction ϕ does not account for the particle deformations of these soft particles, we consider a modified parameter called the effective volume fraction ϕ_{eff}. ϕ_{eff} of a PNIPAM suspension is obtained from the relation $\phi_{eff} = nV_d$, where n is the number of particles per unit volume and $V_d = \pi<d_h>^3/6$ is the volume of an undeformed particle of mean hydrodynamic diameter $<d_h>$ in a very dilute suspension in the fully swollen state (25°C) [16]. The above relation can be written in terms of the polymer concentration of the microgel packing c as $\phi_{eff} = c/c_p$ [34], where $c_p = m_p/V_d$ is the polymer concentration inside each particle in the swollen state and m_p is the molecular weight of each particle. The Batchelor's equation relates η_{rel} of the suspension with its ϕ_{eff} as follows: [35, 36]:

$$\eta_{rel} = 1 + 2.5\phi_{eff} + 5.9\phi_{eff}^2 \tag{3.2}$$

The polymer mass concentration of the suspension can be converted into the effective volume fraction by substituting $\phi_{eff} = c/c_p$ in equation 3.2:

$$\eta_{rel} = 1 + 2.5(c/c_p) + 5.9(c/c_p)^2 \tag{3.3}$$

The Batchelor's law is valid for only dilute and relatively monodisperse hard sphere

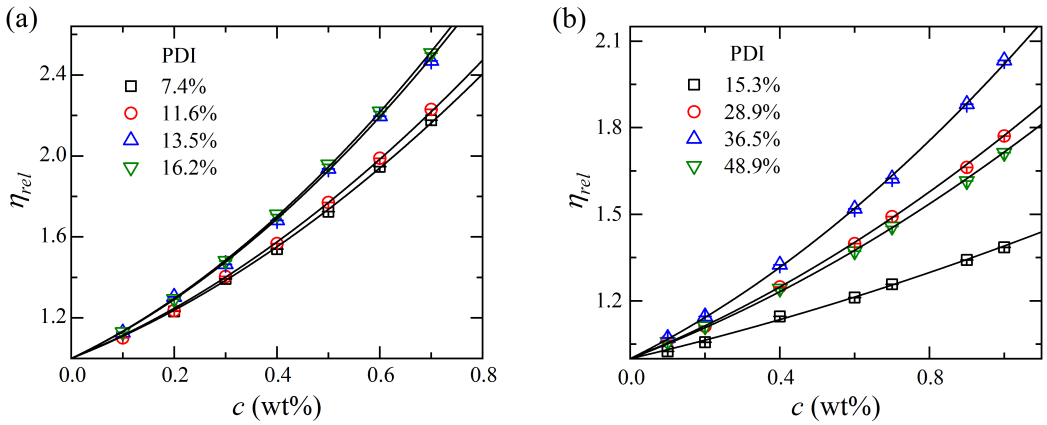

Figure 3.2: Relative viscosity η_{rel} *vs.* polymer mass concentration c in wt% at 25°C for suspensions of PNIPAM particles of different polydispersity indices (PDIs) synthesized by (a) the OP method and (b) the SB method. The solid lines are fits to equation 3.3.

Method	PDI	$<d_h>$	c_p (wt%)
OP	7.4%	156 nm	2.48 ± 0.03
OP	11.6%	402 nm	1.71 ± 0.01
OP	13.5%	469 nm	1.69 ± 0.01
OP	16.2%	875 nm	1.68 ± 0.01
SB	15.3%	1.24 μm	1.81 ± 0.02
SB	28.9%	1.73 μm	1.87 ± 0.01
SB	36.5%	2.38 μm	1.84 ± 0.01
SB	48.9%	2.78 μm	1.83 ± 0.02

Table 3.1: Polydispersity index (PDI), mean diameter $<d_h>$ and polymer concentration inside each particle in the swollen state c_p, obtained from the fits of the data in figure 3.2 to equation 3.3, for PNIPAM particles synthesized by both OP and SB methods. The estimates are made from DLS experiments performed at 25°C and at a scattering angle $\theta = 90°$.

suspensions [35]. In our experiments, only dilute concentrations ($\phi_{eff} < 0.2$) of polydisperse PNIPAM suspensions are used to rule out inter-particle interactions [37]. Our assumption is validated by the excellent fits of the data to equation (3.3) (figure 3.2). The values of c_p, calculated by fitting equation (3.3) to the experimental data displayed in figure 3.2, are tabulated in table 3.1 for PNIPAM particles of different mean hydrodynamic diameters $<d_h>$ and polydispersity indices (PDIs). The fitted values of the polymer concentration inside each particle, c_p, is independent of the polymer mass

concentration of the suspension c and depends only on the particle preparation protocol. $\phi_{eff} = c/c_p$ is therefore used to determine the value of the effective volume fraction ϕ_{eff} at higher concentrations for the suspensions of the same batch of particles.

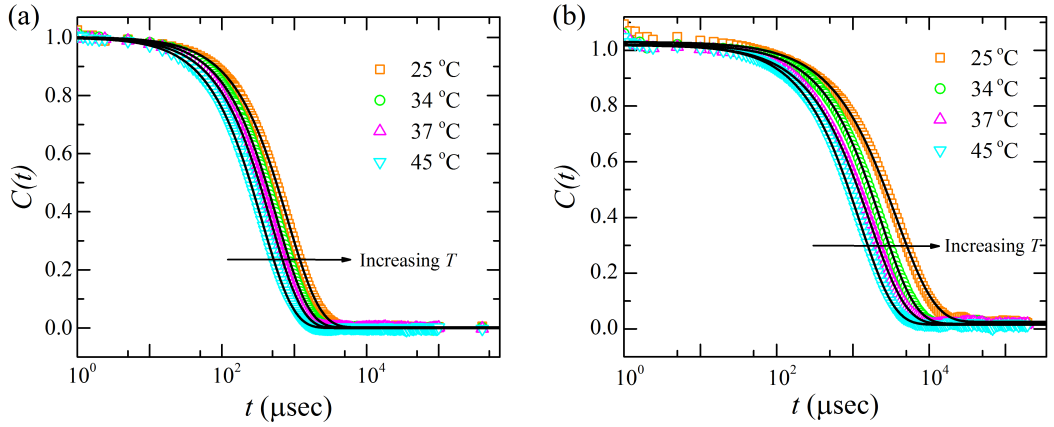

Figure 3.3: The normalised intensity autocorrelation functions $C(t)$ *vs.* the delay time t of PNIPAM particles synthesized by (a) the one-pot (OP) method at an SDS concentration of 0.06 g/L and by (b) the semi-batch (SB) method at a flow rate of the reaction ingredients of 0.7 mL/min at different temperatures and at a scattering angle $\theta = 90°$. The solid lines are fits to the equation: $C(t) = [\exp(-t/\tau)^{\beta}]^2$.

For a suspension of polydisperse particles of effective volume fraction $\phi_{eff} = 0.006$, the decays of the normalized autocorrelation $C(t) = \frac{g^{(2)}(q,t)-1}{A}$ are fit to the stretched exponential of the form, $C(t) = [\exp(-t/\tau)^{\beta}]^2$. Here, A is used to normalize the autocorrelation data to 1 at $t = 0$. The stretching exponent β is used to calculate the mean and the second moment of the relaxation time spectrum of the particles in suspension using the relations $<\tau>=(\frac{\tau}{\beta})\Gamma(1/\beta)$ and $<\tau^2>= (\frac{\tau^2}{\beta})\Gamma(2/\beta)$ respectively [38], where Γ is the Euler Gamma function. The mean hydrodynamic diameter $<d_h>$ and the standard deviation or width of the particle size distribution σ were obtained by using $<d_h>= \frac{k_B T<\tau>q^2}{3\pi\eta}$ and $\sigma = \frac{k_B T\sqrt{<\tau^2>-<\tau>^2}q^2}{3\pi\eta}$ respectively [39]. The values of mean relaxation time $<\tau>$ and mean hydrodynamic diameter $<d_h>$, obtained by fitting the intensity autocorrelation data of a PNIPAM suspension at $\phi_{eff} = 0.006$, synthesized

Method	Temperature (°C)	β	$< \tau >$	$<d_h>$ (μm)
OP	25	0.987 ± 0.002	1646 ± 5	0.40
OP	34	0.995 ± 0.001	1076 ± 2	0.31
OP	37	0.998 ± 0.001	792 ± 2	0.26
OP	45	0.999 ± 0.001	613 ± 1	0.24
SB	25	0.884 ± 0.006	9262 ± 48	2.38
SB	34	0.915 ± 0.004	4809 ± 23	1.52
SB	37	0.926 ± 0.004	4233 ± 12	1.42
SB	45	0.954 ± 0.003	3315 ± 06	1.31

Table 3.2: Stretching exponent β, mean relaxation time $< \tau >$ and average diameter $<d_h>$ of PNIPAM particles, obtained by fitting to the data plotted in figure 3.3, for suspensions of PNIPAM particles synthesized by the one-pot (OP) method at an SDS concentration of 0.06 g/L and by the semi-batch (SB) method at a flow rate of the reaction ingredients of 0.7 mL/min at different temperatures.

in the one-pot (OP) method at an SDS concentration of 0.06 g/liter (figure 3.3(a)), and in the semi-batch (SB) method at a flow rate of 0.7 mL/min of the flow rates of the reaction ingredients (figure 3.3(b)), are seen to decrease with the increase in temperature (table 3.2). The normalized electric field autocorrelation function $g^{(1)}(q,t)$ is related to the line width distribution $G(\Gamma)$ by the relation $g^{(1)}(q,t) = <E(t,q)E^*(0,q)> = \int_0^\infty G(\Gamma)\exp(-\Gamma t)d\Gamma$ [40, 41]. Here, Γ is the decay rate which is related to the self diffusion coefficient D_0 by the relation $\Gamma = D_0 q^2$. The particle size distribution of each PNIPAM particle suspension is obtained from the inverse Laplace transform of $g^{(1)}(q,t)$ [40, 41]. The size distribution of PNIPAM particles is quantified by a dimensionless polydispersity index (PDI) which is defined as the ratio of the width of the particle size (σ) and the mean hydrodynamic diameter ($<d_h>$) of the particle size distribution.

The plots of hydrodynamic particle size distributions, estimated from DLS at a scattering angle θ=90°, for PNIPAM particles synthesized by the OP and the SB methods are shown in figure 3.4. The sizes ($<d_h>$), swelling ratios (α) and polydispersity indices (PDIs), estimated for all the synthesized PNIPAM particles in aqueous suspensions in the DLS experiments, are listed in table 3.3. It is seen from figure 3.4 and table 3.3 that the mean and the width of the size distribution of the PNIPAM particles, synthesized using the OP method, increase with the decrease in concentration of SDS.

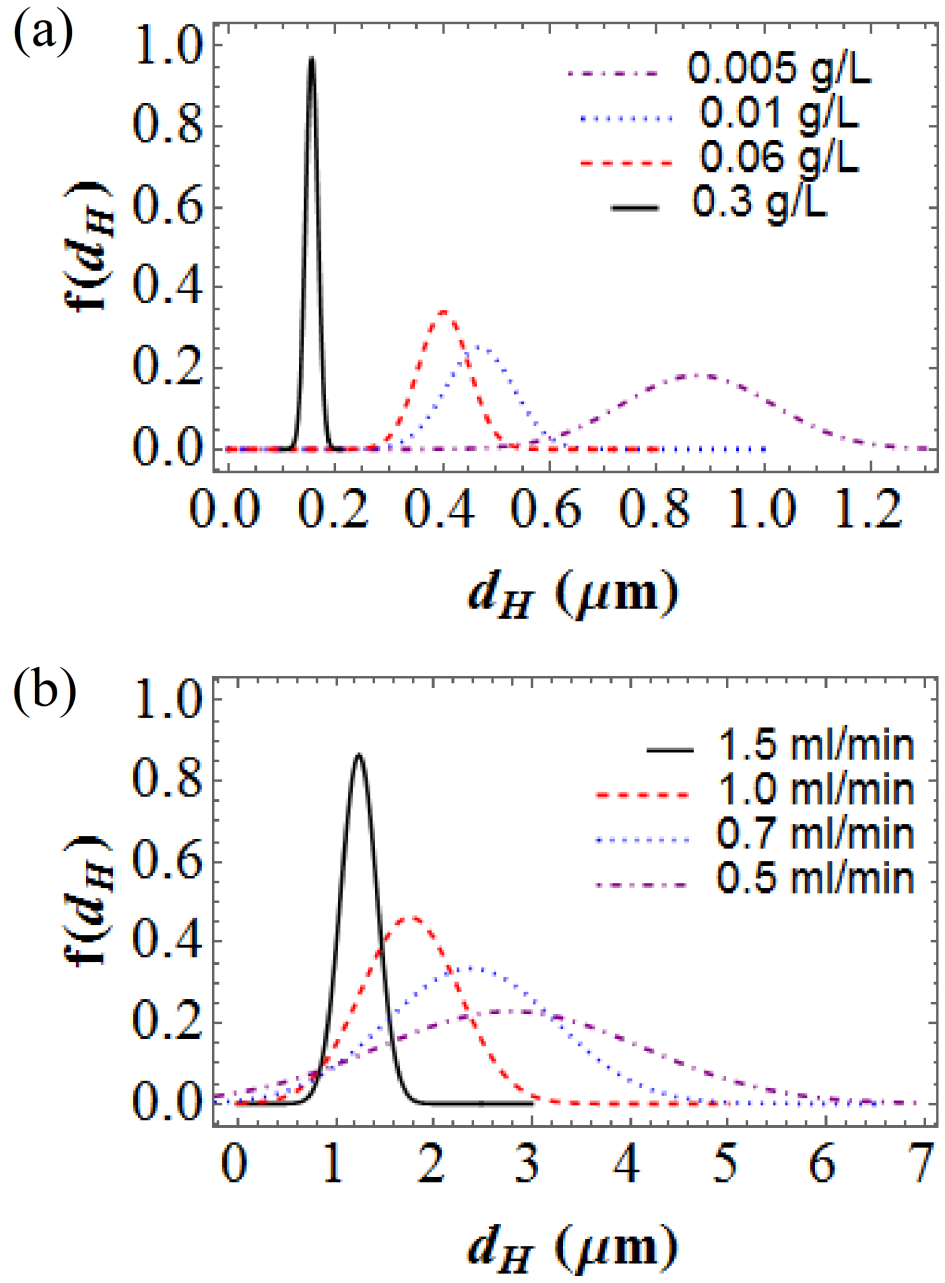

Figure 3.4: (a) The hydrodynamic particle size distributions of PNIPAM particles in aqueous suspensions measured from DLS experiments for particles synthesized by the OP method at different SDS concentrations (g/liter) at 25°C and at a scattering angle θ=90°. (b) The hydrodynamic particle size distribution of PNIPAM particles measured from DLS experiments for particles synthesized by the SB method at different flow rates (ml/min) of the reaction ingredients at 25°C and at a scattering angle θ=90°.

Method	SDS conc./Flow rate	$<d_{25^\circ C}>$	$\sigma(\mu m)$	PDI	α
OP	0.3 g/L	0.16 μm	0.0119	7.4%	1.72 ± 0.01
OP	0.06 g/L	0.40 μm	0.0464	11.6%	1.71 ± 0.01
OP	0.01 g/L	0.47 μm	0.0635	13.5%	1.69 ± 0.01
OP	0.005 g/L	0.88 μm	0.1424	16.2%	1.68 ± 0.01
SB	1.5 mL/min	1.24 μm	0.1900	15.3%	1.81 ± 0.02
SB	1.0 mL/min	1.73 μm	0.5000	28.9%	1.87 ± 0.01
SB	0.7 mL/min	2.38 μm	0.8690	36.5%	1.84 ± 0.01
SB	0.5 mL/min	2.78 μm	1.3595	48.9%	1.83 ± 0.02

Table 3.3: Mean hydrodynamic diameters ($<d_h>$), standard deviation of particle sizes (σ) at 25°C, polydispersity indices (PDI) and swelling ratios (α) measured from dynamic light scattering experiments at θ=90° for suspensions of PNIPAM particles synthesized by varying the SDS concentration in the OP method and by varying the flow rate of the reaction ingredients in the SB method.

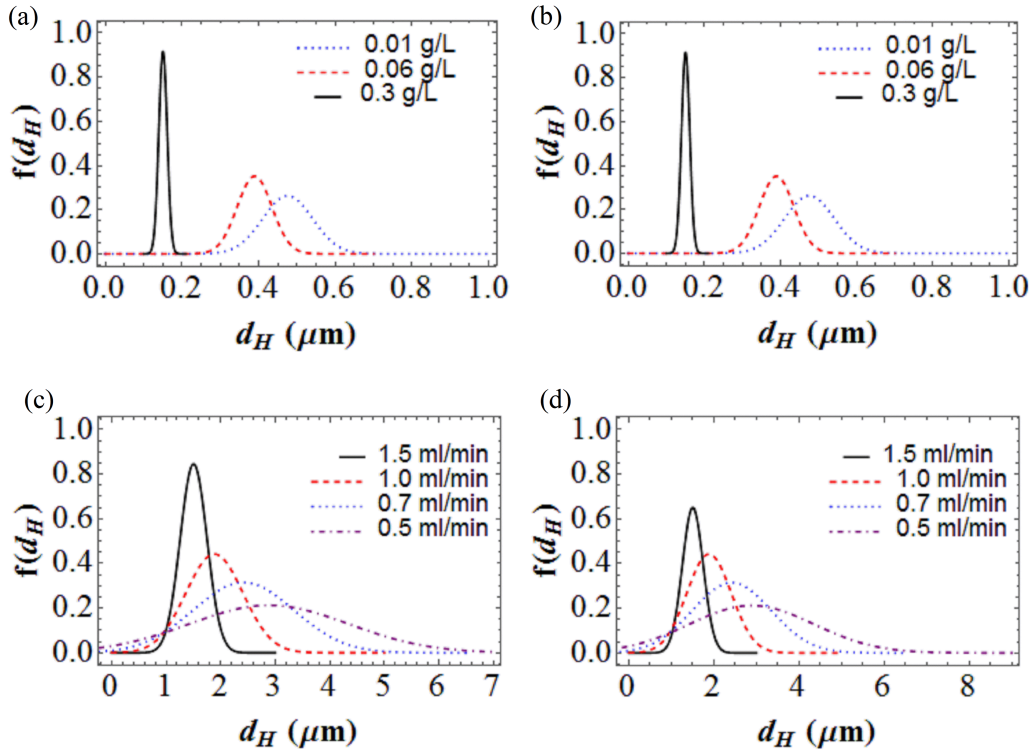

Figure 3.5: (a-b) Particle size distributions of PNIPAM particles measured from DLS experiments for particles synthesized by the OP method at different SDS concentrations (g/L) at 25°C and at scattering angles (a) θ = 75° and (b) θ = 60° (c-d) Particle size distributions of PNIPAM particles measured from DLS experiments for particles synthesized by the SB method at different flow rates (ml/min) of the reaction ingredients at 25°C and at scattering angles (c) θ = 75° and (d) θ = 60°.

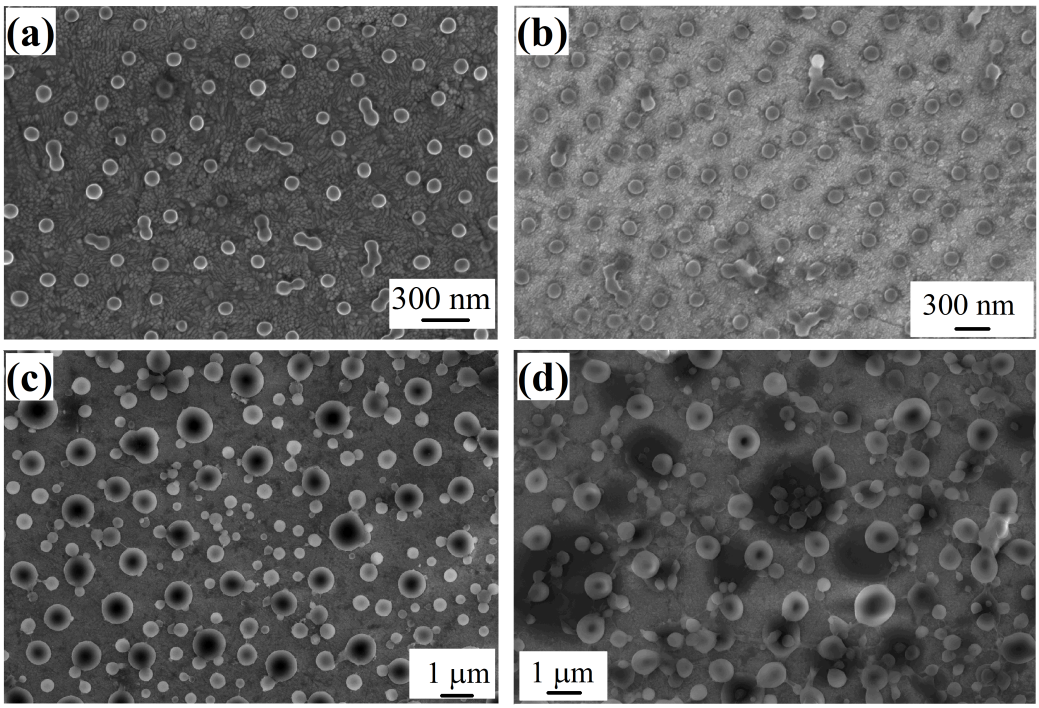

Figure 3.6: (a-b) Representative SEM micrographs of dry PNIPAM particles synthesized by the OP method (a) particle PDI 11.9% at SDS concentration of 0.06 g/liter and (b) particle PDI 16.2% at SDS concentration 0.01 g/liter. (c-d) Representative SEM micrographs of dry PNIPAM particles, synthesized by the SB method (c) particle PDI 46.9% at a flow rate of 0.7 mL/min and (d) particle PDI 53.8% at a flow rate of 0.5 mL/min.

Using this method, we have synthesized particles of PDIs varying from 7.4% to 16.2%. Particles of higher polydispersity (PDIs between 15.3% and 48.9%) are synthesized in the SB method by varying the flow rate of the reaction ingredients . It is seen from figure 3.4 and table 3.3 that the decrease in the flow rate of the reaction ingredients in the SB method increases the mean and the width of the size distribution of the PNIPAM particles. The increase in mean particle sizes and PDIs with decreasing SDS concentration in the OP method and with decreasing flow rates of the reaction ingredients in the SB method have been verified by making additional measurements at lower scattering angles. The data are plotted in figure 3.5. The wide range of PDI values achieved for the soft PNIPAM particles allows us to systematically investigate the effects of particle size polydispersity on the approach of their concentrated suspensions towards the colloidal glass transition.

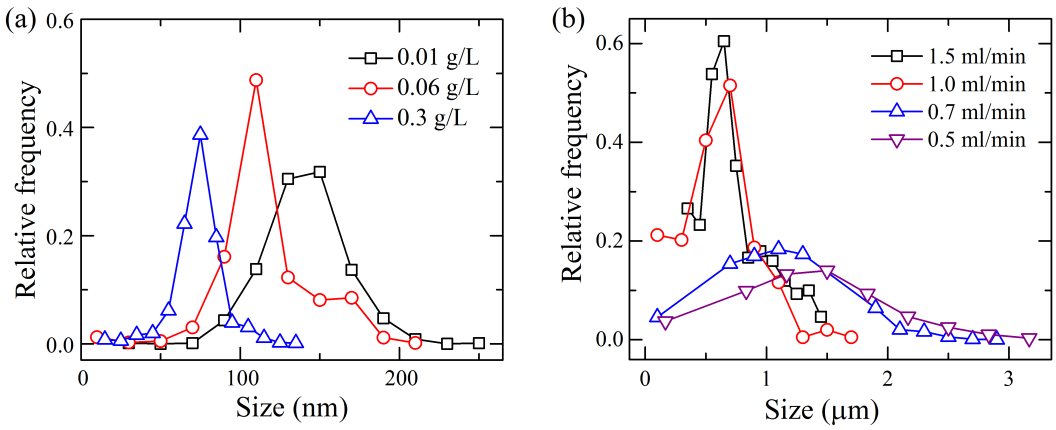

Figure 3.7: Particle size distribution calculated from SEM images for dried PNIPAM particles synthesized by (a) the OP method at different SDS concentrations (g/L) and (b) the SB method at different flow rates (ml/min) of the reaction ingredients. Representative images are presented in figure 3.6.

Direct visualization of the PNIPAM particles synthesized by the OP and the SB methods is achieved using SEM imaging. Representative SEM images are displayed in figure 3.6. The average sizes and particle size distributions estimated from SEM images are shown in table 3.4 and figure 3.7. These results are in excellent agreement with the DLS results (figure 3.4 and table 3.4). However, the sizes of the particles measured from SEM images are found to be less than those obtained by DLS at 45°C by a factor of almost 1.2 – 2.0 (table 3.4). This is explained by considering that above the LCST (45°C), the particles in suspension shrink by expelling water from their interior, but are still not collapsed completely. The DLS measurements therefore reveal larger values of $<d_h>$ when compared to the SEM experiments in which the particles are in the dried state.

The particle stiffness is characterized by measuring the temperature dependence of the sizes of the PNIPAM particles using DLS. The corresponding thermoresponsive curves of the PNIPAM particles in suspensions are shown in figure 3.8. It is seen that the swelling ratio α is approximately insensitive to the method of synthesis (figure 3.8). This is explained by considering that a fixed concentration of crosslinker MBA is

Method	SDS conc./Flow rate	DLS ($d_{20^\circ C}$)	DLS ($d_{45^\circ C}$)	α	SEM (dried sample)
OP	0.3 g/L	0.16 μm	0.09 μm	1.72	0.075 μm
OP	0.06 g/L	0.40 μm	0.24 μm	1.71	0.11 μm
OP	0.01 g/L	0.47 μm	0.28 μm	1.69	0.15 μm
OP	0.005 g/L	0.89 μm	0.53 μm	1.68	0.28 μm
SB	1.5 mL/min	1.35 μm	0.74 μm	1.81	0.61 μm
SB	1.0 mL/min	1.81 μm	0.97 μm	1.87	0.71 μm
SB	0.7 mL/min	2.41 μm	1.31 μm	1.84	1.06 μm
SB	0.5 mL/min	2.93 μm	1.60 μm	1.83	1.32 μm

Table 3.4: The particle sizes and the swelling ratios (α), measured from dynamic light scattering (DLS) and scanning electron microscopy (SEM) are reported for suspensions of PNIPAM particles synthesized by varying the SDS concentration in the one-pot OP method and by varying the flow rate of the reaction ingredients in the semi-batch SB method. SEM images of the particles are taken in their dried state. In this table, $d_{20^\circ C}$ and $d_{45^\circ C}$ are the diameters of the particles measured by DLS at 20°C and 45°C respectively.

used in both the OP and SB methods. It can therefore be concluded that the swelling behaviour, and therefore, the CLD inside each particle is approximately insensitive to changes of PDI.

The dynamics of glass formation as a function of PDIs in suspensions of soft PNIPAM particles having PDIs between 7.4% and 48.9% is investigated using rheology at 25°C. The colloidal glass transition is expected to occur at a volume fraction ϕ_g at which the viscosity shows an apparent divergence. It is well known that for colloidal glasses, the volume fraction ϕ plays a role analogous to the inverse of the temperature T, with the dynamics slowing down with increasing ϕ due to the increase in kinetic constraints [42, 43]. Since ϕ_{eff} is a correct measure of the concentration of soft PNIPAM particles in aqueous suspensions, we estimate the relative zero shear viscosity η_{rel} as a function of ϕ_{eff}. η_{rel} *vs.* ϕ_{eff} plots are depicted in figure 3.9. η_{rel} values are observed to increase by four decades over the range of ϕ_{eff} explored here. The values of η_{rel} of suspensions of soft PNIPAM particles in the arrested state are higher than the η_{rel} values reported for hard sphere colloidal particle suspensions [44, 45]. The observed higher values of η_{rel} in these suspensions of polydisperse, deformable PNIPAM particles approaching ϕ_g are due to the increase in the number of contacts and the

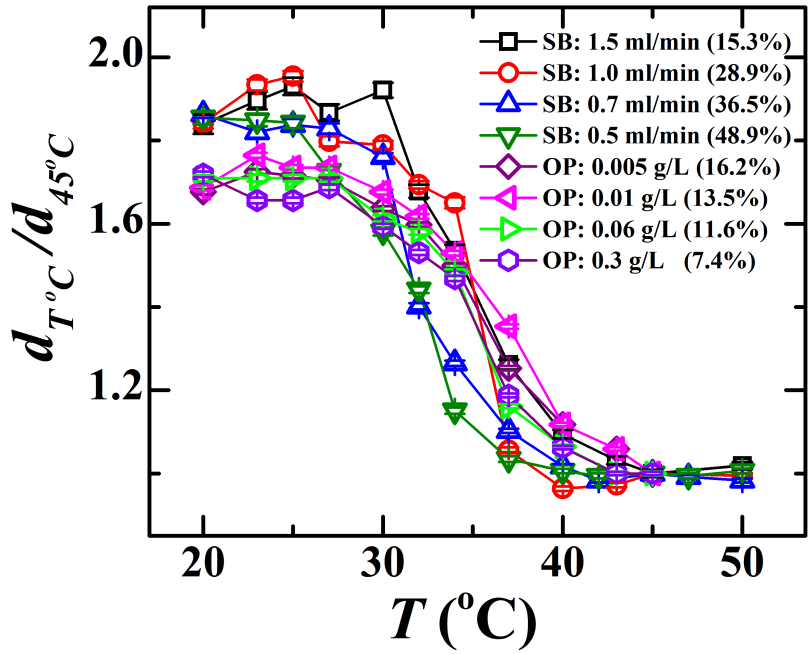

Figure 3.8: Temperature dependent swelling ratio $d_{T\circ C}/d_{45\circ C}$ as a function of temperature T°C for suspensions of PNIPAM particles of different PDIs synthesized by the SB method at different flow rates (ml/min) of the reaction ingredients, and by the OP method, synthesized using different concentrations (g/L) of SDS, estimated from DLS experiments at a scattering angle θ=90°.

number of neighbours surrounding a given particle, which result in the enhancement of the particle packing efficiency. The values of the fragility, $1/D$, and the effective volume fraction ϕ_0, at which η_{rel} increases dramatically, are obtained by fitting the η_{rel} *vs.* ϕ_{eff} data (figure 3.9) to the VFT equation [14, 16]:

$$\eta_{rel} = \exp\left(\frac{D\phi_{eff}}{\phi_0 - \phi_{eff}}\right) \tag{3.4}$$

Here, D is the fragility parameter. The fragility $(1/D)$ in glass-forming liquids is defined as the deviation of the viscosity from Arrhenius growth upon cooling rapidly (for supercooled liquids) or with increasing ϕ (for colloidal suspensions) [17, 46].

The values of $1/D$ and ϕ_0, obtained from fits to the VFT law for suspensions of PNIPAM particles with varying PDIs, are reported in table 3.5. It is seen from table

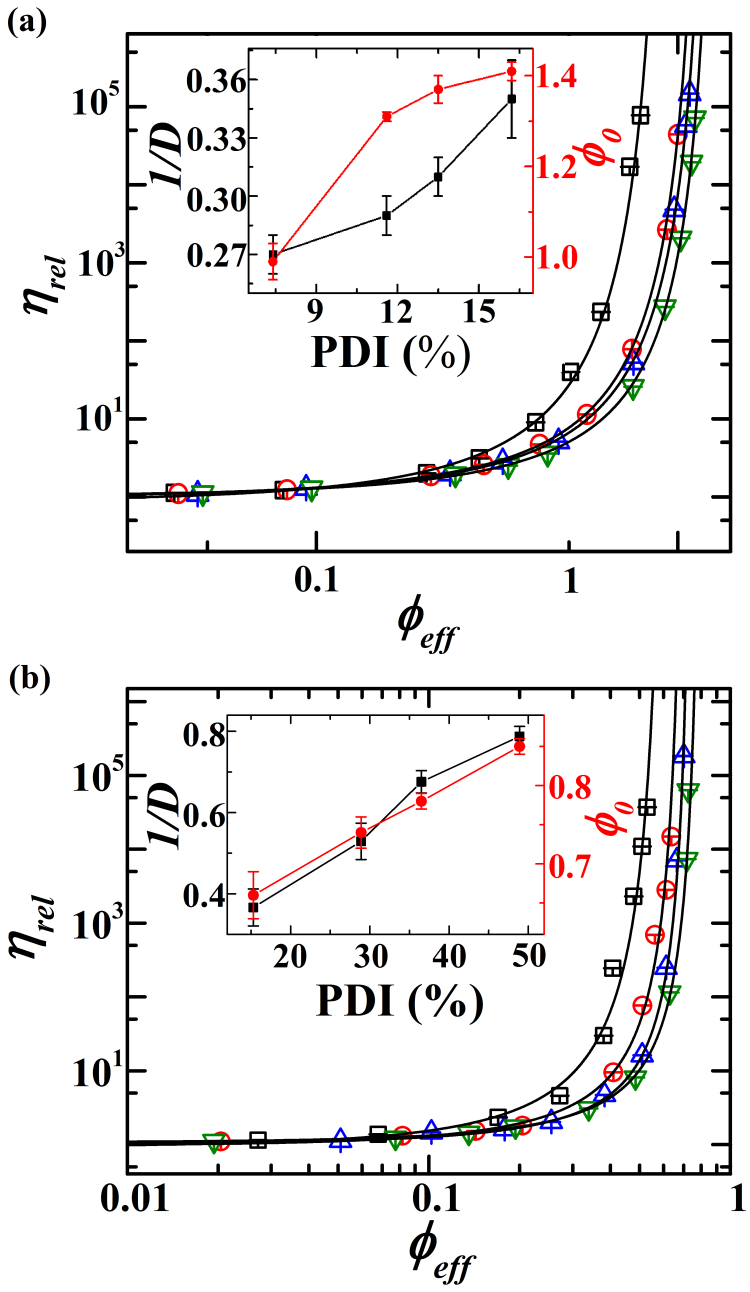

Figure 3.9: (a) Relative viscosity η_{rel} *vs.* effective volume fraction ϕ_{eff} of suspensions of PNIPAM particles synthesized by the OP method at different concentrations of SDS and characterized by different PDIs: 7.4 % (□), 11.6 % (○), 13.5 % (△), 16.2 % (∇) at 25°C. (b) η_{rel} *vs.* ϕ_{eff} of suspensions of PNIPAM particles synthesized by the SB method at different flow rates of reaction ingredients and characterized by different PDIs: 15.3 % (□), 28.9 % (○), 36.5 % (△), 48.9 % (∇) at 25°C. The solid lines are the VFT fits (equation 3.4) to the data. Insets show the fitted values of fragility $1/D$ (■) and ϕ_0 (●) *vs.* PDI of the PNIPAM suspensions.

Method	PDI	$1/D$	ϕ_0
OP	7.4%	0.27 ± 0.01	0.99 ± 0.04
OP	11.6%	0.29 ± 0.01	1.31 ± 0.01
OP	13.5%	0.31 ± 0.01	1.37 ± 0.03
OP	16.2%	0.35 ± 0.02	1.41 ± 0.02
SB	15.3%	0.37 ± 0.05	0.66 ± 0.03
SB	28.9%	0.53 ± 0.04	0.74 ± 0.02
SB	36.5%	0.68 ± 0.03	0.78 ± 0.01
SB	48.9%	0.79 ± 0.02	0.85 ± 0.01

Table 3.5: Fragility $1/D$ and ϕ_0 values obtained by fitting the VFT equation to the relative viscosity η_{rel} *vs.* effective volume fraction ϕ_{eff} data (figure 3.9) for suspensions of PNIPAM particles of different PDIs.

3.5 that for particles synthesize using both OP and SB methods, $1/D$ and ϕ_0 increase with increase in PDIs. It is noted that the ϕ_0 values for suspensions of particles of lower polydispersities, synthesized by the OP method, are higher than those of the suspensions of the particles synthesized by the SB method. This can be attributed to the rigid cores and loose shells of the particles produced in the OP method [47]. The heterogeneous crosslinking density (CLD) of the PNIPAM particles synthesized by the OP method produces highly crosslinked rigid cores, and less crosslinked hairy shells [48]. At sufficiently high volume fractions, the core-shell particles deform up to the core because of the presence of the hairy shells. This shifts ϕ_0 to higher values. The PNIPAM particles synthesized by the SB method, in contrast, have a uniform CLD within each particle [30]. This is confirmed by direct visualization (figure 3.10). The larger polymer densities at the core of the particles obtained in the OP method create a larger refractive index mismatch between the particles and the background solvent (water). This leads to stronger light scattering and more suspension turbidity in suspensions of these particles when compared to the particles synthesized by the SB method. At fixed volume fraction above ϕ_{RCP}, therefore, the particles synthesized by the SB method deform less when compared to the particles synthesized by the OP method.

The observed increase of ϕ_0 with increasing PDIs for the PNIPAM particle suspensions studied here is in agreement with theoretical predictions and simulation results

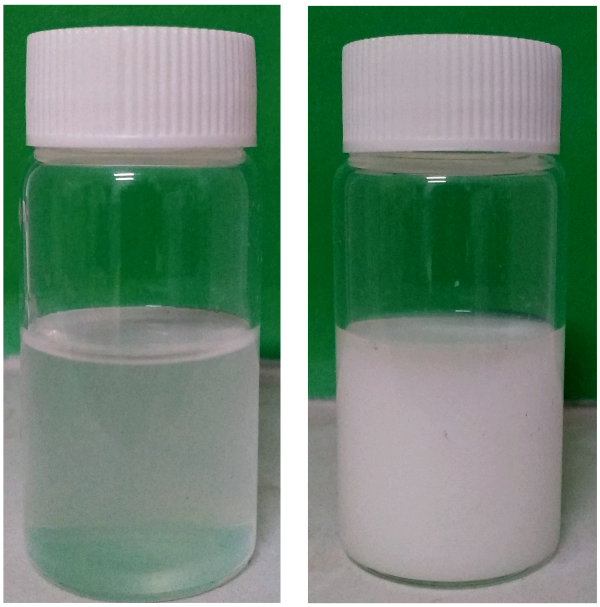

Figure 3.10: Direct visualization of aqueous suspensions of PNIPAM particles of size 1.24 μm, synthesized by the SB method (left), and of size 0.88 μm, synthesized by the OP method (right), at an effective volume fraction ϕ_{eff} = 0.07 at 25°C.

for close packed hard sphere colloids [12, 26, 32] and can be explained by considering that the packing of smaller spherical particles in between bigger spherical particles becomes increasingly efficient as the sample PDI increases. It has been shown that suspensions of polydisperse hard spheres can stay fluidized at volume fractions higher than the random close packing volume fraction of monodisperse hard spheres [14, 24]. This is due to the high degree of heterogeneous dynamics prevalent among the small particles whose mobilities are higher than those of the bigger particles in the polydisperse mixture [24]. Heterogeneous dynamics, and the resultant decoupling of the dynamics of the small and big particles in the polydisperse suspensions, result in the big particles forming an arrested state, with the smaller particles of higher diffusivities smearing out the glass transition to a certain degree [24]. The increased prevalence of heterogeneous dynamics and the increased packing efficiency of PNIPAM microparticles with increase in the polydispersity index can therefore explain the data in figure

3.9.

The fragility of glass forming liquids arises from the presence of slow and fast moving groups of molecules or particles called dynamical heterogeneities (DHs). The observed high fragility values of these glassy suspensions of polydisperse particles can be understood by considering an increase in the concentration of the DHs [49, 50]. Indeed, the fragility values increase by almost a factor of three over the range of PDIs explored in this work (table 3.5 and solid squares in the insets of figure 3.9(a) and 3.9(b)). Dynamical heterogeneity in a polydisperse system can be correlated with the intrinsic nonlinearity of the sample. Intrinsic nonlinearity is the nonlinear mechanical response of the system and is related with the various structural relaxation processes that are affected by the polydispersity of the material [29].

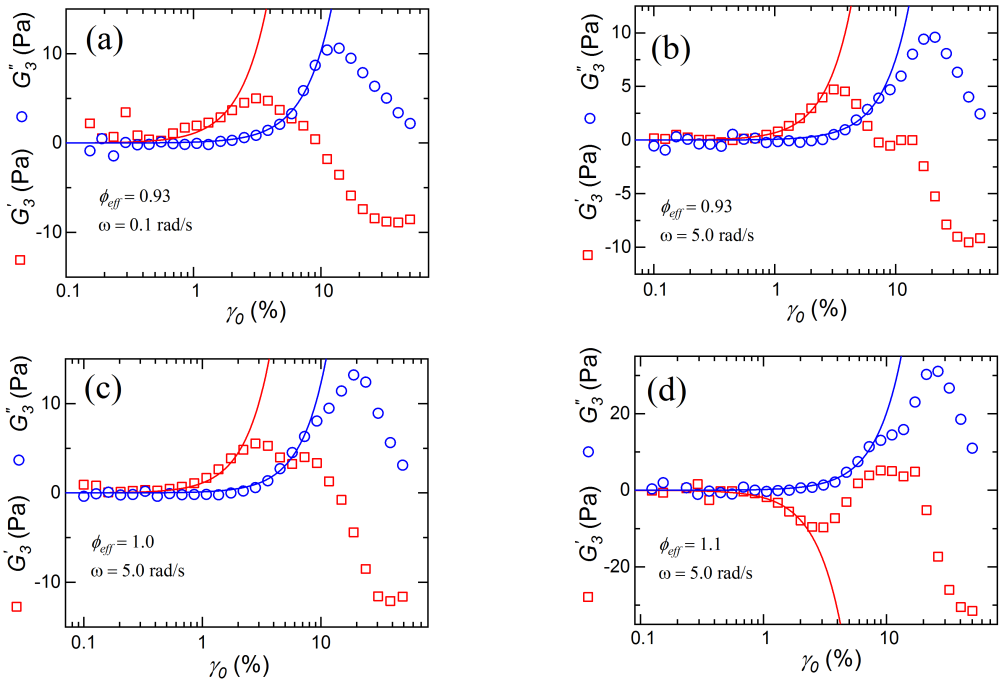

Figure 3.11: Fourier coefficients of the elastic and viscous moduli at the third harmonic (G_3' (□), G_3'' (○)) *vs.* strain amplitude γ_0 for suspensions of PNIPAM particles of PDI 11.6% measured at two different frequencies ω for different effective volume fractions ϕ_{eff}. The solid lines are fits to the equations: $G_3' = [G_3'(\omega)]\gamma_0^2$ (red solid lines) and $G_3'' = [G_3''(\omega)]\gamma_0^2$ (blue solid lines).

Medium amplitude oscillatory shear (MAOS) tests are performed for suspensions

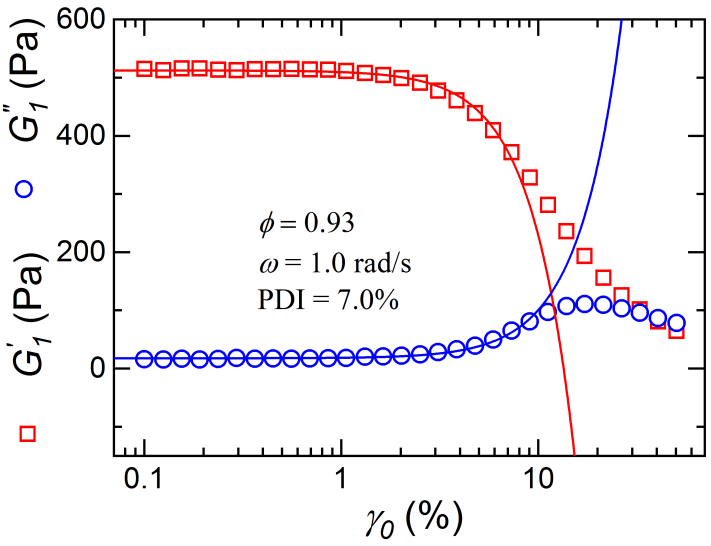

Figure 3.12: Fourier coefficients of the elastic and viscous moduli at the first harmonic (G_1' (□), G_1'' (○)) *vs.* strain amplitude γ_0 for suspensions of PNIPAM particles of polydispersity index (PDI) 11.6% measured at an angular frequency ω = 1.0 rad/s and for a sample of ϕ_{eff} = 0.93. The solid lines are fits to the equations: $G_1' = G_{eq}'(\omega) + [G_1'(\omega)]\gamma_0^2$ (red solid line) and $G_1'' = G_{eq}''(\omega) + [G_1''(\omega)]\gamma_0^2$ (blue solid line).

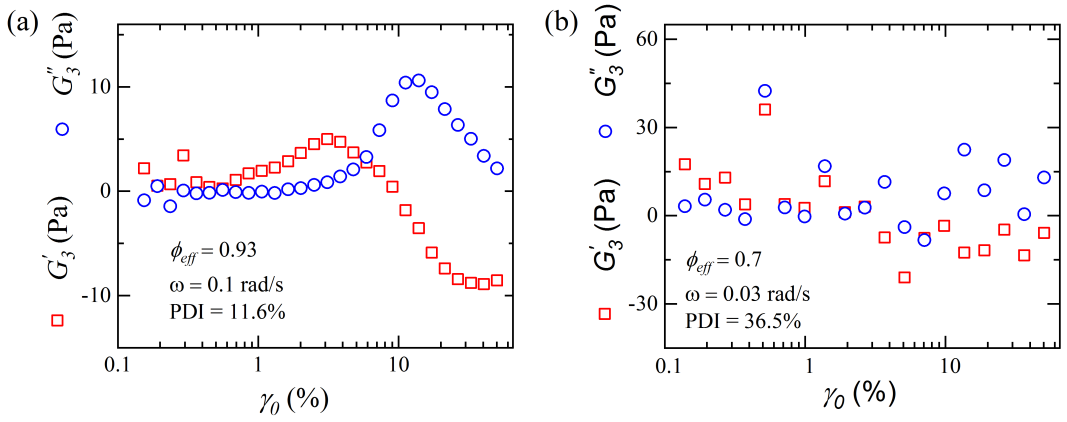

Figure 3.13: Fourier coefficients of the elastic and viscous moduli at the third harmonic (G_3' (□), G_3'' (○)) vs. strain amplitude γ_0 for suspensions of PNIPAM particles synthesized by (a) the OP method having polydispersity index (PDI) of 11.6% measured at an angular frequency ω = 0.1 rad/s and for ϕ_{eff} = 0.93 and by (b) the SB method having polydispersity index (PDI) of 36.5% measured at an angular frequency ω = 0.03 rad/s and for ϕ_{eff} = 0.7.

of PNIPAM particles of lower PDIs synthesized by the OP method. PNIPAM suspensions of different volume fractions near ϕ_0 are prepared using several different batches of particles. The Fourier coefficients of the elastic and viscous moduli at the third harmonic, $G_3'(\omega,\gamma_0)$ and $G_3''(\omega,\gamma_0)$, and at the fundamental harmonic, $G_1'(\omega,\gamma_0)$ and $G_1''(\omega,\gamma_0)$, are measured by varying the strain amplitude γ_0 between 0.1% to 50% at a fixed angular frequency ω. The intrinsic moduli $[G_3'(\omega)]$ and $[G_3''(\omega)]$ at a very low strain amplitude are determined by fitting the strain amplitude dependence of the Fourier coefficients of the elastic and viscous moduli at the third harmonic, $G_3'(\omega,\gamma_0)$ and $G_3''(\omega,\gamma_0)$, with quadratic functions, $G_3' = [G_3'(\omega)]\gamma_0^2$ and $G_3'' = [G_3''(\omega)]\gamma_0^2$ (figure 3.11) [29]. The frequency dependent equilibrium linear elastic and viscous moduli $G_{eq}'(\omega)$ and $G_{eq}''(\omega)$ are determined by fitting the strain amplitude dependence of the fundamental Fourier coefficients of the elastic and viscous moduli, $G_1'(\omega,\gamma_0)$ and $G_1''(\omega,\gamma_0)$, to the equations $G_1' = G_{eq}'(\omega) + [G_1'(\omega)]\gamma_0^2$ and $G_1'' = G_{eq}''(\omega) + [G_1''(\omega)]\gamma_0^2$ (figure 3.12). The intrinsic nonlinearity $Q_0(\omega)$ is obtained from the relation $Q_0(\omega) = \frac{|[G_3(\omega)]|}{|G_{eq}(\omega)|}$ [29]. Here, $|[G_3(\omega)]| = [[G_3'(\omega)]^2 + [G_3''(\omega)]^2]^{1/2}$ and $|G_{eq}(\omega)| = [[G_{eq}'(\omega)]^2 + [G_{eq}''(\omega)]^2]^{1/2}$ are the magnitudes of the intrinsic moduli at the third harmonic and the frequency dependent equilibrium linear complex modulus respectively.

We observe some difference in the quality of the G_3' and G_3'' data acquired from suspensions of PNIPAM particles synthesized by OP and SB methods at very low γ_0 (figure 3.13). It is difficult to determine the intrinsic parameters $[G_3'(\omega)]$ and $[G_3''(\omega)]$ for the highly polydisperse PNIPAM suspensions synthesized by the SB method due to the presence of large fluctuations in the G_3' and G_3'' values measured at very low γ_0 (figure 3.13(b)). These observed fluctuations arise from the extremely large distribution of particle sizes present in these highly polydisperse suspensions. Since the data from the suspensions of PNIPAM particles synthesized by the OP method are less noisy (figure 3.13(a)), we therefore use their aqueous suspensions to study the nonlinear Fourier transform rheology.

The nonlinear susceptibilities of glass forming liquids have been studied recently to

evaluate its dependence on the length scales of the dynamical heterogeneities [14, 51–54]. Moreover, the nonlinear rheological response of visco-elastic materials have been studied to understand material rigidity and its microscopic origin [28]. A recent report on soft PNIPAM core-shell particle suspensions showed the divergence of the mechanical nonlinear susceptibility at the third harmonic while approaching the glass transition [29]. In order to understand the heterogeneous behaviour and fragility of polydisperse PNIPAM suspensions, we record the mechanical nonlinear susceptibility arising at the third harmonic in the stress response of concentrated polydisperse PNIPAM suspensions using Fourier transform oscillatory rheology. To estimate the nonlinearity of these suspensions, we calculate the intrinsic nonlinearity Q_0, which is the ratio of the mechanical susceptibilities at the third harmonic with respect to the first harmonic at a very low strain amplitude γ_0. Q_0 is estimated as a function of angular frequency of the applied strain, ω, for PNIPAM suspensions synthesized by the OP method at several different ϕ_{eff} near ϕ_0 at a fixed PDI value and for several different PDIs at a fixed ϕ_{eff}. In these experiments, ω is varied between 0.005 rad/s and 10 rad/s.

In figures 3.14(a) and figure 3.14(b), Q_0 is plotted as a function of ω, normalized by the intrinsic relaxation frequency ($D_0/ < R_h >^2$) of a single particle, for dilute suspensions for PNIPAM suspensions at several different ϕ_{eff} at a fixed PDI and for several different PDIs at a fixed ϕ_{eff}, respectively. Q_0 exhibits a peak with increase in $\omega < R_h >^2 /D_0$ in both plots. It is seen from figure 3.14(a) that the peak height increases by half a decade and the peak position shifts to lower frequencies when ϕ_{eff} of PNIPAM suspensions is increased from 0.93 to 1.20 at a fixed particle PDI. The values of the peak heights and the peak positions at various ϕ_{eff} are plotted in the inset of figure 3.14(a). When the PDIs of the particles in these suspensions are increased from 7.4% to 16.2% at a fixed ϕ_{eff}, the peak height is observed to increase by a half a decade, while the peak positions shift to higher frequencies (figure 3.14(b)). The values of the peak positions and the peak heights *vs.* PDI are plotted in the inset of figure 3.14(b). The plots of Q_0, estimated as a function of $\omega < R_h >^2 /D_0$ for

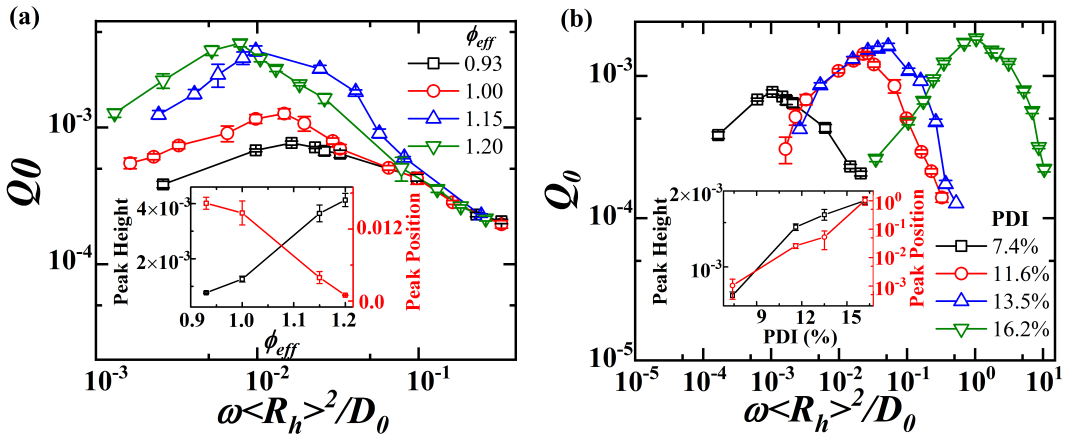

FIGURE 3.14: (a) Intrinsic nonlinearity Q_0 at the third harmonic *vs.* $\omega < R_h >^2 /D_0$ for suspensions of PNIPAM particles synthesized by the OP method for different ϕ_{eff} near ϕ_0 at a PDI = 11.6% at 25°C. Inset of (a) shows the peak height (□) and peak position (○) of $Q_0(\omega < R_h >^2 /D_0)$ curve *vs.* ϕ_{eff} of PNIPAM suspensions. (b) Intrinsic nonlinearity $Q_0(\omega)$ at the third harmonic *vs.* $\omega < R_h >^2 /D_0$ for suspensions of PNIPAM particles synthesized by OP method and characterized by different PDIs at a ϕ_{eff} = 1.0 at 25°C. Inset of (b) shows the peak height (□) and peak position (○) of $Q_0(\omega < R_h >^2 /D_0)$ curve *vs.* PDI of the PNIPAM particles in suspension. In this plot, the angular frequency ω is varied between 0.005 rad/s and 10 rad/s. For a dilute suspension of particles of mean radius $< R_h >$= 0.2 μm at 25°C, the self diffusion coefficient $D_0 = 1.23 \times 10^{-12}$ m^2/s.

PNIPAM suspensions of different ϕ_{eff} near ϕ_0 at a PDI = 11.6%, are seen to collapse at high frequencies (figure 3.14(a)). This observation indicates the presence of a single fast relaxation time in PNIPAM suspensions of different ϕ_{eff} values near ϕ_0 when the particle PDI is kept constant. However, in figure 3.14(b), the plots corresponding to different PDIs at fixed ϕ_{eff} are observed to have different shapes and therefore cannot be collapsed onto a master curve. This suggests the presence of different relaxation rates in the PNIPAM suspensions having different PDIs at a fixed ϕ_{eff}.

The observed increase in the peak heights with increase in ϕ_{eff} at a fixed PDI (inset of figure 3.14(a)) and with increase in PDI at a fixed ϕ_{eff} (inset of figure 3.14(b)) confirms an increase in the intrinsic nonlinearity of the suspensions when the relevant control parameter (ϕ_{eff} or PDI) is changed. This can be interpreted in terms of increasingly heterogeneous dynamics which is also apparent from the fragility measurements reported in figure 3.9. In general, for a jammed suspension characterized by higher particle PDIs, the dynamics of small particles decouple from the dynamics

of big particles, which leads to a broadening of the relaxation spectra of the particles. As a consequence, due to the cooperative rearrangements of these polydisperse particles in the jammed suspension, the distribution of relaxation time scales widens. This is expected to increase the nonlinearity in the mechanical responses of the jammed suspensions of higher particle PDIs.

Furthermore, the shift of the peak position to a higher frequency with increase in particle PDI indicates a decrease in the structural relaxation times (inset of figure 3.14(b)) of the particles in aqueous suspension. This can be explained by considering that the smaller particles in the highly polydisperse suspensions still remain free to diffuse even at very high volume fractions. This results in the emergence of an arrested state at larger particle concentrations when compared to suspensions having particles of smaller PDIs. From the nonlinear rheology results shown in figures 3.14(a) and 3.14(b), we can therefore separate the effects of changes in ϕ_{eff} and PDI on the glass transition of PNIPAM suspensions. Increase in ϕ_{eff} at a fixed PDI accelerates the jamming of PNIPAM particles in suspension, while increase in PDI at a fixed ϕ_{eff} fluidizes the jammed state of PNIPAM suspensions.

3.4 Conclusions

We have synthesized thermoresponsive PNIPAM particles of a wide range of polydispersity indices (PDIs) using the one-pot and semi-batch synthesis methods. The thermoresponsive behaviour and the size distributions of these particles are characterized by DLS and SEM. A rheological study of the approach of these suspensions towards the glass transition shows that the soft and polydisperse PNIPAM particles form highly fragile glasses at volume fractions well above the random close packing volume fraction ϕ_{rcp} of monodisperse hard sphere colloidal suspensions. The nonlinear stress response at the third harmonic to applied oscillatory strains is measured to quantify the intrinsic nonlinearity of these samples. The intrinsic nonlinearity of these suspensions is monitored by changing ϕ_{eff} at a fixed PDI and by changing particle

PDIs at a fixed ϕ_{eff}. The nonlinearity of the dynamics of these suspensions is observed to increase with increase in both ϕ_{eff} and PDI. The increase in fragility, $1/D$, and ϕ_0 of these concentrated suspensions with increase in particle PDI is supported by our nonlinear rheology results. In jammed suspensions of polydisperse particles, the increase in nonlinearity in mechanical responses strongly affects the cooperative structural relaxation processes. This involves more particles showing correlated movement during the structural relaxation which makes the dynamics more heterogeneous. For a jammed packing of polydisperse particles, the local packing fraction, the number of contacts and the number of neighbours surrounding a given particle are the parameters that decide the packing efficiency at the single particle level. All these parameters are expected to increase with increase in ϕ_{eff}, PDI and the particle softness, thereby enhancing the packing efficiency of the soft and deformable PNIPAM particles. Suspensions of PNIPAM particles are therefore excellent candidates for studying the dynamics of highly polydisperse particles in soft glassy suspensions.

References

[1] M. Heskins and J. E. Guillet, *J. Macromol SCi.*, 1968, **2**, 1441.

[2] Y. Hirokawa and T. Tanaka, *J. Chem. Phys.*, 1984, **81**, 6379.

[3] J. Wu, G. Huang and Z. Hu, *Macromolecules*, 2003, **36**, 440-448.

[4] J. Appel, B. Folker and J. Sprakel, *Soft Matter*, 2016, **12**, 2515.

[5] L. Dong and A. S. Hoffman, *J. Controlled. Release*, 1991, **15**, 141.

[6] A. S. Hoffman, *The Journal of Physical Chemistry B*, 2000, **46**, 1478.

[7] G. Zhang, N. Yang, Y. Ni, J. Shen, W. Zhao and X. Huang, *Sensors and Actuators B: Chemical.*, 2011, **158**, 130.

[8] G. E. Morris, B. Vincent and M. J. Snowden, *J Colloid Interface Sci*, 1997, **190**, 198.

[9] H. Q. Sun, L. Zhang, Z. Q. Li, L. Zhang, L. Luo and S. Zhao, *Soft Matter*, 2011, **7**, 7601.

[10] P. N. Pusey and W. Van Megen, *Phys. Rev. Lett.*, 1987, **59**, 2083.

[11] E. R. Weeks, J. C. Crocker, A. C. Levitt, A. Schofield and D. A. Weitz, *Science*, 2000, **287**, 627.

[12] W. Schaertl and H. Sillescu, *J. Stat. Phys.*, 1994, **77**,1007.

[13] C. A. Angell, *J. Non-Crystalline Solids*, 1991, **131**, 13.

[14] G. Brambilla, D. El Masri, M. Pierno, L. Berthier, L. Cipelletti, G. Petekidis and A. B. Schofield, *Phys. Rev. Lett.*, 2009, **102**, 085703.

[15] P. N. Pusey and W. Van Megen, *Nature*, 1986, **320**, 340.

[16] J. Mattsson, H. M. Wyss, A. Fernandez-Nieves, K. Miyazaki, Z. Hu, D. R. Reichman and D. A. Weitz, *Nature*, 2009, **462**, 83.

[17] C. A. Angell, *Science*, 1995, **267**, 1924.

[18] M. Suzuki, H. Sato, M. Hasegawa and M. Hirota, *Powder Technol.*, 2011, **118**, 53.

[19] M. Rubinstein and R. H. Colby, *J. Chem. Phys.*, 1988, **89**, 5291.

[20] R. Basak, N. Mukhopadhyay and R. Bandyopadhyay, *Eur. Phys. J. E*, 2011, **34**, 103.

[21] P. Yunker, Z. Zhang and A. G. Yodh, *Phys. Rev. Lett.*, 2010, **104**, 015701.

[22] J. Hendricks, R. Capellmann, A. B. Schofield, S. U. Egelhaaf and M. Laurati *Phys. Rev. E*, 2015, **91**, 032308.

[23] T. Sentjabrskaja, E. Babaliari, J. Hendricks, M. Laurati, G. Petekidis and S. U. Egelhaaf, *Soft Matter*, 2013, **9**, 4524.

[24] E. Zaccarelli, S. M. Liddle and W. C. K. Poon, *Soft Matter*, 2015, **11**, 324.

[25] P. Sollich and N. B. Wilding, *Soft Matter*, 2011, **7**, 4472.

[26] R. S. Farr and R. D. Groot, *J. Chem. Phys.*, 2009, **131**, 244104.

[27] S. E. Abraham and B. Bagchi, *Phys. Rev. E.*, 2008, **78**, 051501.

[28] K. Hyun and M. Wilhelm, *Macromolecules*, 2009, **42**, 411.

[29] R. Seyboldt, D. Merger, F. Coupette, M. Siebenbürger, M. Ballauff, M. Wilhelmc and Matthias Fuchs, *Soft Matter*, 2016, **12**, 8825.

[30] T. Still, K. Chen, A. M. Alsayed, K. V. Aptowicz and A. G. Yodh, *J. Colloid and Interface Science*, 2013, **405**, 96.

[31] W. McPhee, K. C. Tam and R. Pelton, *J. Colloid and Interface Science*, 1993, **156**, 24.

[32] A. Yang, C.T. Miller and L.D. Turcoliver, *Phys. Rev. E*, 1996, **53**, 1516.

[33] M. Cross, *J. Colloid Sci.*, 1965, **20**, 417.

[34] F. D. Lorenzo and S. Seiffert, *Macromolecules*, 2013, **46**, 1962.

[35] G. K. Batchelor, *J. Fluid Mech.*, 1997, **83**, 97.

[36] J. F. Brady and M. Vicic, *J. Rheology*, 2014, **39**, 545.

[37] W. C. K. Poon, Colloidal Suspensions, Clarendon Press, Oxford U. P., 2012.

[38] C. P. Lindsey and G. D. Patterson, *J. Chem. Phys.*, 1980, **73**, 3348.

[39] P. N. Segre and P. N. Pusey, *Phys. Rev. Lett.*, 1996, **77**, 771.

[40] D. E. Koppel, *J. Chem. Phys.*, 1972, **57**, 4814.

[41] X. Xia and Z. Hu, *Langmuir*, 2004, **20**, 2094.

[42] G. L. Hunter and E. R. Weeks, *Rep. Prog. Phys.*, 2012, **75**, 66501.

[43] W. Van Megen and S. M. Underwood, *Phys. Rev. Lett.*, 1993, **70**, 2766.

[44] S. P. Meeker, W. C. K. Poon and P. N. Pusey, *Phys. Rev. E.*, 1997, **55**, 5718.

[45] S. E. Phan, W. B. Russel, Z. Cheng, J. Zhu, P. M. Chaikin, J. H. Dunsmuir and R. H. Ottewill, *Phys. Rev. E.*, 1996, **54**, 6633.

[46] H. Tanaka, *Phys. Rev. Lett.*, 2003, **90**, 0055701.

[47] B. R. Saunders, *Langmuir*, 2004, **20**, 3925.

[48] R. H. Pelton, H. M. Pelton, A. Morphesis and R. L. Rowell, *Langmuir*, 1989, **5**, 816.

[49] D. He, N. N. Ekere and L. Cai, *Phys. Rev. E.*, 1999, **60**, 7098.

[50] N. Kiriushcheva and P. H. Poole, *Phys. Rev. E.*, 2001, **65**, 011402.

[51] M. Tarzia, G. Biroli, A. Lefèvre and and J.-P. Bouchaud, *J. Chem. Phys.*, 2010, **132**, 054501.

[52] C. Crauste-Thibierge, C. Brun, F. Ladieu, D. L'Hôte, G. Biroli and J.-P. Bouchaud, *Phys. Rev. Lett.*, 2010, **104**, 165703.

[53] F. Ladieu, C. Brun and D. L'Hôte, *Physical Review B*, 2012, **85**, 184207.

[54] P. Gadige, D. Saha, S. K. Behera and R. Bandyopadhyay, *Scientific Reports*, 2017, **7**, 8017.

4

Study of microscopic dynamics of a polydisperse colloidal suspension approaching kinetic arrest.

4.1 Introduction

The kinetically arrested state in supercooled liquids or colloidal suspensions can be achieved, respectively, by rapidly decreasing the temperature, T, or increasing the particle volume fraction, ϕ [1, 2]. Colloidal suspensions have been used as model glass formers as their size range (nm - μm) and relaxation time scales (μs - s) are accessible by experimental techniques such as bright field and confocal microscopy, dynamic light scattering, etc. [3]. The viscosities and relaxation times of hard sphere colloidal

suspensions grow by orders of magnitude for a very small increase in volume fraction near the jamming transition volume fraction ϕ_g [4–7]. This dramatic increase of viscosities and relaxation times near ϕ_g is due to the slowing down of the particle dynamics which reflects the confinement of any given particle by a cage formed by its neighbors [1, 8, 9]. At longer time scales, the cages rearrange due to the cooperative motion of neighboring particles. This leads to the structural relaxation of the sample, allowing the particle to diffuse out of its cage [1, 10]. In order to achieve kinetic arrest in colloidal suspensions, it has been reported that increasing the volume fraction ϕ by fixing PDI in a colloidal suspension is analogous to decreasing PDI by fixing ϕ [3]. Thus, the exploration of dense colloidal suspensions, composed of particles of different PDIs, can explain the effects of PDI on the caging dynamics of these suspensions approaching kinetic arrest.

The caging dynamics in dense colloidal suspensions near the glass transition volume fraction has been studied extensively [9, 11, 12]. An understanding of the cage trapping and breaking phenomena occurring at the glass transition is very important in explaining the structural relaxation time scales and rapid growth of viscosity in dense suspensions [3, 11]. It is reported that the sizes of the cages shrink and the cage lifetimes grow as the glass transition is approached [9]. The cages become more compact with increase in particle volume fraction, with the rearrangements of cages happening at longer times. The structural relaxation time and viscosity of the colloidal suspension therefore increase with increase in volume fraction. In addition to particle volume fraction, the caging behavior of a dense colloidal suspension is sensitive to particle stiffness, interparticle interactions and particle size polydispersity [13–15]. The effects of particle stiffness and interparticle interactions on the caging behavior are reported in the literature [13, 14]. It has been observed that soft particles in a dense suspension are more strongly caged when compared to stiff particles [13]. The caging behavior of attractive and repulsive colloidal glasses are different from each other. Colloidal glasses formed by attractive interparticle interactions are reported to have more heterogeneous dynamics during the cage rearrangement process [14]. Due to our incomplete

understanding of the effects of particle size polydispersity on the caging behaviour of a colloidal suspension, a systematic study of the connection between particle size polydispersity and the caging properties in colloidal suspensions approaching kinetic arrest is essential in understanding the sample dynamics close to the jamming point.

In this work, fluorescent PNIPAM particles characterized by a range of particle PDIs are synthesized by varying the flow rate of the reaction ingredients in a semi-batch method [16]. The dynamics of the particles in suspension as they approach kinetic arrest is studied using confocal microscopy. The evolution of the dynamics of these particles with time is observed from the mean square displacement (MSD) plots obtained as a function of time by confocal video tracking of the particles. MSD *vs*. time plots for suspensions of PNIPAM particles show that the particles motion changes from diffusive to sub-diffusive with increase in area fraction, while the opposite happens in a colloidal suspension when PDI of the particles in suspension is increased. Moreover, caging behavior becomes weaker and slowly disappears with the increase in particle PDI. Our measurements provide interesting insights into the effects of the width of the particle size distribution and particle area fraction on the caging behavior of disordered materials approaching the dynamically arrested state.

4.2 Sample preparation

Fluorescent PNIPAM particles are prepared by incorporating functionalized fluorescein dye in the polymer network in a semi-batch method. The details of the preparation method of functionalized fluorescein is described in the section 2.2.1 of chapter 2. The polydispersity of the fluorescent PNIPAM particles is controlled by varying the flow rates of the reaction ingredients in the semi-batch method described in the same section. In a typical experiment, 2.0 g *N*-isopropylacrylamide (NIPAM) (≥ 99%), 0.05 g *N,N'*-methylenebisacrylamide (MBA) (≥ 99.5%), 8.3 mg of 2-aminoethylmethacylate hydrochloride (AEMA) and 0.1 g of flunctionalized fluorescein are dissolved in 50 mL of Milli-Q water (Millipore Corp.) in a three-necked round-bottomed (RB) flask fitted

with a reflux condenser, a temperature sensor and a N_2 inlet/outlet. PNIPAM particles of different sizes and size distributions are synthesized by varying the feeding rates of reaction ingredients (the monomer, crosslinker, fluorescein and AEMA solutions). The three-necked RB flask is placed inside a heat bath in contact with the hot plate of the magnetic stirrer. The solution is stirred at 600 rpm for 20 min and also purged with nitrogen (N_2) gas for 20 min. 30 mL of this solution is taken out in a syringe and 10 mL of water is added to the remaining 20 mL of solution present in the flask. The temperature of the heat bath is raised to 80°C and the bath is purged with N_2 gas for 20 min. The free radical precipitation polymerization reaction is initiated by the addition of 11.4 mg ammonium persulfate (APS) dissolved in 2 mL of water. Primary nucleation sites start to form after about 5 min, following which the solution present in the syringe is fed into the reaction vessel at constant flow rates using a syringe pump (Chemyx Inc.). The reaction is stopped 5 min after all the ingredients are added. The latices are cooled down rapidly in an ice bath. The preparation of the latex recipes is summarized in table 4.1.

Water (mL)	NIPAM (g)	MBA (g)	APS (mg)	AEMA (mg)	Flow rate (ml/min)	$< d_{25^\circ C} >$ (μm)	PDI (%)
60	2	0.05	11.4	8.3	1.0	1.22	8.36
60	2	0.05	11.4	8.3	0.9	0.86	12.48
60	2	0.05	11.4	8.3	0.7	0.63	23.25
60	2	0.05	11.4	8.3	0.5	1.27	35.77
60	2	0.05	11.4	8.3	0.3	0.95	40.38

Table 4.1: Summary of synthesis conditions for preparing suspensions of PNIPAM particles of various sizes and PDIs by a semi-batch method. The particles are synthesized at 80°C by varying the flow rates of the reaction ingredients. The mean particle size at 25°C ($< d_{25^\circ C} >$) and the polydispersity index (PDI), estimated for approximately 2000 particles, are reported.

4.2.1 Preparation of aqueous suspensions of fluorescent PNIPAM particles and measurement of their zeta potential:

Fluorescent PNIPAM latices obtained from the reaction are purified by four successive centrifugations, decantations and redispersions in Milli-Q water to remove unwanted fluorescent compounds and the remaining monomers, oligomers and impurities. Centrifugation is performed at a speed of 10,000 rpm for 60 min. Dense fluorescent PNIPAM suspensions are obtained by removing all the supernatant from the residue. Fluorescent PNIPAM suspensions of very high concentrations are prepared by adding Milli-Q water in the residue of PNIPAM suspensions obtained after centrifugation. The suspension is then stirred overnight and sonicated for 15 min. PNIPAM suspensions of different concentrations are prepared by diluting suspensions of the highest PNIPAM particle concentration with Milli-Q water.

The zeta potentials (ζ) of these suspensions are measured using an electroacoustic probe (DT-1200) described in section 2.3.4 of chapter 2. The ζ values estimated for suspensions of PNIPAM particles of PDI=23.25% at different concentrations are listed in table 4.2. The positive ζ values of these suspensions (table 4.2) confirm the presence of repulsive electrostatic interactions among the PNIPAM colloidal particles.

Concentration (wt%)	ζ (mV)
1.0	28.16
5.0	13.8
10.0	7.08

Table 4.2: Zeta potential of fluorescent PNIPAM suspensions of PDI=23.25% measured for different concentrations at 25°C.

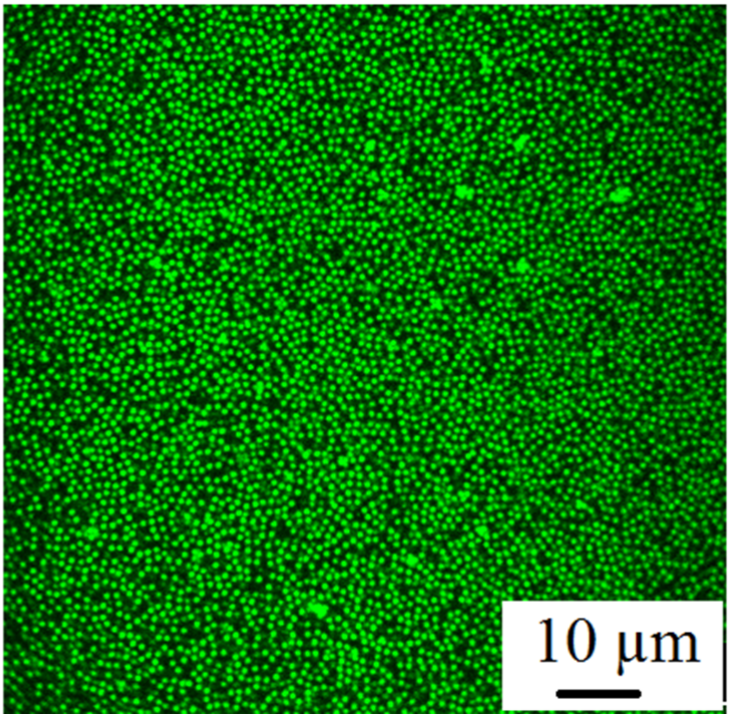

Figure 4.1: Confocal microscopy image of a suspension of fluorescent PNIPAM particles of PDI = 23.25% at an area fraction 0.66 at 25°C. The scale bar shown in the image is 10 μm.

4.3 Confocal microscopy imaging and Particle tracking:

Two dimensional confocal microscopy images are acquired using a Leica TCS SP8 confocal microscope system, with a 100x Nikon plain oil immersion objective (NA = 1.40) described in the section 2.3.5 of chapter 2. The details of the sample cell and sample preparation for confocal microscope imaging of PNIPAM particles are described in the same section. Figure 4.1 shows the representative two dimensional confocal microscopy image of a suspension of PNIPAM particles of PDI = 23.25% at an area fraction of 0.66. PNIPAM particles are tracked using a video spot tracker software developed by Computer Integrated Systems for Microscopy and Manipulation (CISMM). In this software, a green channel is selected for tracking the green PNIPAM particles. A disc kernel, with radius of the disc equal to the radius of the particle,

is suitable for tracking this type of particles. The threshold value of the intensity for tracking the particle is automatically decided by the software. The x and y coordinates of the centroid of the particles are linked from one image to the next to form trajectories which are used to compute mean square displacements of the particles.

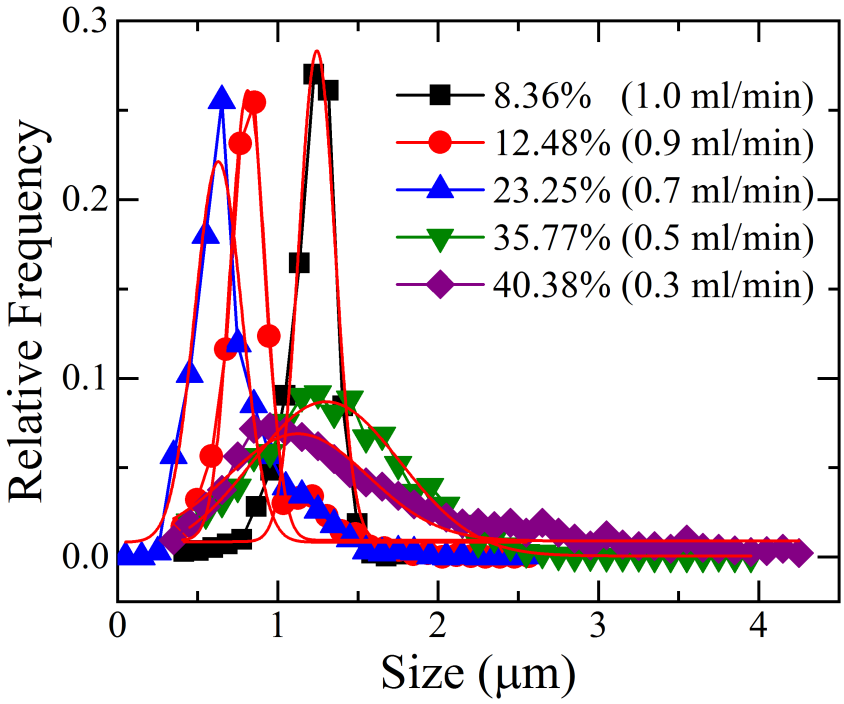

Figure 4.2: Particle size distributions calculated from confocal images for PNIPAM particles of different PDIs synthesized by the semi-batch method at different flow rates (ml/min) of the reaction ingredients. The red solid lines are fits to the Gaussian function.

4.4 Estimation of Area fraction and PDI:

The area fractions $\phi = A_p/A_T$ of samples prepared at different concentrations are calculated by counting the pixels occupied by the particles in the two-dimensional confocal images. Here A_p is the total pixel area occupied by the particles and A_T is the total pixel area of the field of view. The area fractions of these samples are estimated from

3 confocal images taken from different regions of the samples. The average particle sizes and size distributions of these particles in aqueous suspensions are estimated for approximately 2000 particles using the ImageJ software. The particle size distributions obtained from the confocal image analyses can be described by Gaussian distributions. The ratio of the standard deviation of the particle size and the mean particle size of the Gaussian distribution measures the polydisperity index (PDI) of the particles in the suspension. PDIs measured for PNIPAM suspensions synthesized for different flow rates in the semi-batch method are listed in table 4.1 and the corresponding particle size distributions are plotted in figure 4.2.

4.5 Results and discussion

The mean square displacements $< \Delta r^2(\Delta t) > = < \frac{1}{n} \sum_{i=1}^{n} \Delta r_i^2(\Delta t) >$ of PNIPAM particles at a lag time Δt is calculated from the x, y position coordinates of the centroids of these particles obtained by tracking over approximately 140 successive frames. Here, $\Delta r_i^2(\Delta t) = \Delta x_i^2(\Delta t) + \Delta y_i^2(\Delta t)$ is the square displacement of a particle during the ith step corresponding to a stepping time Δt. In the above expression, $\Delta x_i(\Delta t)$ and $\Delta y_i(\Delta t)$ are, respectively, the x and y displacements of a particle during the i th step, n is the number of steps with a stepping time Δt and <> indicates the average over all particles in the observation volume for a lag time Δt. In order to study the motion of PNIPAM particles in a suspension approaching kinetic arrest, we have plotted the mean square displacement $< \Delta r^2(\Delta t) >$ of the particles as a function of lag time Δt in figure 4.3 for several different area fractions ϕ of the suspension with particles of PDI = 23.25%. It is seen that the MSD values of the particles decrease with increase in particle area fraction. This indicates that the particle motion slows down with increase in area fraction due to the increase in confinement of the particles by their neighbors [9, 12]. Moreover, a plateau in the MSD curve appears when the area fraction of the particle is increased above a certain value (figure 4.3). At $\phi = 0.72$, the plateau in the MSD curve indicates the trapping of a particle inside a cage, which arrests the

particle motion [11, 17]. At longer times, we see cage breaking due to cooperative diffusion. As time progresses, the cages rearrange which allows the particle to move to a new cage. This results in an increase in the MSD of the particles at longer times. During the rearrangement of the cages, the particles move cooperatively. The time scale associated with this process is called the structural or α relaxation time [1, 8]. The time at which the upturn in the MSD curve appears can be roughly related with the average α relaxation time scale of the particle [11]. When the area fraction of the PNIPAM suspension is decreased below 0.72, the plateau in the $< \Delta r^2(\Delta t) >$ *vs.* Δt curve disappears. This shows the absence of caged motion of the particles for $\phi < 0.72$ (figure 4.3).

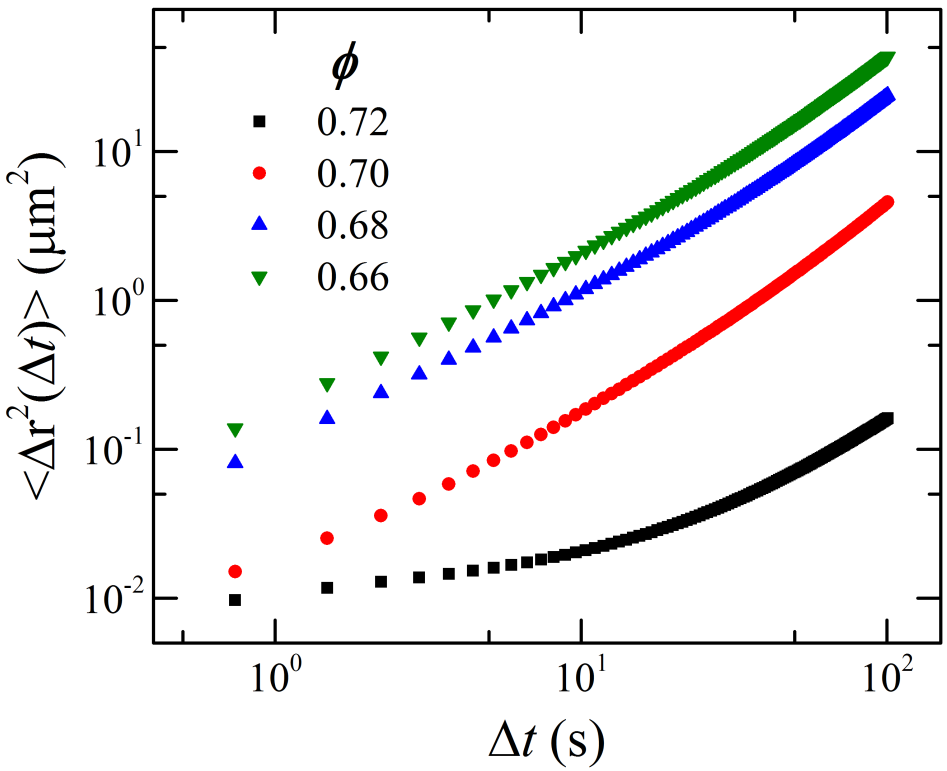

Figure 4.3: Mean square displacement $< \Delta r^2(\Delta t) >$ of the particles, is plotted against lag time, Δt for PNIPAM suspensions of different area fractions ϕ at a fixed PDI = 23.25%.

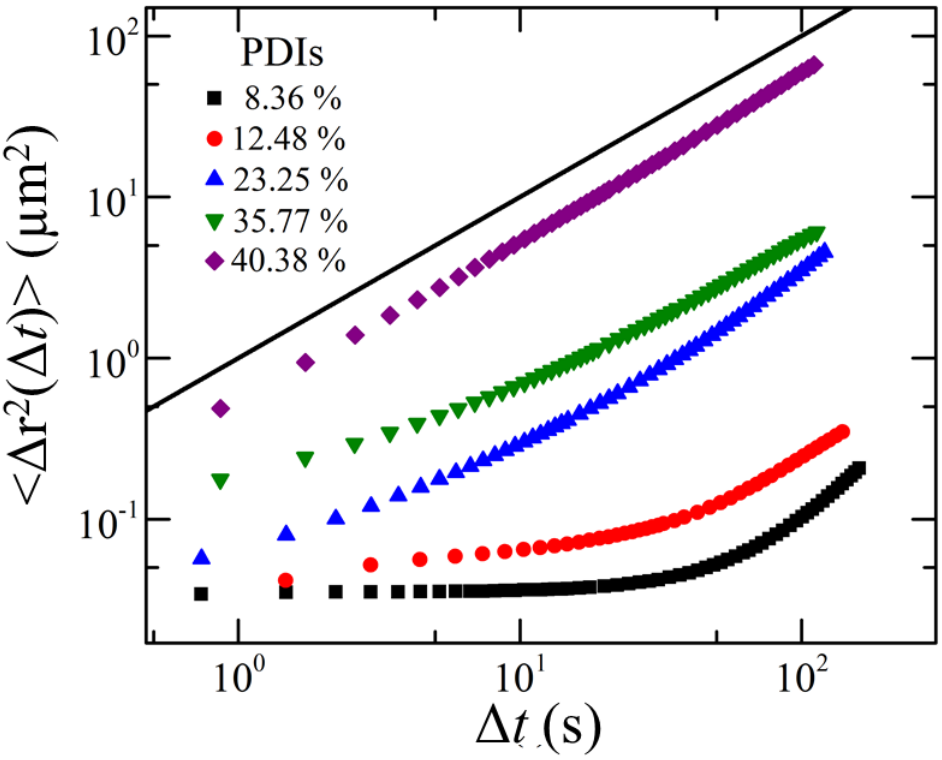

Figure 4.4: Mean square displacement $< \Delta r^2(\Delta t) >$ of the particles, is plotted against lag time, Δt for PNIPAM suspensions of different PDIs at a fixed area fraction $\phi = 0.7$. The solid line in this plot is a line with unit slope.

To study the effects of particle size polydispersity on the caging dynamics of PNIPAM suspensions, we have plotted the MSD curves as a function of time for suspensions of particles of different PDIs at a fixed area fraction (figure 4.4). It is seen that the MSD of the particles increases with increase in PDI. This suggests that the motion of the particle in a suspension speeds up with increase in PDI. The MSD curves for the suspensions constituted by particles of lower PDIs (8.36% and 12.48%) show a plateau at low Δt values, which is followed by an increase with Δt at longer times (figure 4.4). As mentioned earlier, the presence of a plateau at initial times in these MSD curves indicates the caging behavior of the particles in these suspensions. As time progresses, the particles move cooperatively due to the rearrangement of cages [8, 9]. The plateau

value of the MSD curve is related to the size of the cage [9]. The plateau mean square displacement value decreases as the PDI decreases, reflecting the decrease in cage size with decrease in particle PDI (figure 4.4). The plateaus in the $< \Delta r^2(\Delta t) > vs.\ \Delta t$ plot slowly disappear with increase in PDI (23.25% and 35.77%) (figure 4.4). For a suspension having a sufficiently high PDI (40.38%), we note that the dynamics are diffusive ($< \Delta r^2(\Delta t) > \propto \Delta t$) even at the lowest accessible values of Δt (figure 4.4). The diffusive behavior of the particles in this suspension is verified by comparing its MSD curve with a line of unit slope (shown by a solid line in figure 4.4). The above observation confirms that the caging behaviour becomes weak with increase in PDI in dense aqueous suspensions of PNIPAM particles.

4.6 Conclusions

This chapter reports particle-scale experiments that demonstrate that the caging behavior of an aqueous polydisperse PNIPAM colloidal suspension approaching kinetic arrest is influenced by the particle size distribution of colloidal particles. The evolution of mean square displacement (MSD) of the particles with time in these dense suspensions, characterized by a range of particle PDIs, shows that the caging behaviour becomes weak and the cage-breaking phenomenon occur at earlier times with increase in particle PDIs. However, the caging behavior becomes strong when the area fraction of the particles is increased. The increase in particle size polydispersity therefore has an opposite effect to the increase in area fraction of the particles in the caging dynamics of a suspension. The faster dynamics of the smaller particles in suspensions of higher polydispersity facilitates the cage rearrangements and thereby reduces the cage-breaking time scales in these suspensions.

In this work, the caging behavior of PNIPAM suspension is monitored by changing the area fraction at a fixed PDI and by changing particle PDIs at a fixed area fraction. The sizes of the cages formed by the particles in these suspension increase with increase in PDI and decrease with increase in area fraction, while the cage rearrangement

time scales decrease with increase in PDI or decrease in area fraction. In polydisperse colloidal suspensions, smaller particles relax faster than the larger particles, which accelerates the suspension dynamics. The experiments reported here measure the average dynamics of the particles in suspension. Furthermore, the population of the particles corresponding to a particular size can also affect the caging dynamics in suspensions of polydisperse particles. The study of the effects of particle polydispersity on the dynamics of dense suspensions is therefore a challenging problem that needs to be addressed in more detailed experiments.

References

[1] M. D. Ediger, C. A. Angel and S. R. Nagel *J. Phys. Chem.*, 1996, **100**, 13200-13212.

[2] S. K. Behera, D. Saha, P. Gadige and R. Bandyopadhyay, *Phys. Rev. Materials*, 2017, **1**, 055603.

[3] G. L. Hunter and E. R. Weeks, *Rep. Prog. Phys.*, 2012, **75**, 066501.

[4] L. Marshall and C. F. Zukoski, *J. Phys. Chem.*, 1990, **94**, 71-1164.

[5] G. Brambilla, D. El Masri, M. Pierno, L. Berthier, L. Cipelletti, G. Petekidis and A. B. Schofield, *Phys. Rev. Lett.*, 2009, **102**, 085703.

[6] Z. Cheng, J. Zhu, P. M. Chaikin, S. E. Phan and W. B. Russel, *Phys. Rev. E*, 2002, **65**, 041405.

[7] S. E. Phan, W. B. Russel, Z. Cheng, J. Zhu, P. M. Chaikin, J. H. Dunsmuir and R. H. Ottewill, *Phys. Rev. E*, 1996, **54**, 45-6633.

[8] C. A. Angell, *J. Phys. Condens. Matter*, 2000, **12**, 6463.

[9] E. R. Weeks and D. A. Weitz, *Phys. Rev. Lett.*, 2002, **89**, 095704.

[10] C. A. Angell, *Science*, 1995, **267**, 35-1924.

[11] E. R. Weeks, J. C. Crocker, A. C. Levitt, A. Schofield and D. A. Weitz, *Science*, 2000, **287**, 627.

[12] T. Narumi, S. V. Franklin, K. W. Desmond, M. Tokuyama and E. R. Weeks, *Soft Matter*, 2011, **7**, 1472.

[13] Y. Rahmani, K. van der Vaart, B. van Dam, Z. Hu, V. Chikkadia and P. Schall, *Soft Matter*, 2012, **8**, 4264.

[14] Z. Zhang, P. J. Yunker, P. Habdas and A. G. Yodh, *Phys. Rev. Lett.*, 2011, **107**, 208303.

[15] P. Yunker, Z. Zhang and A. G. Yodh, *Phys. Rev. Lett.*, 2010, **104**, 015701.

[16] T. Still, K. Chen, A. M. Alsayed, K. V. Aptowicz and A. G. Yodh, *J. Colloid and Interface Science*, 2013, **405**, 96.

[17] K. V. Edmonda, M. T. Elsesserb, G. L. Huntera, D. J. Pineb and E. R. Weeks, *PNAS*, 2012, **109**, 1789117896.

5

Temperature and stiffness induced phase changes in dense aqueous suspensions of thermoresponsive poly(*N*-isopropylacrylamide) colloidal particles

5.1 Introduction

The complex phase behavior and jamming dynamics of dense suspensions of soft poly(*N*-isopropylacrylamide) (PNIPAM) colloidal particles have been widely investigated [1–5]. These particles are thermoresponsive and, when suspended in water, can swell or deswell in response to changes in temperature. The particle volume fraction in an aqueous medium can therefore be controlled by changing the suspension temperature without changing the particle number density [6, 7]. This property has been exploited in several experiments to tune the dynamics and assembly of PNIPAM suspensions [8–10]. A decrease in the temperature of aqueous suspensions of PNIPAM particles below the lower critical solution temperature (LCST) of $T \approx 35°\mathrm{C}$ causes the particles to swell significantly. Controlling the temperature and concentration of a PNIPAM suspension can therefore lead to a jammed suspension, widely regarded as an excellent experimental model system to study the kinetic arrest phenomenon in dense colloidal suspensions [11]. Due to their physicochemical flexibility, PNIPAM particles have been considered as candidates for drug delivery in the human body and in the production of strong gels that could potentially enable the design of soft biomimetic machines [12, 13]. The compressive and tensile stresses of poly(acrylamide) nanocomposite hydrogels, characterised by homogeneous network structures that are reinforced by calcium hydroxide nano-spherulites and the crosslinking of N,N'-methylenebisacrylamide clusters [14], are of the order of mega-Pascals. Considering their mechanical robustness and thermoresponsivity, these suspensions can be used as multifunctional materials in biomedical engineering applications [13, 15].

The microscopic structure, rheology and phase behavior of PNIPAM suspensions can be altered by changing the chemistry of the PNIPAM particles [16]. A chemical property that can be controlled fairly easily is the particle stiffness [2, 17]. During particle synthesis, the ratio of the concentrations of the crosslinker (N,N'-methylenebisacrylamide) and the monomer (*N*-isopropylacrylamide) fixes the number of cross linking points and therefore the stiffness of the PNIPAM particles [18, 19]. Stiff PNIPAM

particles suspended in water undergo transitions from a liquid to a crystal to a glass when the particle volume fraction is increased, while suspensions of particles of intermediate stiffnesses transform from a liquid to a glass without going through an intermediate crystalline phase [2]. Suspensions of soft particles, in contrast, remain in the liquid phase for the entire range of volume fractions explored in [2]. The mechanical properties of PNIPAM suspensions were reported to be affected by the stiffnesses of the constituent particles, with the elastic modulus and yield stress depending upon the crosslinking density of the particles [19]. A higher crosslinking density leads to a higher interparticle force and a higher plateau value of the elastic modulus, whereas the easy inter-penetration of the dangling polymer chains on the surfaces of particles with lower crosslinking densities results in higher yield stresses. In another study, it was reported that the crystalline packing of PNIPAM particles in aqueous suspension is not affected by the particle softness, with the colloidal assemblies exhibiting remarkable self-healing properties [17].

The phase behavior of dense PNIPAM suspensions is also sensitive to changes in temperature. It has been reported that an increase in temperature shifts the dynamically arrested states of the suspensions (colloidal crystals and glasses) to higher volume fractions [8]. Zhao *et al.* reported a gel to sol transition in concentrated PNIPAM microgel suspensions when the temperature was increased across the LCST [20]. In another study on the temperature dependence of hydrogel suspensions, Romeo *et al.* observed that the low-temperature glassy state in temperature- and pH-responsive p-NIPA suspensions liquefies at the LCST, before solidifying into a gel-like state when the temperature is increased further [1]. These observations were understood by considering that the interparticle interaction in these aqueous suspensions switches from repulsive to attractive across the LCST [1, 21].

A systematic study of the effects of temperature and stiffness on the mechanical behavior and structure of dense suspensions of PNIPAM particles is essential to understand the complex phase behavior of their dense suspensions. In this chapter, we report the temperature and stiffness induced changes in the mechanical properties and phase

behavior of PNIPAM particles in very dense aqueous suspensions. PNIPAM particles of different stiffnesses are synthesized by varying the concentration of the crosslinker in a one-pot method. These particles are suspended in an aqueous medium to constitute dense suspensions. The viscoelasticity and yield stresses of these samples are studied using oscillatory rheology experiments. Interestingly, as the sample temperature is raised beyond the LCST, the rigidity modulus decreases to a minimum value at the LCST and then increases monotonically with increasing temperature. Such non-monotonic temperature-dependence of the rigidity modulus is observed in all the PNIPAM suspensions, with the suspensions of the stiffer particles showing larger changes in their moduli. These observations are explained in terms of hydrobhobicity-induced particle cluster formation at temperatures above the LCST. Our study reveals that the phase behavior and rheology of dense PNIPAM suspensions can be effectively tailored by controlling the degree of crosslinking of the particles. We believe that the results reported here have the potential to trigger further research on the use of thermoresponsive PNIPAM suspensions as multifunctional materials [13].

5.2 Sample preparation

Aqueous PNIPAM suspensions are prepared by adding dried PNIPAM powder in Milli-Q water. The suspensions are stirred overnight and sonicated for 30 min before being used in experiments. For the dynamic light scattering experiments, very dilute aqueous suspensions are prepared by diluting the dense PNIPAM suspensions with Milli-Q water. For the rheological measurements, dense PNIPAM suspensions are used.

5.2.1 Estimation of the effective volume fraction ϕ_{eff}

The procedure for estimating the effective volume fraction ϕ_{eff} of PNIPAM suspensions used in this work is described in section 3.3 of chapter 3. For soft and deformable

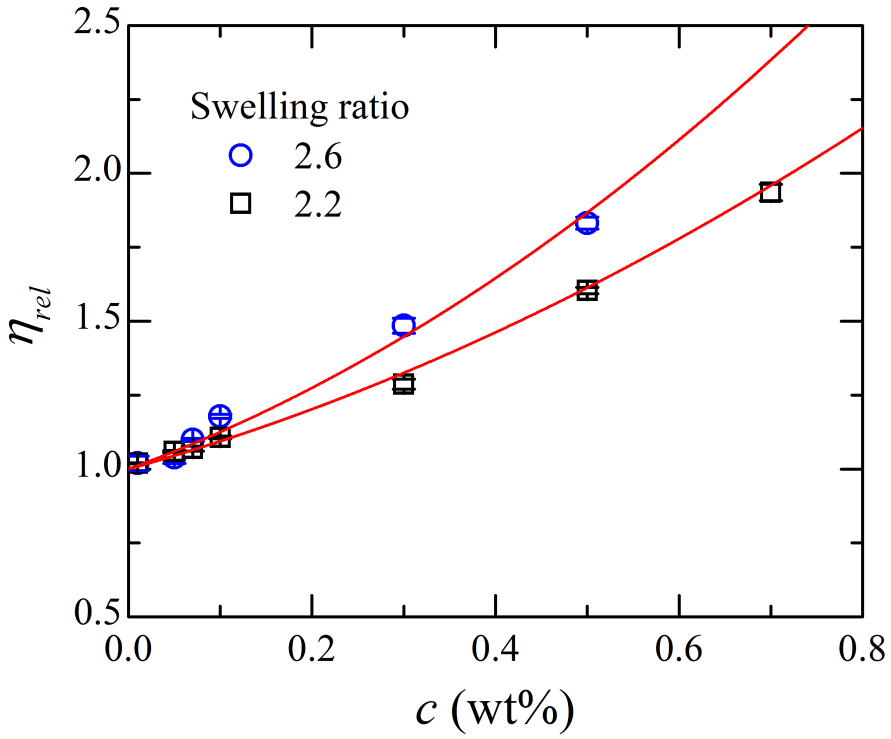

Figure 5.1: Relative viscosity η_{rel} *vs.* concentration c in wt% for suspensions of PNIPAM particles of different swelling ratios. The solid lines are fits to the Batchelor's equation $\eta_{rel} = 1 + 2.5(c/c_p) + 5.9(c/c_p)^2$.

PNIPAM particles in suspension, ϕ_{eff} can be related to their concentration c by the relation $\phi_{eff} = c/c_p$, where c_p is the polymer mass concentration of the particle. The zero shear viscosity η_0 of dilute PNIPAM suspensions at several different concentrations are calculated by fitting the viscosity, η, versus shear rate $\dot{\gamma}$ curves to the Cross model [22]. The relative viscosity η_{rel} of PNIPAM suspensions is defined as the ratio of the zero shear viscosity of the suspension, η_0 and the viscosity of water η_s; $\eta_{rel} = \frac{\eta_0}{\eta_s}$. η_{rel} is plotted in figure 5.1 as a function of the concentration c of aqueous suspensions of PNIPAM particles of different swelling ratios. The effective volume fraction ϕ_{eff} of the suspension at a particular concentration c is estimated by extracting the parameter c_p from a fit to the Batchelor's equation $\eta_{rel} = 1 + 2.5(c/c_p) + 5.9(c/c_p)^2$ [23]. The values of c_p, calculated by fitting the Batchelor's equation to the η_{rel} *vs.* c data and the

Swelling ratio	c (wt%)	c_p (wt%)	ϕ_{eff}
2.2	12	2.87 ± 0.01	4.18
2.6	10	2.21 ± 0.03	4.52

Table 5.1: The particle swelling ratio (the measure of the particle stiffness), the concentration of the particles, c, the fitted value of the polymer concentration, c_p, inside each particle in the swollen state (obtained from the fit of the data in figure 5.1 to the Batchelor equation), and the effective volume fraction ϕ_{eff} of the particles in suspension estimated from the analysis.

estimated ϕ_{eff} values for suspensions of PNIPAM particles of two different stiffnesses, are listed in table 5.1.

5.3 Results and discussion

The dependence of the phase behavior and rheology of PNIPAM suspensions on the stiffness of the constituent particles is studied systematically. The average sizes and the thermoresponsive behavior of PNIPAM particles in dilute suspensions are quantified using dynamic light scattering (DLS) experiments. DLS experiments are performed using a Brookhaven Instruments Corporation (BIC) BI- 200SM spectrometer. The details of the setup are described in chapter 2 (section 2.3.1). For each DLS experiment, a glass cuvette, filled with 5.0 ml. of the dilute PNIPAM suspension (0.01 wt%), is placed in the sample holder of the DLS setup attached to the temperature controller. For a suspension of polydisperse particles, the decays of the normalized autocorrelation functions $C(t) = \frac{g^{(2)}(t)-1}{A}$ are fitted to stretched exponential functions of the form $C(t) = \left[\exp(-t/\tau)^{\beta}\right]^2$. Here, $g^{(2)}(t)$ and A are respectively, the intensity autocorrelation function and the coherence factor of the scattered light. The stretching exponent β, a fitting parameter, is used to calculate the mean relaxation time of the particles in suspension using the relation $<\tau>=(\frac{\tau}{\beta})\Gamma(1/\beta)$, where Γ is the Euler Gamma function. The mean hydrodynamic diameter $<d_h>$ of the particles can be estimated using the Stokes-Einstein relation $<d_h>= \frac{k_B T<\tau>q^2}{3\pi\eta}$, where k_B, T and η are the Boltzmann constant, the absolute temperature and the viscosity of the solvent, respectively [11, 24, 25]. The

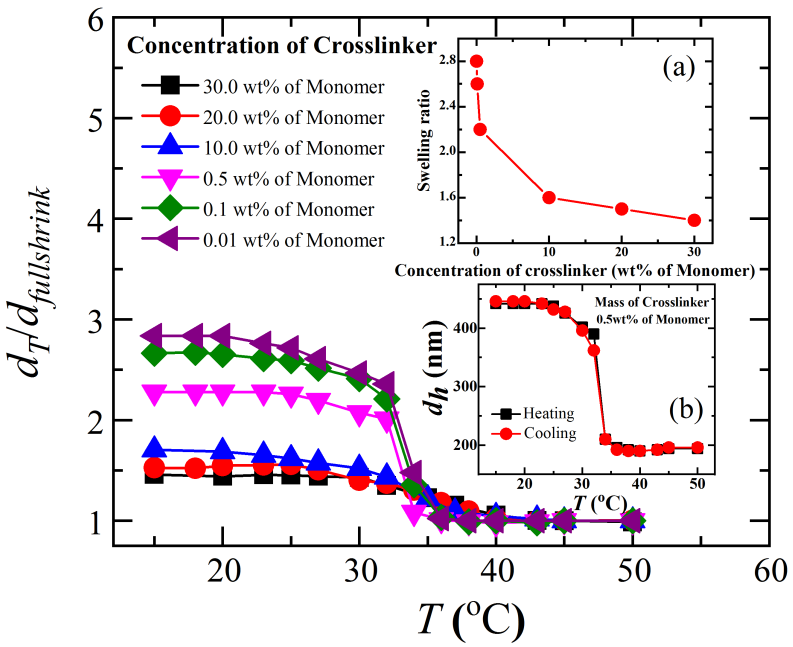

Figure 5.2: Temperature dependent swelling ratios $d_T/d_{fullshrink}$ as a function of temperature T for suspensions of PNIPAM particles synthesized by varying the concentration of the crosslinker. The inset figure (a) shows the dependence of the swelling ratio of the particle on the concentration of the crosslinker. The inset figure (b) shows the temperature dependent hydrodynamic diameter ($< d_h >$) of PNIPAM particles (swelling ratio = 2.2) in aqueous suspension while heating and cooling.

average hydrodynamic sizes $<d_h>$ of the thermoresponsive PNIPAM particles are measured between 15°C and 50°C at temperature intervals of 3°C.

The stiffness of the PNIPAM particles, controlled here by controlling the concentration of the crosslinker, can be quantified by measuring the particle swelling ratio, $d_{fullswell}/d_{fullshrink}$, where $d_{fullswell}$ and $d_{fullshrink}$ are, respectively, the particle diameters in aqueous suspension in the fully swollen and the fully shrunken states [6]. The temperature dependent swelling ratio of PNIPAM particles in an aqueous medium, $d_T/d_{fullshrink}$, where d_T is the particle diameter estimated at a temperature T, is plotted in figure 5.2. It is seen that PNIPAM particles swell maximally at temperatures below 20°C, while they shrink or collapse fully at temperatures above 40°C. The particle swelling ratio, defined here as the ratio of the particle diameters measured at the lowest

and highest temperatures ($d_{fullswell}$ and $d_{fullshrink}$ respectively) accessed in these experiments, is seen to increase with decrease in the concentration of the crosslinker (inset (a) of figure 5.2). Due to their higher osmotic pressures, the polymer networks in soft particles undergo rapid expansion upon the incorporation of water [19, 26–28]. We see from figure 5.2 that the volume phase transition of PNIPAM particles becomes more continuous with increasing particle stiffness. Measurements of the hydrodynamic radii of these particles, performed during both heating and cooling temperature cycles, are seen to overlap very well (inset (b) of figure 5.2). This shows the thermoreversible nature of PNIPAM particles in aqueous medium.

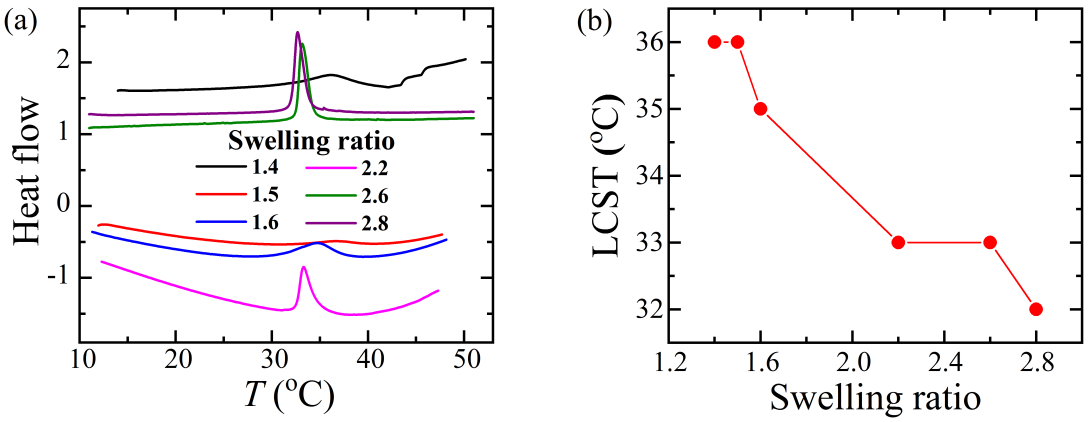

FIGURE 5.3: Heat flow as a function of temperature T for aqueous suspensions of PNIPAM particles of different swelling ratios using differential scanning calorimetry (DSC). (b) Lowest critical solution temperature (LCST) values, obtained from the endothermic peak of the heat flow *vs.* T data for suspensions of PNIPAM particles, are plotted as a function of particle swelling ratio.

The lowest critical solution temperature (LCST) of the particles of different swelling ratios are estimated by performing differential scanning calorimetry (DSC) experiments. The temperature corresponding to the endothermic peak in the heat flow *vs.* temperature (T) data (figure 5.3(a)) gives us a measure of the LCST of these particles in their aqueous suspension and is plotted as a function of swelling ratio in figure 5.3(b). A slight increase (approximately 10%) in the LCST of these particles is observed with

decrease in swelling ratio / increase in particle stiffness. This can be explained by considering that the stiffer particles are more hydrophilic due to the presence of a larger concentration of the crosslinker (N, N'-methylenebisacrylamide) comprising the polar groups N-H and C=O [29, 30].

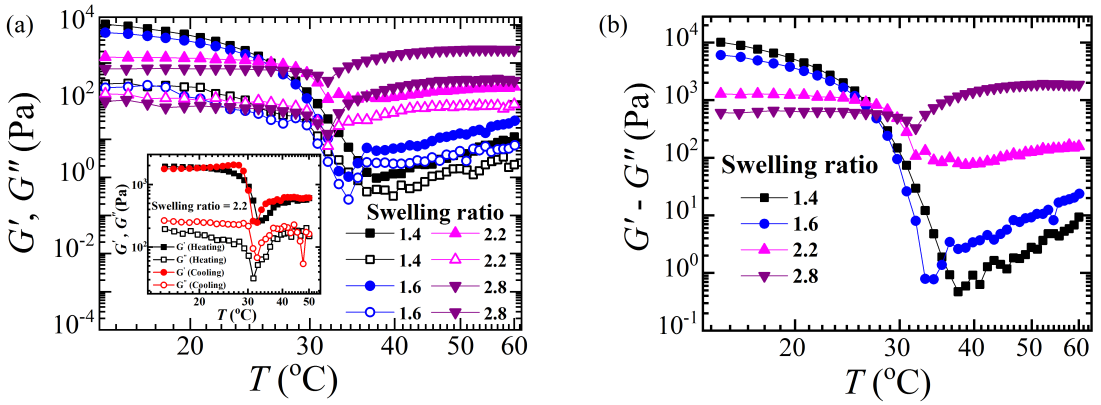

Figure 5.4: (a) The temperature dependent elastic modulus G' (solid symbols) and viscous modulus G'' (open symbols) for suspensions of PNIPAM particles of different swelling ratios. The inset shows the temperature dependent storage modulus G' (solid symbols) and loss modulus G'' (open symbols) while heating and cooling a suspension of PNIPAM particles of swelling ratio = 2.2. (b) Difference between the elastic modulus and the viscous modulus, G'-G'', *vs.* temperature T for suspensions of PNIPAM particles of different swelling ratios.

The rheological results reported here are acquired using a cone and plate geometry (CP-25) of cone radius r_c = 12.49 mm, cone angle α = 0.979° and measuring gap d = 0.048 mm. The temperature dependent mechanical behavior of dense aqueous suspensions of PNIPAM colloidal particles is studied by measuring the linear viscoelastic moduli $G^{'}$ and G'' at a fixed oscillatory strain of amplitude γ = 0.1% and angular frequency ω = 1 rad/s. The temperature is varied in the range 15 – 60°C at a rate of 1°C per minute. The elastic modulus G' and the viscous modulus G'', plotted as a function of temperature T for suspensions of PNIPAM particles of different swelling ratios in figure 5.4(a), are denoted by solid and hollow symbols respectively. Temperature-dependent viscoelastic moduli of these suspensions, measured during both heating and cooling temperature cycles (inset of figure 5.4(a)), are seen to follow approximately

similar paths. The values of $G' - G''$, a measure of the viscoelastic solid behavior of the samples, are plotted in figure 5.4(b) for the same samples. It is seen that $G' > G''$ at $T <$ LCST, indicating that all the PNIPAM suspensions show viscoelastic solid-like behavior at these temperatures. Our results are consistent with those reported in [31]. It is also seen that for a given effective volume fraction below the LCST ($T < 25°$C), the elastic modulus G' of the suspensions increases with decrease in swelling ratio. Moreover, G' increases with increase in swelling ratio at temperatures above the LCST. For the suspensions constituted by stiff particles, the sharp decrease in $G' - G''$ with increase in T upto the LCST is attributed to the rapid deswelling of the particles. At $T \simeq$ LCST, these suspensions are less solid-like, with $G' \approx G''$. The $G' - G''$ values for concentrated packings of soft particles, in contrast, are comparatively more insensitive to temperature. The Poisson ratio of soft microgels are relatively low and the particles are easily compressible at low osmotic pressures [32]. In concentrated packings of soft particles, therefore, shrinkage dominates over particle deformation, thereby allowing the particles to share more contacts with neighbouring particles as they deswell. Increase in thermal energy therefore has a relatively weaker effect on the volume fraction, and hence the viscoelastic moduli, of soft particle suspensions. Finally, as the temperature is raised beyond the LCST, an increase in the viscoelastic moduli is observed, with $G' > G''$ for all the samples. The results summarized in figure 5.4(a) and 5.4(b) are consistent with the those reported by Romeo *et al.* for suspensions of temperature and pH-responsive p-NIPA particles copolymerized with acrylic acid [1]. The steep increase in the viscoelastic moduli, reported by Romeo *et al.* at $T >$ LCST, was explained by considering temperature-dependent changes in the Flory parameter that result in the enhanced formation of rigid particle assemblies at these temperatures.

Frequency sweep oscillatory rheological measurements are next performed to study the dynamics of PNIPAM suspensions at various temperatures and particle stiffnesses. These tests are conducted at temperatures below and above the LCST by varying the angular frequency of the sinusoidal strain oscillation between 10^{-2} rad/s and 10^{2} rad/s,

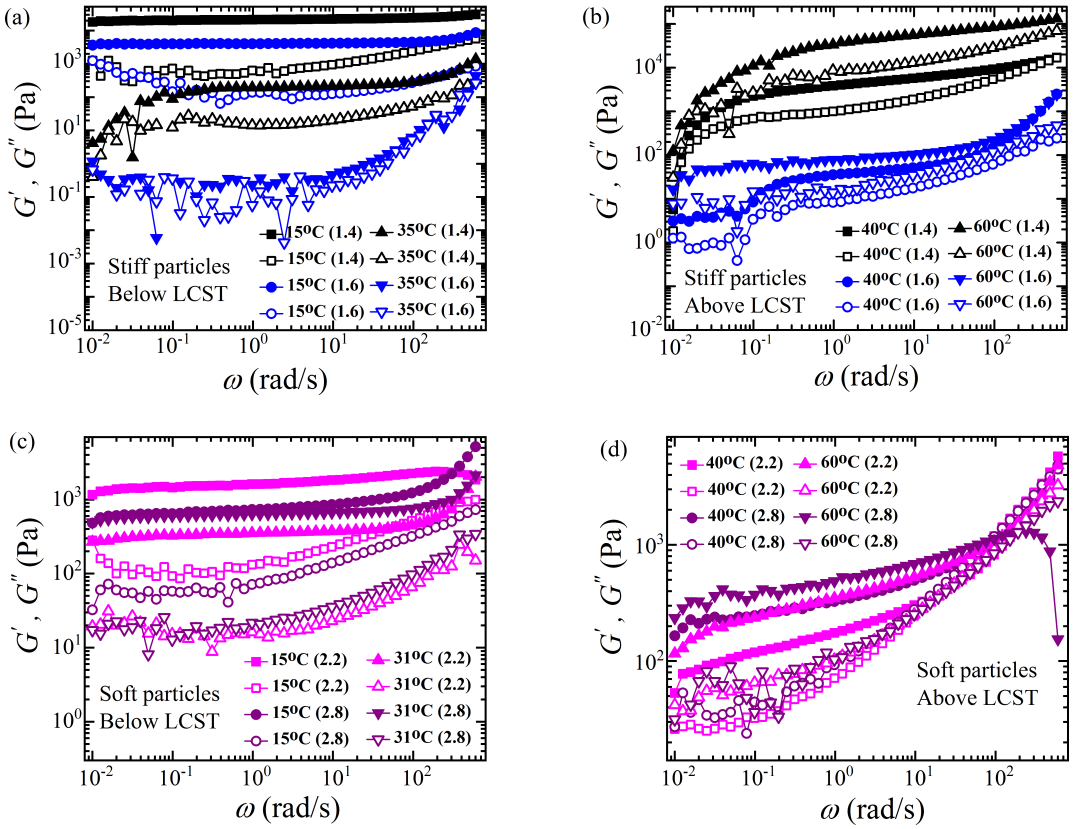

Figure 5.5: Storage modulus G' (solid symbols) and loss modulus G'' (open symbols) *vs.* angular frequency (ω) of suspensions of stiff PNIPAM particles having swelling ratios 1.4, 1.6 at several different temperatures (a) below the LCST and (b) above the LCST. G' and G'' *vs.* ω for suspensions of soft PNIPAM particles having swelling ratio 2.2 and 2.8 at several different temperatures (c) below the LCST and (d) above the LCST.

while keeping the strain fixed at $\gamma = 0.1\%$. At temperatures much lower than the LCST, suspensions of PNIPAM particles display high rigidity values, frequency-independent G' and weakly frequency-dependent G'' (figure 5.5), suggesting the existence of ultra-slow dynamics in these samples [33]. The plateau of G' in this temperature regime is observed to be higher for a suspension of stiff particles when compared to a suspension of soft particles. This is due to the higher particle concentrations in suspensions of stiff particles (Table 5.1). At lower frequencies, the increase of G'' with decreasing angular frequency ω is indicative of the presence of a structural relaxation (crossover of G' and G'') at even lower frequencies. Suspensions at temperatures much below the LCST are solid-like and are expected to have very slow dynamics, which precludes

the measurements of their long relaxation times within the experimental window. G' and G'' of suspensions of stiff particles show strong frequency dependence with $G' \approx G''$ at temperatures close to LCST (figure 5.5(a)). A qualitative change in the frequency dependence of the moduli of these suspensions is noted when the temperature is increased above the LCST (figure 5.5(b)). At these temperatures, the suspensions constituted by softer particles exhibit enhanced frequency dependence of G' and G'' when compared to suspensions of stiff particles (figure 5.5(d)). In this temperature regime, the presence of crossover between G' and G'' for suspensions of soft particles, with $G'' > G'$ indicates the liquid-like dynamics in these suspensions at higher frequencies (figure 5.5(d)).

The nonlinear rheology of dense PNIPAM suspensions at various temperatures and particle stiffnesses is next studied by performing oscillatory strain amplitude sweep tests at an angular frequency $\omega = 1$ rad s^{-1} (figure 5.6). Here the oscillatory strain amplitude γ is varied in the range $0.1 - 4000\%$. The data acquired in amplitude sweep experiments for suspensions of stiff and soft PNIPAM particles at several different temperatures below and above the LCST are plotted in figures 5.6(a) - 5.6(d). As expected for a viscoelastic solid-like material, it is seen that G' and G'' exhibit plateaus at small values of applied strain, with $G' > G''$. With further increase in the applied strain amplitude γ, the elastic modulus G' starts to decrease, while G'' passes through a peak at the point of crossover between G' and G''. Finally at very high strains, the sample exhibits fluid-like behavior which is indicated by $G'' > G'$. The elastic stress σ_{el}, defined as the product of G' and the strain γ, is estimated as a function of γ for all the suspensions and at several different temperatures. Representative data and the analysis are displayed in figure 5.7. The value of strain at which the straight line fit (solid red line) to the σ_{el} vs. γ data deviates by 5% from the prediction of Hookes law (dashed lines in figure 5.7) is the yield strain γ_y while the corresponding stress is the yield stress σ_y (dotted lines in figure 5.7) [34]. It is to be noted that there are two yield points above the LCST (figure 5.7(b)). The second yield strain γ_{y2} and the second yield stress σ_{y2} are computed from the deviation of the second elastic stress (denoted by a

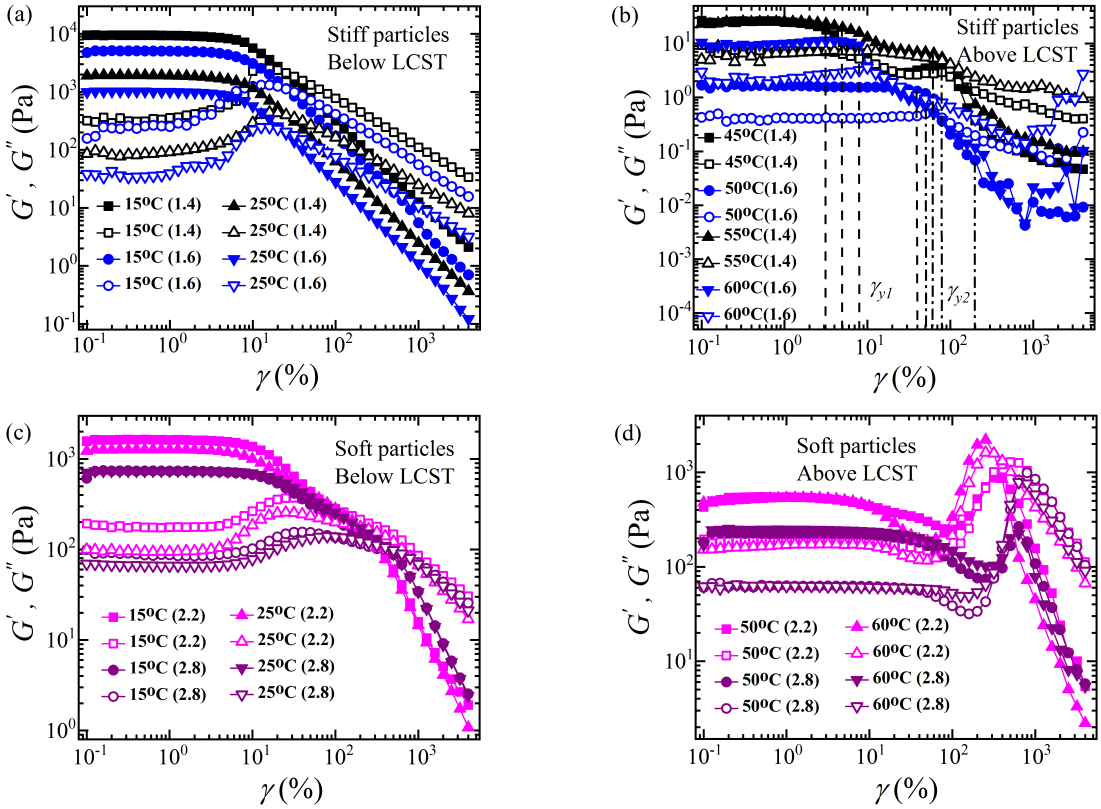

Figure 5.6: Storage modulus G' (solid symbols) and loss modulus G'' (open symbols) *vs.* applied oscillatory strain amplitude (γ) for suspensions of stiff PNIPAM particles having swelling ratios 1.4 and 1.6 at several different temperatures (a) below the LCST and (b) above the LCST. G' and G'' *vs.* oscillatory strain amplitude for suspensions of soft PNIPAM particles having swelling ratios 2.2 and 2.8 at several different temperatures (c) below the LCST and (d) above the LCST.

green line in figure 5.7(b)) from the theoretical Hookean prediction.

The two-step yielding behavior above the LCST (figures 5.6(b) and 5.7(b)) in dense suspensions of stiff PNIPAM particles is reminiscent of the yielding of attractive glasses [35]. We speculate that the suspensions studied here possibly comprise attractive gel-like structures, with the first yield point (γ_{y1}, indicated by dashed lines in figures 5.6(b) and 5.7(b)) arising from the breakup of the clustered network structure of the samples and the second yield point (γ_{y2}) (dashed lines in figures 5.6(b) and 5.7(b)), arising from to the breakup of individual particle clusters or chains [35, 36].

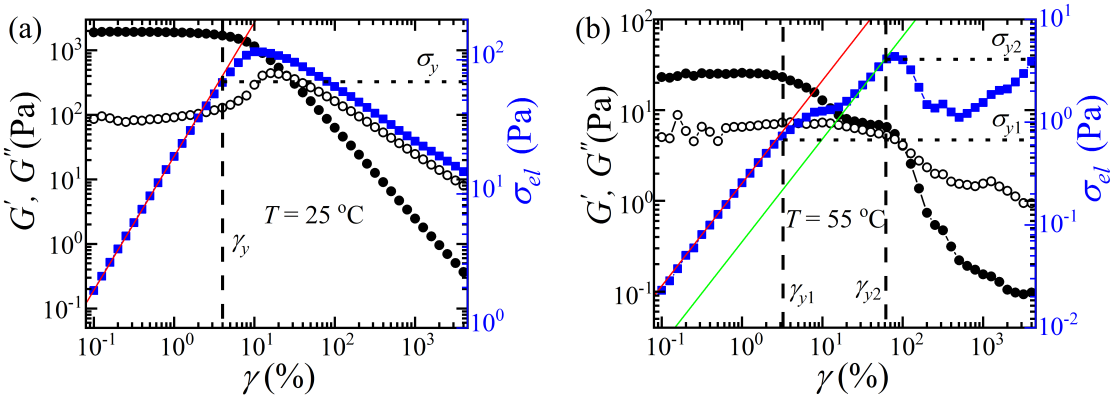

FIGURE 5.7: Variation of storage modulus G' (•), loss modulus G'' (○) and elastic stress σ_{el} (■) with increasing oscillatory strain amplitude (γ) for suspensions of PNIPAM particles of swelling ratio = 1.4 (a) at 25°C (below LCST) and (b) at 55°C (above LCST). The solid line is a linear fit to the σ_{el} *vs.* γ data. The two elastic stresses are denoted by the solid red and green lines respectively. The values of σ_y, σ_{y1} and σ_{y2} are shown by the horizontal dotted lines, while the values of γ_y, γ_{y1} and γ_{y2} are shown by the vertical dashed lines. Interestingly, the data plotted in (b) shows two yield points.

Interestingly, dense suspensions of soft PNIPAM particles show a very different yielding behavior when compared to suspensions of stiff particles. It is seen in figure 5.6(d) that at strains $\gamma \sim 10^3\%$, G' and G'' exhibit strong peaks.

The plateau values of the elastic modulus G', extracted at very low strain aplitudes γ, are designated as G'_{pl} and are plotted *vs.* temperature in figure 5.8(a). The temperature dependence of the estimated yield stress σ_y values for several PNIPAM suspensions are plotted as a function of temperature T in figure 5.8(b). It is seen that G'_{pl} and σ_y both exhibit nonmonotonic trends with varying temperatures. As noted earlier, the elastic behavior of dense suspensions of stiff particles is comparatively more sensitive to changes in temperature, while their temperature dependent swelling ratios are comparatively less sensitive to changes in temperature. Here, DLS experiments are performed in the dilute suspensions, while the rheological experiments are performed in their concentrated regimes. The increased temperature dependent sensitivity observed in suspensions of stiff particles in the rheology experiments arises due to the different swelling mechanisms of these particles in different regimes of volume fractions. From figure 5.8(b), it is observed that the yield stresses σ_y of the suspensions

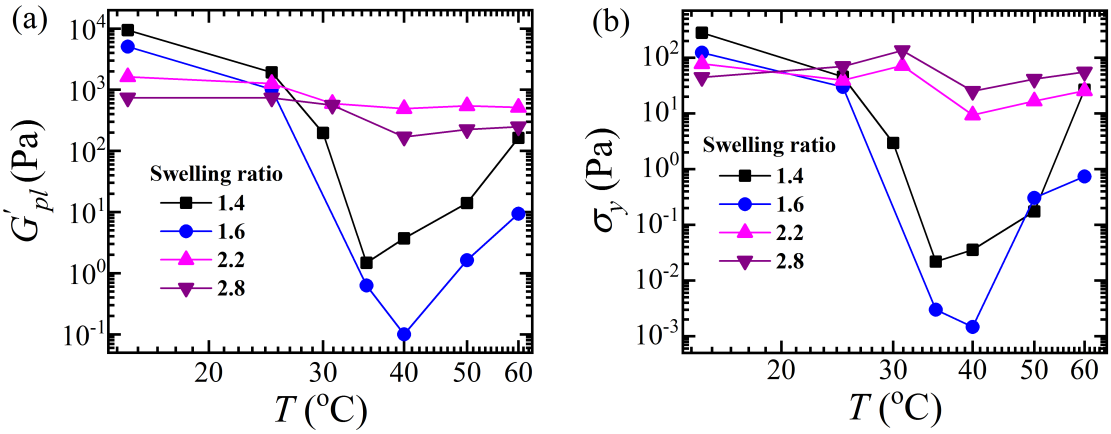

Figure 5.8: (a) Variation of plateau value of elastic modulus G'_{pl} with increasing temperatures for suspensions of PNIPAM particles having different swelling ratios. (b) Variation of yield stress σ_y with the increasing temperatures for suspensions of PNIPAM particles having different swelling ratios.

of stiff particles are the lowest at temperatures near the LCST. Near the LCST, therefore, dense suspensions of stiff PNIPAM particles shear melt at smaller stresses and are mechanically very fragile.

5.4 Conclusions

The present study demonstrates the tunability of the mechanical properties and phase behaviors of PNIPAM suspensions by controlling the suspension temperature and the crossli-nking densities of the particles. PNIPAM particles of different stiffnesses are synthesized by varying the concentration of the crosslinker in a one-pot synthesis method. The swelling ratio of the particles, which characterize the particle stiffness, is estimated from dynamic light scattering experiments. A temperature dependent rheological study of suspensions of PNIPAM particles of different stiffnesses reveals a non-monotonic change in the suspension viscoelasticity when the temperature is increased across the LCST. In these concentrated packings, the aggregation of the PNIPAM particles is determined by the isotropic deswelling and deformability of the particles [37].

Soft particles, characterised by higher osmotic pressures, deswell and deform more than stiff particles in dense suspensions. The stiffer particles, which cannot deswell to the same extent as soft particles, assemble in attractive gel-like network structures in aqueous suspension, with the sample exhibiting two-step yielding under an applied oscillatory shear strain sweep. The viscoelastic moduli characterising suspensions of stiff particles change sharply across the LCST. In contrast, the viscoelastic moduli of suspensions of soft particles change smoothly across the LCST. We believe that changes in the temperature-dependent hydrophobicity of the PNIPAM particles of varying stiffnesses give rise to the observations reported in this chapter.

Since the mechanical behaviors and microstructures of dense PNIPAM suspensions can be controlled by tuning the suspension temperature and the stiffnesses of the constituent particles, their aqueous suspensions are potentially good candidates in the synthesis of multifunctional materials whose mechanical robustness can be controlled by tuning the temperature and particle stiffness. The tunable LCST of PNIPAM particles, obtained by varying the concentration of the crosslinkers, can be exploited in designing soft robotic applications, for example in making microgrippers, or in the folding of flat gel sheets by changing the temperature [38]. Our ability to control the stiffness of PNIPAM particles raises the possibility of their use in soft biomimetic machines. The bending or twisting of a flat gel sheet, comprising layers of hydrogel particle aggregates of different stiffnesses, can, in principle, be achieved by the application of a temperature gradient. The idea of differential stiffnesses is relevant even in natural machines, for example, in the movement of the cell wall and in the rapid changes in the conformations of the modified leaves of the mimosa and the venus flytrap [39]. PNIPAM microgel suspensions are extremely resilient to tensile and compressive stresses and are also very flexible. Since these materials can be used in a range of engineering and biomimetic applications, further research on their mechanical properties is of utmost importance.

References

[1] G. Romeo, A. Fernandez-Nieves, H. M. Wyss, D. Acierno and D. A. Weitz, *Adv. Mater.*, 2010, **22**, 3441.

[2] B. Sierra-Martin and A. Fernandez-Nieves, *Soft Matter*, 2012, **8**, 4141.

[3] A. Scottia, U. Gassera, E. S. Hermanc, M. Pelaez-Fernandezb, J. Hand, A. Menzeld, L. A. Lyonf and A. Fernandez-Nieves, *PNAS*, 2016, **113(20)**, 5576.

[4] Z. Zhang, N. Xu, D. T. N. Chen, P. Yunker, A. M. Alsayed, K. B. Aptowicz, P. Habdas, A. J. Liu, S. R. Nagel and A. G. Yodh *Nature*, 2009, **459**, 230.

[5] C. Pellet and M. Cloitre, *Soft Matter*, 2016, **12**, 3710.

[6] B. R. Saunders and B. Vincent, *Adv. Colloid Interface Sci.*, 1999, **80**, 1.

[7] Y. Han, N. Y. Ha, A. M. Alsayed, and A. G. Yodh, *Phys. Rev. E*, 2008, **77**, 041406.

[8] H. Senff and W. Richtering, *J. Chem. Phys.*, 2015, **111(4)**, 1705.

[9] A. M. Alsayed, M. F. Islam, J. Zhang, P. J. Collings and A. G. Yodh, *Science*, 2005, **309**, 1207.

[10] L. A. Lyon and A. Fernandez-Nieves, *Annu. Rev. Phys. Chem.*, 2012, **63**, 25.

[11] S. K. Behera, D. Saha, P. Gadige and R. Bandyopadhyay, *Phys. Rev. Materials*, 2017, **1**, 055603.

[12] L. Dong and A. S. Hoffman, *J. Controlled. Release*, 1991, **15**, 141.

[13] P. Calvert, *Adv. Mater.*, 2009, **21**, 743.

[14] X. Hu, R. Liang, J. Li, Z. Liu and G. Sun, *Materials and Design*, 2019, **163**, 107547.

[15] N. A. Peppas, J. Z. Hilt, A. Khademhosseini and R. Langer, *Adv. Mater.*, 2006, **18**, 1345.

[16] P. J. Yunker, K. Chen, M. D. Gratale, M. A. Lohr, T. Still and A. G. Yodh, *Rep. Prog. Phys.*, 2014, **77**, 056601.

[17] A. S. Iyer and L. A. Lyon, *Angew. Chem. Int. Edn*, 2009, **48**, 4562.

[18] W. McPhee, K. C. Tam and R. Pelton, *J. Colloid and Interface Sci.*, 1993, **156**, 24.

[19] H. Senff and W. Richtering, *Colloid Polym Sci.*, 2000, **278**, 830.

[20] Y. Zhao, Y. Cao, Y. Yang and C. Wu, *Macromolecules*, 2003, **36**, 855.

[21] K. Kratz , T. Hellweg and W. Eimer, *Colloids Surf. A*, 2000, **170**, 137.

[22] M. Cross, *J. Colloid Sci.*, 1965, **20**, 417.

[23] G. K. Batchelor, *J. Fluid Mech.*, 1997, **83**, 97.

[24] B. J. Berne and R. Pecora, *Dynamic light scattering: with applications to chemistry. biology and physics. John Wiley & Sons:* New York, 1975.

[25] A. Einstein, *Annalen der Physik (in German)*, 1905, **322(8)**, 549.

[26] J. Mattsson, H. M. Wyss, A. Fernandez-Nieves, K. Pham, Z. Hu, D. R. Reichman and D. A. Weitz, *Nature*, 2009, **462**, 83.

[27] Y. Hirokawa, T. Tanaka and S. Katayama, *Microbial Adhesion and Aggregation* (Ed. K. C. Marshall), Springer. Berlin, 1984, **55**, 177.

[28] F. J. Aangenendt, J. Mattsson, W. G. Ellenbroek and H. M. Wyss, *arXiv:1607.07897 [cond-mat.soft]*, 2017.

[29] G. Liu, X. Yang and Y. Wang, *Polymer International*, 2007, **56(7)**, 905-913.

[30] A. Chilkoti, M. R. Dreher, D. E. Meyer and D. Raucher, *Advanced Drug Delivery Reviews*, 2002, **54(5)**, 613-630.

[31] A. Ghosh, G. Chaudhary, J. G. Kang, P. V. Braun, R. H. Ewoldt and K. S. Schweizer, *Soft Matter*, 2019, **15**, 1038.

[32] I. B. de Aguiar, T. van de Laar, M. Meireles, A. Bouchoux, J. Sprakel and K. Schroën, *Scientific Reports*, 2017, **7**, 10223.

[33] H.M. Wyss, K. Miyazaki, J. Mattsson, Z. Hu, D. R. Reichman, and D. A. Weitz, *Phys. Rev. Lett.*, 2007, **98**, 238303.

[34] M. Laurati, S. U. Egelhaaf and G. Petekidis, *J. Rheol.*, 2011, **55**, 673.

[35] K. N. Pham, G. Petekidis, D. Vlassopoulos, S. U. Egelhaaf, W. C. K. Poon, and P. N. Pusey, *J. Rheol.*, 2008, **52**, 649.

[36] P. Gadige and R. Bandyopadhyay, *Soft Matter*, 2018, **14**, 6974.

[37] G. M. Conley, P. Aebischer, S. Nöjd, P. Schurtenberger and F. Scheffold, *Sci. Adv.*, 2017, **3**, e1700969.

[38] W. J. Zheng, N. An, J. H. Yang, J. Zhou, and Y. M. Chen, *Appl. Mater. Interfaces*, 2015, **7**, 1758-1764.

[39] L. Ionov, *Adv. Funct. Mater.*, 2013, **23**, 4555-4570.

6

The effect of activity on the kinetically arrested state of passive particles

6.1 Introduction

Active particles are biological or man-made self-propelled Brownian particles that are capable of consuming energy from their environment and converting it into directed motion [1, 2]. They are nanoscopic or microscopic in size with propulsion speeds up to a fraction of a millimeter per second [3]. The motion of passive Brownian particles is driven by equilibrium thermal fluctuations, while the interplay between the self-propelled motion and random fluctuations in active particles drive them far from the equilibrium state [4–7]. The study of the collective behavior of active particles

can uncover novel strategies for designing smart materials and devices [3, 6]. During the last few decades, active particle suspensions have gained much attention as they provide deep insights into the self-organization behaviour of self-propelled particles in suspension and the interaction between passive and active objects in cells and tissues [8, 9]. Recent experiments and numerical simulations have studied the structure and dynamics of passive particles in the presence of active particles [8]. Laboratory synthesized active particles, whose activity can be easily controlled, are increasingly being used to study their dynamics in suspensions.

The presence of a small amount of active particles in a crowded environment of passive particles can strongly influence the properties and dynamics of the passive particles. Simulations of dense suspensions of self-propelled hard sphere particles reveal that increase in activity speeds up the relaxation dynamics and shifts the glass transition to higher packing fractions [10]. This is also confirmed by another numerical study of a dense driven granular fluid which reports a shift of the glass transition towards higher densities with increase in the external driving force [11]. Theoretical studies have reported that the incorporation of activity or self propulsion induces a cage breaking phenomenon in dense bidisperse suspensions of passive particles [12]. In spite of many theoretical and numerical studies, systematic experiments on the effects of activity in jammed environments have not been reported as yet. In order to bridge this gap, we have conducted experiments by adding a very small fraction of chemically active Janus particles in a concentrated aqueous mixture of passive colloidal particles.

In this chapter, chemically active Janus particles are synthesized by coating platinum on one hemisphere of polystyrene (PS) microspheres. A small fraction of these particles are added to a passive binary PS mixture to obtain an active-passive hybrid suspension. The activity of the Janus particle is controlled by varying the strength of the hydrogen peroxide solution in the aqueous medium. The evolution of the dynamics of passive particles with time is observed from the mean square displacement (MSD) plots obtained as a function of time by video tracking the particles using a confocal microscope. A cage breaking phenomenon, followed by the fluidization of densely

packed binary PS particles, is achieved with increase in the activity of the active particles. Further, the caging properties of the active-passive hybrid system are compared with those of a passive binary mixture. Our experimental results demonstrate that the caging properties and jamming transition of dense passive particle suspensions can be controlled by varying the activity of the Janus particles.

6.2 Sample preparation

6.2.1 Preparation of passive binary mixture

For a passive binary aqueous mixture, we use fluorescent spherical polystyrene (PS) particles of two different sizes ($d_L = 3.87$ μm and $d_S = 2.07$ μm) with a size ratio $d_L/d_S = 1.87$ and number ratio $N_L/N_S = 0.76$. The selected size and number ratio effectively suppress the crystallization of the system. Here, d_L, d_S, N_L and N_S are respectively the size and number of large and small particles. These fluorescent PS microspheres, dispersed in aqueous media, are purchased from Bangs Laboratories Inc. The bigger and smaller particles used in this work are labelled with envy green and flash red dyes respectively. Aqueous PS suspensions containing 1 wt% PS particles are used as the stock suspension in this work. In a typical experiment, stock solutions of the larger and smaller particles of volumes 125 μL and 25 μL respectively are mixed together in a vial. The resulting suspension is sonicated for 15 min for homogeneous mixing. This aqueous binary suspension is centrifuged at a speed of 4000 rpm for 20 min using a Spinwin MC-02 microcentrifuge machine. The supernatant water is discarded and the residue is dried in vacuum after the centrifugation. This method ensures the close packing of bi-disperse PS particles [13]. Bi-disperse PS suspensions of several different concentrations are prepared by diluting the suspensions with 1 : 1 v/v of D_2O : water mixture. The D_2O : water mixture is used as a density matching solvent for the PS particles.

6.2.2 Preparation of active-passive hybrid mixture

The flash red colored smaller PS microspheres ($d_S = 2.07\ \mu$m) are converted into Janus particles by coating one hemisphere with platinum. The details of the synthesis procedure for Janus particles is described in section 2.2.2 of chapter 2. For an active-passive hybrid mixture, an aqueous suspension of Janus particles is added to the passive binary aqueous PS suspension and centrifuged to remove the supernatant water. The residue is dried in vacuum to obtain a close packed active-passive hybrid mixture. Suspensions of active-passive hybrid mixtures of several different concentrations are prepared by diluting the above dense mixture with D_2O. These particles self-propel in a hydrogen peroxide solution due to the platinum induced catalytic decomposition of hydrogen peroxide into water and oxygen [14].

6.2.3 Estimation of particle volume fraction

The volume fraction of particles in suspension is estimated using a centrifugation method as described below. The sedimented particles obtained by centrifugation are dried in vacuum. The volume fraction of the particles in fully dried state is assumed to be at the random close packing volume fraction ϕ_{RCP} [15]. These dried particles are then redispersed in fixed volumes of solvent in order to obtain samples at lower volume fractions ($\phi < \phi_{RCP}$). The volume of the dried particles, determined by measuring the mass of dried particles and using the value for the density [1.055 g/cm^3], is used for estimation of particle volume fraction.

6.3 Designing microchannel as a sample cell

A Y-shaped microchannel with a thickness of approximately 100 μm is used as a sample cell for this work. The image of the Y-shaped microchannel is shown in figure 6.1. The Y-shaped microchannel has two inlets, one outlet and a sample well. Out of the

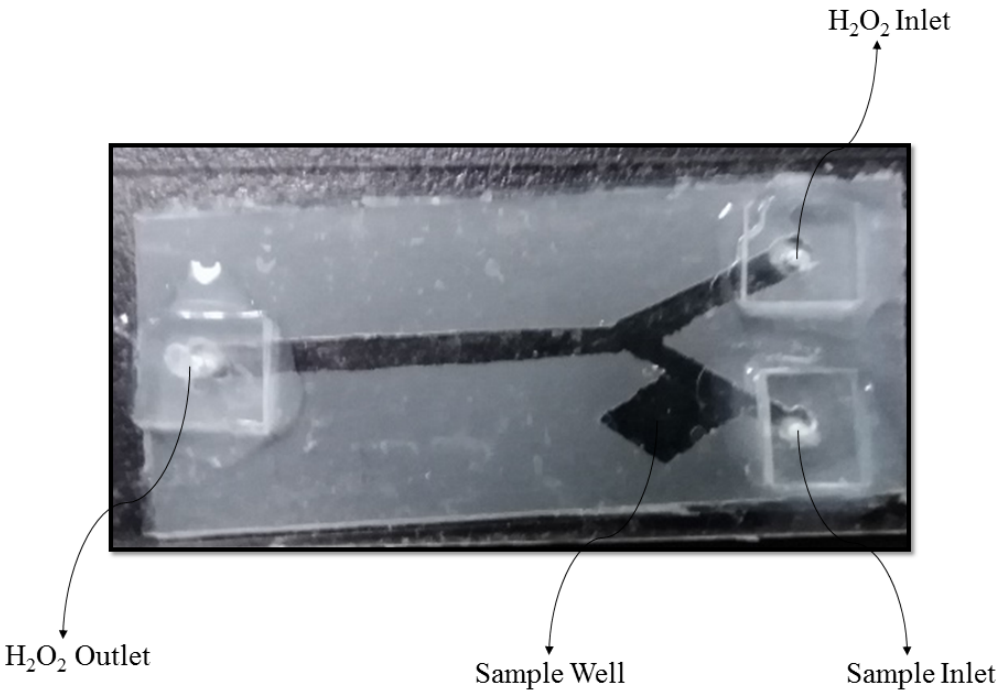

Figure 6.1: Snapshot of Y-shaped microchannel with a sample well, inlets for injecting the sample and the hydrogen peroxide (H_2O_2) solution and an outlet for the exit of H_2O_2 solution.

two inlets, one is for injecting the sample and the other is for injecting hydrogen peroxide (H_2O_2) solution. The outlet allows exit of the H_2O_2 solution. The sample well is filled with the active-passive hybrid mixture during the experiment. Hydrogen peroxide solution, supplied externally at a certain flow rate, slowly diffuses into the well of the channel and reacts with the platinum coated Janus particles. The slow diffusion of H_2O_2 solution into the well prevents the onset of drift motion of the particles. The dynamics of the particles inside the sample well is our subject of interest. Two number 1 thickness coverslips, one microscope slide, three PDMS (polydimethylesiloxane) blocks and a parafilm sheet are required for designing the Y-shaped microchannel. Holes are made on coverslips and microscope slides using sand jets and chemical glass etching, respectively. The positions of the holes on coverslips and microscope slides are synchronized. All the glassware used in these experiments are sonicated in 1.5% v/v Hellmanex III solution at 70°C and then rinsed twice with Milli-Q water. The

glassware is ready to use after it is dried in a hot oven at 60°C for 1 h. A Y-shaped channel with a well attached to the right arm of Y (figure 6.1) is created on a parafilm using a sharp knife. The sample well is created near the inlet in order to avoid the wastage of sample in the channel. This Y-shaped channel is sandwiched between two number 1 coverslips in such a way that the holes of the coverslips are synchronized and placed exactly at the end of each branch of the channel. The parafilm is then heated on a hot plate at 70°C for 2 min. At this temperature, it melts and sticks properly to the coverslips. This method prevents the leakage of solvent in the channel. The holes on the PDMS blocks and coverslips are matched and then attached together using a glue (Ecoflex 005 A & B). For mechanical support of the microchannel, a microscope slide is attached to the coverslip using UV-glue.

6.4 Measurement of hydrogen peroxide decomposition rate

The platinum coated Janus particles self-propel in a hydrogen peroxide (H_2O_2) solution due to the platinum induced catalytic decomposition of hydrogen peroxide into water and oxygen. In an experiment, if all the H_2O_2 molecules available are decomposed by the chemically active Janus particles, then activity can stop after a certain period of time. To maintain constant activity of a chemically active Janus particle for the whole period of the experiment, H_2O_2 solution is supplied externally in a controlled manner. For a certain concentration of active particles, the amount of H_2O_2 solution required to maintain constant activity is estimated by measuring the hydrogen peroxide decomposition rate.

A schematic diagram and snapshot of an experimental setup for measuring the volume of oxygen (O_2) gas evolved during the decomposition of hydrogen peroxide in the presence of platinum coated Janus particles is shown in figure 6.2. The experimental setup consists of an inlet (A in figure 6.2), a container (B) where the reaction between

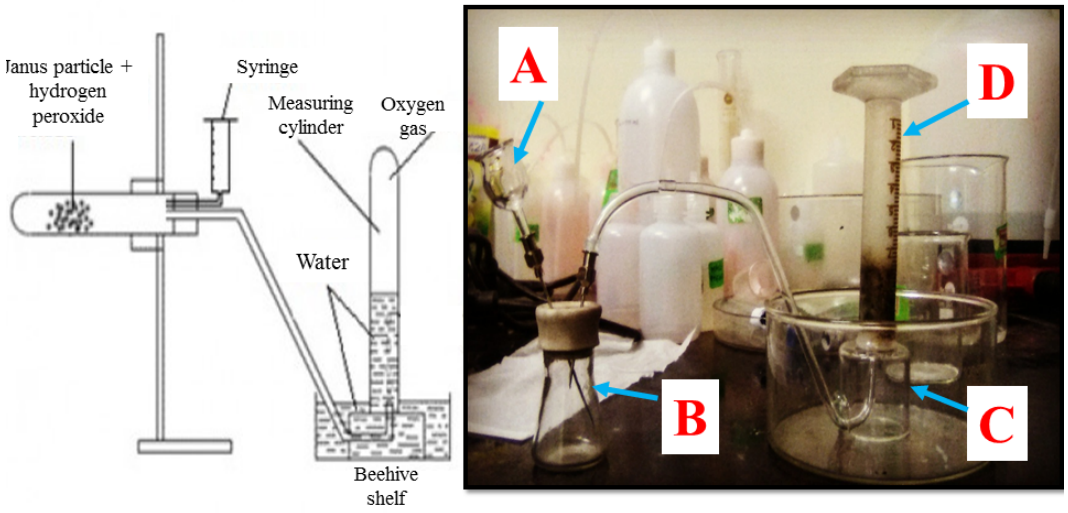

Figure 6.2: (a) A schematic diagram of an experimental setup for measuring the volume of oxygen evolved during the decomposition of hydrogen peroxide (H_2O_2) by platinum coated Janus particles. (b) Snapshot of this experimental setup with an inlet (A) for injecting the Janus particles and H_2O_2 solution, a container (B) where the reaction between Janus particle and H_2O_2 solution occurs, a beehive shelf (C) and a measuring cylinder (D).

the Janus particles and the H_2O_2 solution occurs, a beehive shelf (C) for guiding O_2 gas into a measuring cylinder and a measuring cylinder (D) placed upside down on a beehive shelf for measuring the volume of O_2 gas evolved during the reaction. A certain volume of aqueous Janus suspension is injected into a container followed by the addition of H_2O_2 solution. H_2O_2 decomposes into H_2O and O_2 in the presence of platinum which acts as a catalyst. The O_2 gas that evolved during the reaction inside the container (B) is collected in a measuring cylinder by the downward displacement of water. The volume of O_2 gas measured is equivalent to the volume of water displaced from the measuring cylinder. The volume of O_2 gas evolved during the reaction is recorded as a function of time t. In figure 6.3, the rate of evolution of O_2 gas is

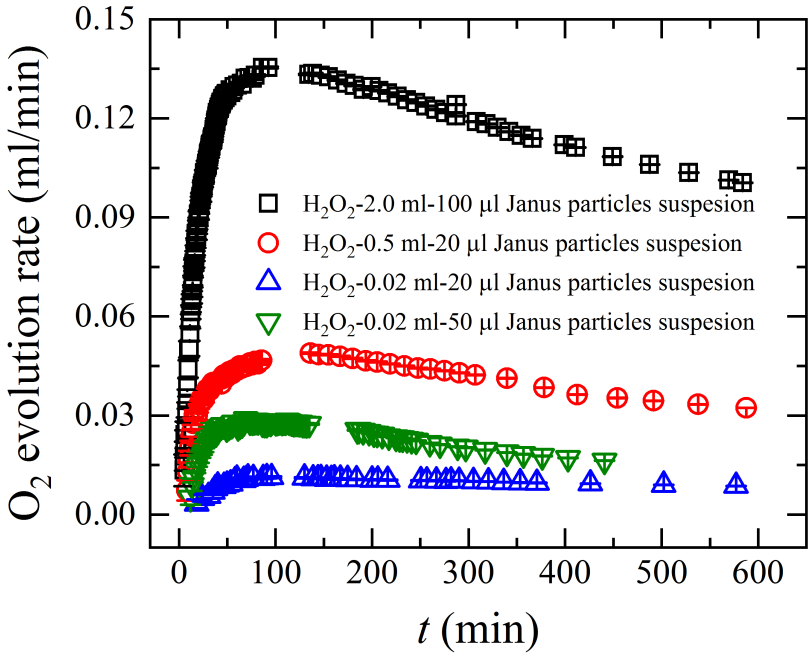

Figure 6.3: Plot of the rate of evolution of O_2 gas as a function of time t for several concentrations of aqueous Janus suspensions and H_2O_2 solutions at 25°C.

plotted as a function of t for several different concentrations of aqueous Janus suspensions and volumes of H_2O_2 solutions. It is observed that the rate of evolution of O_2 gas increases with t in the beginning of the reaction and reaches a maximum value. At later times, the rate of evolution of O_2 gas decreases. This indicates that the decomposition rate of hydrogen peroxide solution or activity of the chemically active Janus particles reduces after a certain period of time. The volume of hydrogen peroxide solution decomposed during this period of time is estimated from the volume of oxygen gas evolved using the stoichiometric calculation described below. From the measured volume of oxygen gas, the number of oxygen molecules produced during the hydrogen peroxide decomposition reaction is estimated using the ideal gas equation (PV = nRT). The balanced equation $2H_2O_2 \rightarrow 2H_2O + O_2$, shows that the total number of hydrogen peroxide molecules decomposed during the reaction is twice the number of oxygen molecules evolved. The volume of H_2O_2 decomposed and the rate of decomposition can be calculated from the above argument and by using the data in figure

6.3. The H_2O_2 decomposition is allowed to proceed till the time when the O_2 evolution rate increases monotonically (figure 6.3). The activity of the chemically active Janus particles is therefore maintained constant by supplying hydrogen peroxide externally with a flow rate equal to the hydrogen peroxide decomposition rate. Care is taken to ensure that the motion of the particles inside the sample well is not affected by the drift generated at this flow rate.

6.5 Confocal microscopy imaging and particle tracking

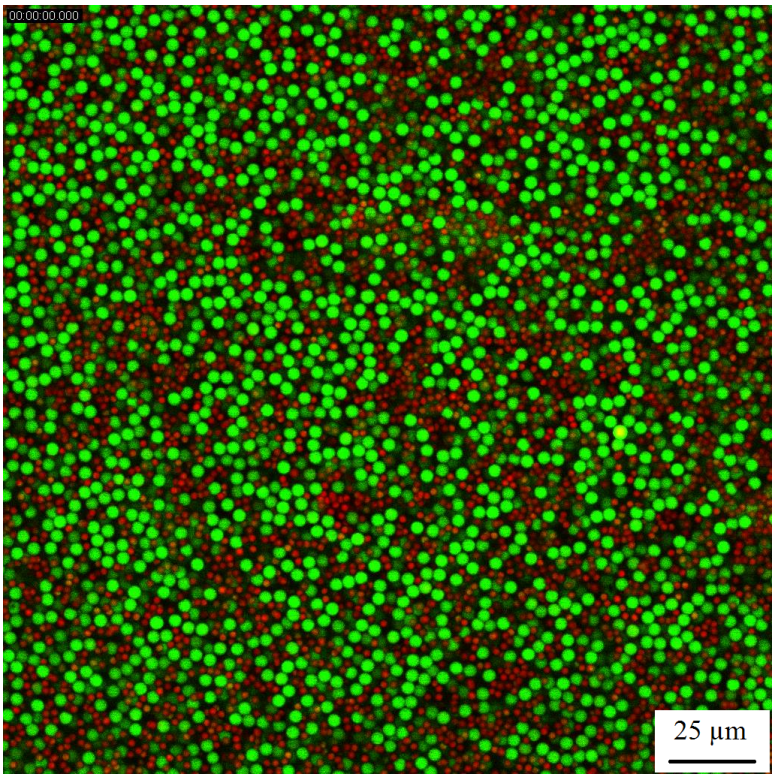

Figure 6.4: A two dimensional confocal microscopy image of an active-passive hybrid mixture at a volume fraction $\phi = 0.57$. All the green particles are passive, while the red particles may be passive or active. The red colored active and passive particles are not distinguishable from each other in this image. The scale bar shown in the image is 25 μm.

Confocal microscopy images are acquired using a Leica TCS SP8 confocal microscope system, with a 40x objective (NA = 0.75) described in section 2.3.5 of chapter 2. Two dimensional confocal images are captured at a rate of 1 frame every 1.47 second over 1200 seconds in a field of view of 91.18 μm x 91.18 μm containing more than 1200 particles. Figure 6.4 shows the representative two dimensional confocal microscopy image of an active-passive hybrid mixture at a volume fraction of 0.57. In all the suspensions studied in this work, only the envy green colored PS particles are tracked using a video spot tracker software developed by Computer Integrated Systems for Microscopy and Manipulation (CISMM). In this software, a green channel is selected for tracking the green PS particles. A disc kernel, with radius of the disc equal to the radius of the particle, is selected for tracking the green particles. The threshold value of the intensity for tracking the particle is automatically decided by the software. The x and y coordinates of the centroid of the particles are linked from one image to the others to form trajectories which are used to compute mean square displacements of the particles.

6.6 Results and Discussion

The mean square displacement $< \Delta r^2(\Delta t) >=< \frac{1}{n} \sum_{i=1}^{n} \Delta r_i^2(\Delta t) >$ of PS particles at a lag time Δt is calculated from the x, y position coordinates of the centroid of these particles, obtained by tracking particle motion for approximately 800 successive frames. Here, $\Delta r_i^2(\Delta t) = \Delta x_i^2(\Delta t) + \Delta y_i^2(\Delta t)$ is the square displacement of a particle during the ith step corresponding to a stepping time Δt. In the above expression, $\Delta x_i(\Delta t)$ and $\Delta y_i(\Delta t)$ are respectively, the x and y displacements of a particle during the i th step, n is the number of steps with a stepping time Δt and <> indicates the average over all particles in the observation volume for a lag time Δt. In figure 6.5, mean square displacement $< \Delta r^2(\Delta t) >$ of passive PS particles is plotted as a function of lag time Δt for several different concentrations of H_2O_2 solution for an active-passive hybrid mixture with a passive particle volume fraction of 0.57. Here, the active particle volume fraction is

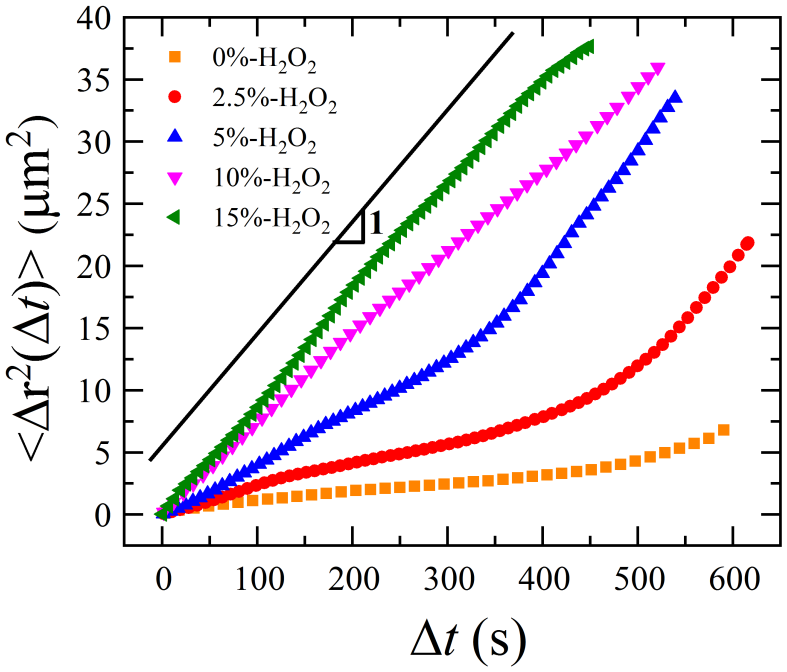

Figure 6.5: Mean square displacement $< \Delta r^2(\Delta t) >$ of passive polystyrene (PS) particles is plotted as a function of lag time Δt for an active-passive hybrid mixture in an aqueous medium for various H_2O_2 concentrations in water. In these experiments, the volume fraction of the passive PS binary mixture and the active Janus particles are, respectively, 0.57 and 0.01. The solid black line with unit slope shows that the dynamics of the particles become increasingly diffusive with increasing strength of H_2O_2 solution.

fixed at 0.01. From this figure, it is seen that the mean square displacement (MSD) curve for the passive binary mixture in the absence of H_2O_2 solution shows a plateau at the initial time. This plateau at the initial time indicates the trapping of particles inside the cages formed by their neighbors [16]. As time progresses, the particles move cooperatively due to the rearrangement of cages which results in the observed increase of MSD values at longer times [17]. The plateaus in the MSD curves slowly disappear with increase in concentration of H_2O_2 solution (2.5% and 5% w/v). As mentioned earlier, an increase in concentration of the H_2O_2 solution increases the active propulsion of the Janus particles in these binary mixtures. For higher concentrations of H_2O_2 solution (10% and 15% w/v), the dynamics become diffusive ($< \Delta r^2(\Delta t) > \propto \Delta t$) even at the lowest Δt values accessible in our experiment. Diffusive behavior of the passive

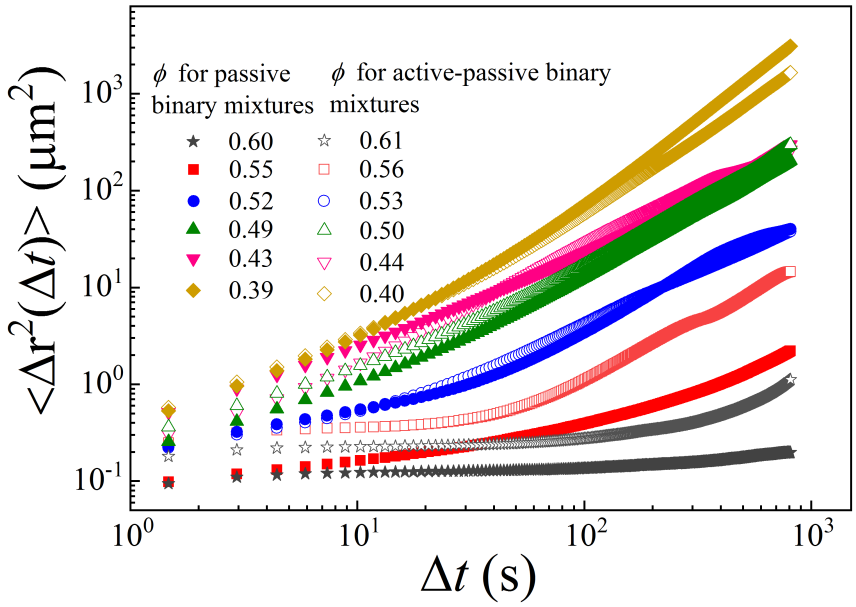

Figure 6.6: Mean square displacement $< \Delta r^2(\Delta t) >$ *vs.* lag time Δt for passive binary particle volume fractions ϕ (solid symbols). On the addition of Janus particles of volume fraction $\phi = 0.01$ to the passive suspensions (data denoted by hollow symbols), the active Janus particles self propel due to the presence of 5% w/v H_2O_2 solution.

particles at these H_2O_2 concentrations is verified by comparing the MSD curves with a solid black line of unit slope (figure 6.5). The activity therefore results in reconfiguring and weakening the cages formed by the passive particles. Our experimental results agree well with previous simulation results [10, 12].

In figure 6.6, the mean square displacement $< \Delta r^2(\Delta t) >$ of passive PS particles is plotted as a function of lag time Δt for passive binary and active-passive hybrid aqueous mixtures at several different volume fractions ϕ in the presence of 5% w/v H_2O_2. The Janus particle volume fraction is kept fixed at 0.01. Figure 6.6 shows that the dynamics of the passive particles, in the absence of any activity is increasingly restricted with increase in volume fraction (solid symbols). This behavior is generally observed in hard sphere colloidal suspensions [16]. It can be seen from this figure that at $\phi = 0.49$, passive particles move a mean square distance 1 μm^2 in ten seconds. However at $\phi = 0.55$, the particle covers a similar mean square distance in 10^3 s. A plateau in the MSD curve is noted with increase in volume fraction, indicating the caging behavior

of the particles. The upturn in the MSD curve at long times is identified with the rearrangement of the cages, which allows the particles to move out of a cage and get trapped in a new cage [18]. It can be inferred by comparing the MSD curves of passive particles at different volume fractions that the time required for rearrangement of cages increases with increase in volume fraction.

When active particles of $\phi = 0.01$ are introduced in a passive binary mixture, the dynamics of passive particles accelerate due to the self-propulsion of the active particles. As a result, the mean square displacement of passive particles increases. This is clearly seen in the MSD plots shown in figure 6.6 (hollow symbols). The plateau value of the MSD curve reflects the size of the cage formed by the particles [17]. The higher plateau value of the MSD curve observed for the active-passive hybrid system indicates that the sizes of the cages formed in this system are larger when compared to the passive binary mixture at the same particle volume fraction. The breaking of particle cages, indicated by the upturn in the MSD data, is seen to occur earlier in the active-passive hybrid mixtures when compared to passive binary mixtures at the same volume fractions.

6.7 Conclusions

In this chapter, we have studied the effects of activity of Janus particles on the jamming dynamics of passive particles in aqueous suspensions. Chemically active Janus particles are synthesized by coating platinum on one hemisphere of polystyrene microspheres. These particles self-propel in a hydrogen peroxide solution due to the platinum induced catalytic decomposition of hydrogen peroxide into water and oxygen. When a small concentration of these active particles is added to passive binary PS suspensions, the cages formed by the passive particles are seen to break due to the activity of the added particles. The jammed passive binary PS suspension fluidizes as the activity or concentration of hydrogen peroxide solution is increased beyond a certain value. The increase in activity increases the average kinetic energy per particle

due to the collisions between the active and passive particles. This reduces the height of the caging potential allowing the particles to escape from their cages [12].

Further studies on caging behavior of passive particles in the presence of active particles can explain specific features of caging and fluidization observed in the cell surface and the nucleus. For example, the bacterial cytoplasm exhibits characteristic glassy features such as caging and the presence of dynamical heterogeneities in the absence of metabolic activity. Interestingly, the system shows liquid-like features when subjected to activity through cellular metabolism [19]. Microrheology studies using a passive micron-sized bead in a live cell nucleus show that the nucleus behaves like an active solid with a finite yield stress at micrometer length scales [20]. Our experimental results are very relevant to activity induced fluidization in biological systems such as cells and tissues.

References

[1] S. J. Ebbens and J. R. Howse, *Soft Matter*, 2010, **6**, 726-738.

[2] S. Ramaswamy, *Annu. Rev. Condens. Matter Phys.*, 2010, **1**, 323-345.

[3] C. Bechinger, R. D. Leonardo, H. Löwen, C. Reichhardt, Gg. Volpe and Gv. Volpe, *Rev. Mod. Phys.*, 2016, **88(4)**, 045006.

[4] D. Babič, C. Schmitt, and C. Bechinger, *Chaos*, 2005, **15**, 026114.

[5] U. Erdmann, W. Ebeling, L. Schimansky-Geier, and F. Schweitzer, *Eur. Phys. J. B*, 2000, **15**, 105-113.

[6] F. Schweitzer, *Brownian agents and active particles:Collective dynamics in the natural and social sciences* (Springer-Verlag, Heidelberg, Germany), 2007.

[7] M. J. B. Hauser and L. Schimansky-Geier, *Eur. Phys. J. Spec. Top.*, 2015, **224**, 1147-1150.

[8] F. K̈ummel, P. Shabestari, C. Lozano, G. Volpe, and C. Bechinger, *Soft Matter*, 2015, **11**, 61876191.

[9] E. Lushi, H. Wioland, and R. E. Goldstein, *Proc. Natl. Acad. Sci. U.S.A.*, 2014, **111**, 97339738.

[10] R. Ni, M. A. C. Stuart and M. Dijkstra, *Nature communications*, 2013, **4**, 2704.

[11] W. T. Kranz, M. Sperl and A. Zippelius, *Phys. Rev. Lett.*, 2010, **104**, 225701.

[12] R. Mandal, P. J. Bhuyan, M. Rao and C. Dasgupta, *Soft Matter*, 2016, **12**, 6268.

[13] P. N. Pusey and W. van Megen, *Phys. Rev. Lett.*, 1987, **59**, 2083 -2086.

[14] J. R. Howse, R. A. L. Jones, A. J. Ryan, T. Gough, R. Vafabakhsh and R. Golestanian, *Phys. Rev. Lett.*, 2007, **99**, 048102.

[15] W. C. K. Poon, E. R. Weeks and C. P. Royall, *Soft Matter*, 2012, **8**, 21.

[16] E. R. Weeks, J. C. Crocker, A. C. Levitt, A. Schofield and D. A. Weitz, *Science*, 2000, **287**, 627.

[17] E. R. Weeks and D. A. Weitz, *Phys. Rev. Lett.*, 2002, **89**, 095704.

[18] T. Narumi, S. V. Franklin, K. W. Desmond, M. Tokuyama and E. R. Weeks, *Soft Matter*, 2011, **7**, 1472.

[19] B. R. Parry, I. V. Surovtsev, M. T. Cabeen, C. S. ÓHern, E. R. Dufresne and C. Jacobs-Wagner, *Cell*, 2014, **156**, 183194.

[20] F. M. Hameed, M. Rao and G. V. Shivashankar, 2012, *PLoS One* **7**, e45843.

7

Future directions

This thesis explores the rheology and dynamics of soft colloidal glasses. We find that particle size polydispersity plays a crucial role in determining the fragilities of soft glassy suspensions. The fragility of these suspensions arises due to the presence of dynamical heterogeneities (DHs). The measurement of DHs in these jammed suspensions of deformable polydisperse PNIPAM particles is therefore essential in order to explain the relationship between fragility and particle polydispersities. In chapter 3, we have qualitatively studied this relationship experimentally.

The experiments reported in chapter 4 study the average microscopic dynamics of jammed PNIPAM particles in suspension. The precise roles of individual particle motion and size polydispersity on cage sizes and lifetimes are interesting questions to address. The cage rearrangement time scale can be obtained from the peak position in the non-Gaussian parameter or four-point susceptibility *vs.* time plots, while the cage sizes can be obtained from mean square displacement (MSD) *vs.* time plots [1]. It is therefore important to estimate these quantities from the position coordinates of the particles obtained by confocal video tracking. Moreover, the number of particles

involved in cooperative rearrangements and the length scales of the cooperative rearrangement regions (CRRs) can be estimated from four-point susceptibility *vs.* time plots. Finally, the relation between length scales of CRRs and particle PDIs can be established.

In chapter 5, we have measured the temperature dependent viscoelastic moduli of dense suspensions constituted by PNIPAM particles of different stiffnesses. In addition to particle stiffness, the interactions between the particles and the volume fractions of the suspensions are also expected to affect the temperature dependent viscoelastic moduli of these suspensions [2]. The addition of kosmotropes (chemicals that cause water molecules to form hydrogen bonds) in aqueous suspensions of PNIPAM particles leads to the strong collapse of particles with increase in temperature [3]. It is also reported in [3] that particles do not significantly deswell when chaotropes (chemicals that disrupt the hydrogen bonding network between water molecules) are added. Moreover, the increase in the concentration of electrolytes in aqueous suspensions of PNIPAM colloids is expected to strongly affect the swelling properties of these particles. These swelling properties of microgels in the presence of kosmotropes, chaotropes and electrolytes can influence the temperature dependent viscoelastic moduli measured in their concentrated suspensions. Therefore, it would be interesting to study the rheology of these dense suspensions while varying the additives in the medium and also the additive concentration. The enhancement of the mechanical properties due to the tunability of the LCST of PNIPAM suspensions can pave the way for realization of soft robots that can sustain loads, grip, and elevate a weight [4]. For instance, a four arm gripper can be designed by crossing two pieces of PNIPAM hydrogel beams in an X-shape. Due to high bending angle of these hydrogels at the LCST, such a gripper could bend to hold an object. Our ability to control the stiffness of PNIPAM particles raises the possibility of their use in soft biomimetic machines. The bending or twisting of a flat sheet, comprising layers of hydrogel aggregates of different stiffnesses, can in principle, be achieved by the application of temperature. The idea of differential stiffnesses is relevant even in natural machines, for example, in the movement of the cell wall and

in the rapid changes in the conformations of the modified leaves of the mimosa and the venus flytrap [5].

In chapter 6, we have studied the effects of active forces or activity on the kinetically arrested state of binary mixtures of passive particles. In addition to the activity, the concentration of active particles can also affect the caging behaviour of passive particles. The increase in concentration of active particles increases the probability of collisions between the active and passive particles. As a result, the average kinetic energy per particle of the system increases which leads to the early breakdown of the cages. At higher active particle concentration, the interaction between active particles is also relevant. In future, it would be interesting to study the dynamics of passive particles by varying the concentration of active particles over a wide range. It has been reported theoretically that activity induces a transition from a fragile to a strong glass [6]. It is essential to verify this theoretical observation by experimentally measuring the relaxation time scales and fragilities of suspensions of passive particles in the presence of active particles using confocal tracking methods.

References

[1] E. R. Weeks and D. A. Weitz, *Phys. Rev. Lett.*, 2002, **89**, 095704.

[2] G. Romeo, A. Fernandez-Nieves, H. M. Wyss, D. Acierno and D. A. Weitz, *Adv. Mater.*, 2010, **22**, 3441.

[3] E. Daly and B. R. Saunders, *Langmuir*, 2000, **16**, 5546-5552.

[4] W. J. Zheng, N. An, J. H. Yang, J. Zhou, and Y. M. Chen, *Appl. Mater. Interfaces*, 2015, **7**, 1758-1764.

[5] L. Ionov, *Adv. Funct. Mater.*, 2013, **23**, 4555-4570.

[6] R. Mandal, P. J. Bhuyan, M. Rao and C. Dasgupta, *Soft Matter*, 2016, **12**, 6268.